Measurement of the leptonic charge asymmetry in $t\bar{t}W^{\pm}$ production using the trilepton final state in proton-proton collisions at $\sqrt{s} = 13$ TeV using the ATLAS experiment

by

Cameron Michael Garvey

Supervisor:
Dr James Keaveney

Co-supervisor:
Dr Sahal Yacoob

A dissertation submitted in fulfillment of the requirements for the degree of Master of Science

in the

UCT-ATLAS Group
Department of Physics
Faculty of Science
University of Cape Town

Declaration of authorship

I, Cameron Garvey, declare that this thesis titled, "Measurement of the leptonic charge asymmetry in the trilepton final state of $t\bar{t}W^{\pm}$ in proton-proton collisions at $\sqrt{s} = 13$ TeV using the ATLAS experiment" and the work presented in it are my own. I confirm that:

- This work was done wholly or mainly while in candidature for a research degree at this University.
- Where any part of this thesis has previously been submitted for a degree or any other qualification at this University or any other institution, this has been clearly stated.
- Where I have consulted the published work of others, this is always clearly attributed.
- Where I have quoted from the work of others, the source is always given. With the exception of such quotations, this thesis is entirely my own work.
- I have acknowledged all main sources of help.
- Where the thesis is based on work done by myself jointly with others, I have made clear exactly what was done by others and what I have contributed myself.

Signed:

Date:

"Education is an admirable thing, but it is well to remember from time to time that nothing that is worth knowing can be taught."

Oscar Wilde

Abstract

In this dissertation, a measurement of the leptonic charge asymmetry (A_C^ℓ) in top quark pair production in association with a W boson ($t\bar{t}W^\pm$) is presented. The A_C^ℓ is sensitive to new physics beyond the standard model, such as the axigluon and as a result, a measurement of the A_C^ℓ could prove useful in searches for new physics. The data set used in this measurement consists of proton-proton collisions at the Large Hadron Collider (LHC) at $\sqrt{s} = 13$ TeV, which was recorded using the ATLAS experiment and corresponds to an integrated luminosity of 139 fb^{-1}. An event selection scheme was put in place to optimally select for $t\bar{t}W^\pm$ events in the trilepton final state while suppressing background events. The A_C^ℓ is calculated using the pseudorapidities of the two leptons that decay from a top quark and a top anti-quark. A lepton-top association was implemented using machine learning which was used to correctly identify the leptons which decay from top quarks in 72% of $t\bar{t}W^\pm$ events. Using the results obtained from the lepton-top association, the A_C^ℓ was measured using a method called the fit across regions (FAR) method. This method makes use of machine learning to differentiate between signal ($t\bar{t}W^\pm$) and all of the backgrounds to increase the sensitivity to the A_C^ℓ. Using the FAR fit, a leptonic charge asymmetry of A_C^ℓ = -9 % $\pm$ 22 % was extracted from Asimov data which is consistent with Standard Model prediction of the A_C^ℓ, as expected. Results of a fit to the ATLAS data remain blinded as this analysis forms the basis of an official ATLAS measurement which is yet to be published. The dominant source of uncertainty results from the limited size of the data set. Further data acquired at the LHC over the next decade should reduce the impact of the dominant uncertainty of the measurement of the A_C^ℓ in $t\bar{t}W^\pm$.

Acknowledgements

Over the last two years I have gained a wealth of experience an knowledge and have built this masters through the help and support of those around me. I would like to express my gratitude to several individuals and groups without whom this masters wouldn't have been possible.

First and foremost I would like to thank my supervisor Dr James Keaveney. Your expertise and guidance have truly helped me grow as a researcher and the lessons I have learnt from this experience will stand me in good stead for any endeavours that the future may hold. I would also like to thank my co-supervisor Dr Sahal Yacoob for his insightful comments and discussion which always showed me to look at the problem from another angle. Thank you to the University of Cape Town for the support financially through the masters research scholarships and the BRAAS award.

I would like to thank my colleagues in the UCT-ATLAS group. To Ryan and Kevin, thank you for your patience and helping me with even the most naive of questions. To Ben, Jake and Senzo, thank you for the discussions and helping to make the masters a well rounded experience. I would also like to thank my collaborators at the Instituto de Física Corpuscular for their help on this project. To Fabio and Maria, thank you for your knowledge and insight on the analysis with a special thanks to Fabio concerning the estimation of fake leptons. To Marcos, thank you for our discussions concerning the analysis and code these proved invaluable.

I would like to thank my parents for their love and support on this journey with special thanks to my mother for proofreading several of my drafts. Lastly, I would like to thank Emily. Your unwavering belief in me and kind words of encouragement keep me going through even the toughest of times.

Contents

List of Figures

List of Tables

Chapter 1

Introduction

High energy particle physics is a branch of physics aimed at studying the laws of nature at a fundamental level. The goal is to provide a complete and validated picture of all of the elementary particles and the forces which govern them. During the 1960s, the framework of the standard model (SM) of particle physics was developed, which provided a deeper understanding of particle physics. Since then, the various particles described in the SM have been measured experimentally [13]. Although this model has provided accurate predictions there are several open questions such as: What is dark matter and dark energy? [14] Why is there an excess of matter over anti-matter in the universe? [15] These open questions leave room for new physics theories, which are collectively known as beyond the SM (BSM) [16]. An important method to test these theories is by accelerating and colliding particles and measuring the decay products which occur as a result.

Particle accelerators are used to accelerate charged stable particles such as protons and electrons to speeds approaching the speed of light [17]. The measurement presented in this dissertation uses data recorded at the Large Hadron Collider (LHC) [18] using the ATLAS experiment. The LHC is the particle accelerator with the highest centre-of-mass energy built to date and can reach centre-of-mass energies of 13 TeV. These high energies provided by the LHC allow researchers to investigate large mass ranges to test predictions provided by the SM as well as new physics models. The process and observable studied here are the $t\bar{t}W^{\pm}$ process and the leptonic charge asymmetry (A_C^{ℓ}) respectively. Previous measurements of the $t\bar{t}W^{\pm}$ cross section have yielded values that are consistently somewhat larger than the SM prediction [7, 9]. The A_C^{ℓ} is an observable which is sensitive to new physics models such as axigluons [19] and provides a complementary handle to test ttW modelling. Measuring the A_C^{ℓ} in $t\bar{t}W^{\pm}$ provides a new approach to constraining and testing both the SM and BSM theories.

The measurement of the A_C^{ℓ} in $t\bar{t}W^{\pm}$ is presented as follows in this dissertation. The theoretical context for this measurement is presented in chapter 2. In chapter 3 the LHC

and the ATLAS experiment are discussed. This is followed by a discussion of the $t\bar{t}W^{\pm}$ process and the charge asymmetry which are presented in chapter 4. The methods used to measure the A_C^{ℓ} are presented in chapter 5, followed by the conclusion in chapter 6.

Chapter 2

Theoretical context

This chapter provides an introduction to the theoretical context for the measurement of the A_C^ℓ in $t\bar{t}W^\pm$. An introduction to the SM is presented in section 2.1. The particles described in the SM specifically fermions and bosons are defined in sections 2.1.1 and 2.1.2 respectively. This is followed by a brief discussion of the open questions in section 2.1.3. A presentation of selected extensions to the SM is presented in section 2.2. Section 2.3 addresses the methods used to produce the simulation.

2.1 The Standard Model of particle physics

The SM provides the theoretical understanding which models the fundamental particles and the forces that govern them [20, 21, 22, 23]. The constituents of the SM are broadly categorised based on their spin. Particles with an integer spin are called bosons and particles with half-integer spin are called fermions. Figure 2.1 shows the particles and force carriers in the SM. The spin, charge, and mass for each of these particles are stated[1]. The particles presented in figure 2.1 will be outlined and discussed in more detail in the following sections.

2.1.1 Fermions

The fundamental fermions are the building blocks that makeup all the matter in the universe. These are particles that have half-integer spin. There are twelve fermions within the SM, each with an anti-matter equivalent. These anti-matter particles are identical to the corresponding matter particle but with the opposite quantum number. For example, the electron (e^-), with a charge of -1, has an anti-matter equivalent in the form of the positron (e^+) which has a charge of +1. Fermions can be further categorised into two major categories namely quarks and leptons. This classification is based on whether particles can interact with the strong force or not. The quarks are particles that can interact with the

[1]Natural units are used where the Planck constant ($\hbar$) and the speed of light (c) are both equal to one

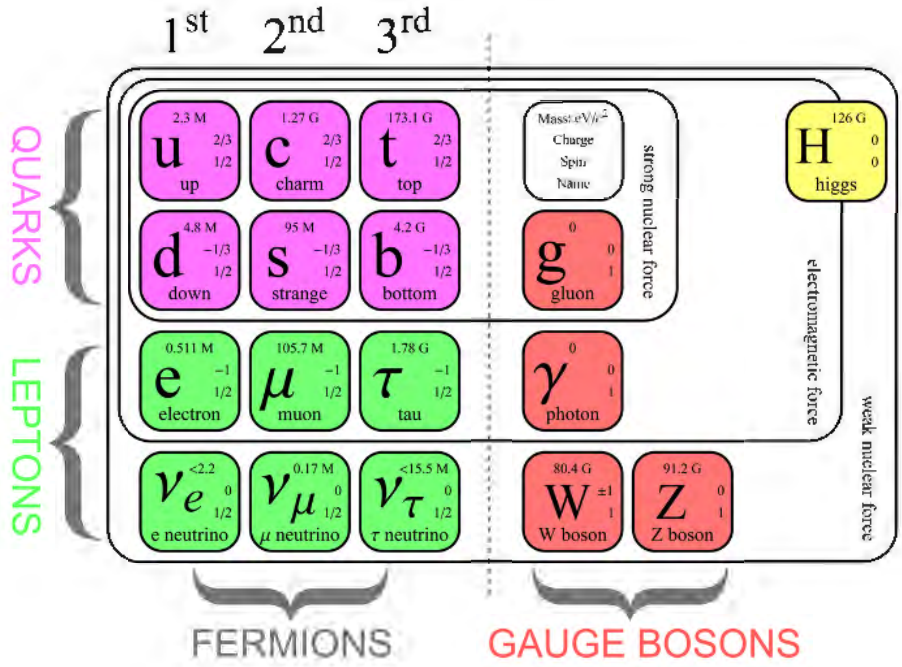

Figure 2.1: A diagram defining the 12 fundamental particles and the 5 force carriers that make up the SM [1]. The green (leptons) and purple (quarks) make up the fermions while the red (vector bosons) and yellow (scalar boson) make up the bosons. The masses stated are as of 2019.

strong force while the leptons cannot.

The quarks are shown in purple in figure 2.1 and are particles with non-integer charges either $+\frac{2}{3}$ or $-\frac{1}{3}$. There are six known quarks namely the up, down, strange, charm, top, and bottom, where the up, charm and top quarks have a charge of $+\frac{2}{3}$ while the down, strange and bottom have a charge of $-\frac{1}{3}$. In terms of quarks, most of the known universe is made up of up and down quarks. These two quarks form the constituents of protons and neutrons. The quarks that are important in this analysis are the top and bottom. The top quark is the most massive particle in the SM with a correspondingly short lifetime of less than 10^{-24} seconds. It is important to note that the top quark decays almost exclusively to a W boson and a bottom quark. The bottom quark, on the other hand, is comparatively long-lived with a lifetime of approximately 10^{-12} seconds. This comparatively long lifetime of the b-quark is utilised in the identification of jets that result from the fragmentation of bottom quarks.

As seen in figure 2.1, the leptons are shown in green. There are also six leptons in the SM namely the electron, muon, and tau each with a corresponding neutrino. Leptons have integer charges of either 0 for neutrinos or -1 for the electron, muon and tau. This analysis will be focussing primarily on two of the leptons - the electron and the muon. The

neutrinos are only measured indirectly in the detector in the form of an observable known as missing transverse momenta ($E_{\mathrm{T}}^{\mathrm{miss}}$), while the tau lepton decays before interacting with the detector. As a result, the only leptons that are directly detected are the electron and muon. These particles will be used to construct the variable of interest in this measurement which is the leptonic charge asymmetry (A_C^{ℓ}).

2.1.2 Bosons

Bosons are the particles that are represented in figure 2.1 in red and yellow. The fundamental bosons are the force carriers in the SM. There are six bosons in the SM which are the photon (γ), Z boson, $W^{\pm}$ boson, the gluon and the Higgs boson. The photon is a massless particle that carries the electromagnetic force. The Z boson and $W^{\pm}$ boson carry the weak force and are massive particles. The gluon carries the strong force and is a massless particle. The bosons which are of particular interest to this analysis are the W^{+} and W^{-} bosons. In the $t\bar{t}W^{\pm}$ process, the $W^{\pm}$ bosons are produced in association with a top-quark pair. The Higgs boson was discovered in 2012 at the LHC using the ATLAS and CMS experiments [24, 25] with a mass of 125.25 $\pm$ 0.17 GeV [26]. The force which hasn't been mentioned is gravity as this is currently not included within the SM.

2.1.3 Problems in the Standard Model

The SM is a theory that has been scrutinised and rigorously tested since it was first proposed. Although this theory provides a good description of the fundamental particles it does not provide a complete picture of nature at the smallest scales. As a result, several open questions need to be answered. A few of the largest problems are discussed below.

Gravity: Gravity is the only fundamental force not included within the SM framework. Extensions to the SM have been theorised such as the inclusion of a particle known as the graviton. However, attempts to extend the SM by including gravity have run into theoretical difficulties at high energy scales.

Neutrino masses: Neutrino masses were discovered through the observation of the neutrino oscillations [27, 28] which opened up several questions concerning the nature of neutrinos. One of the most prominent questions is whether neutrinos are their own anti-particles known as Majorana particles [29].

Dark matter and dark energy: Cosmological observations of the matter and energy compositions of the universe have revealed that matter only makes up 5% of the universe [13]. The rest of the mass and energy is made up of unknown sources. These sources have

been termed dark matter and dark energy which comprise approximately 27% and 67% of the remaining matter and energy respectively.

Matter anti-matter asymmetry: It has been observed that there is an excess of matter as compared to anti-matter in the universe [30]. No mechanism in the SM accurately explains the abundance of matter over anti-matter.

2.2 Beyond the Standard Model

Several theories have been proposed with the intent of answering the questions posed in section 2.1.3 and are collectively known as beyond the standard model (BSM) theories. These theories provide theoretical predictions which can be tested at colliders such as the LHC. Examples of such theories are string theory and supersymmetry. One such particle predicted by BSM theories, which applies to this measurement, is the axigluon and is predicted to be a massive, spin-one gauge boson [19]. A BSM theory that is also relevant to the measurement of A_C^ℓ is that of Effective Field Theory (EFT). The EFT framework extends the SM lagrangian through the inclusion of higher-dimensional operators and provides a model independent method of parameterising deviations from the SM [31]. Within the EFT framework the operators which affect this measurement are the C_{uG} and C_{uW} operators[9]. Recent publications from the LHCb [32] and Muon g-2 [33] experiments at CERN and Fermilab respectively, have provided evidence for BSM physics. Although these publications indicate new physics as of the writing of this dissertation there have been no confirmed discoveries of new physics.

2.3 Simulation of physics processes

The data measured at the LHC will be comprised of several underlying physics processes. These processes include signal and background processes that need to be simulated and calibrated to provide an accurate representation. This simulation uses event generators such as `MADGRAPH` [34], `PYTHIA` [35], `SHERPA` [36], and `POWHEG` [37]. These event generators are used to simulate the hard scattering, parton shower, and hadronization. The definitions for hard scattering, parton shower and hadronisation are as follows. The hard scattering is the energetic interaction between partons (gluons or quarks) at high energy. The theory which models the interactions between partons is quantum chromodynamics (QCD). Due to the high energies involved in the hard scattering, the calculation of these interactions uses a perturbative expansion [38], where all calculations are leading order (LO) unless stated otherwise. The parton shower is a lower energy radiation of particles that arise due to the colour charge. Hadronisation is the formation of quarks into colour neutral particles called hadrons. The parton shower algorithms simulate the branching of each of the partons in

the event into two partons. This approximates higher-order real-emission corrections to the hard scattering [39]. It should be noted that some higher-order real-emission corrections can be included if the hard scattering is calculated at next-to-leading order or higher orders. The quarks and gluons resulting from the hard scattering and parton shower, hadronise into colour-neutral objects. This comes as a result of the colour confinement hypothesis which states that no objects with a non-zero colour charge can propagate as free particles. The combination of the parton shower and hadronization results in jets of hadrons. The parton shower can be simulated using `PYTHIA` or `SHERPA`. The generators `MADGRAPH` and `POWHEG` are not capable of simulating a parton shower and as a result, need to be interfaced with one of the generators able to parton shower. In addition, to ensure that the predictions provided by the simulation yield physical predictions signed weights are provided by certain next-to-leading order (NLO) simulation generators. These weights are applied as per-event weights to yield physical predictions.

Chapter 3

The LHC and the ATLAS detector

This dissertation investigates top quark physics and as a result, requires access to high energy ranges to facilitate the study of top quarks due to their large mass. For this purpose, the LHC provides an ideal environment as it is the particle accelerator with the highest centre-of-mass energy built to date, capable of reaching $\sqrt{s} = 13$ TeV. The LHC was built by the European organisation for nuclear research (CERN) between 1998 and 2008 near the town of Geneva. The LHC has a circumference of 27 km and is located 175m below ground. A schematic of the Large Hadron Collider (LHC) complex is shown in figure 3.1. The process of accelerating protons to high energies is implemented in several stages. The protons are generated by stripping the electrons from hydrogen atoms through the use of electric fields. These protons are then accelerated using the Linac 2 which can reach energies of 50 MeV. The proton beam is then passed to the Proton Synchrotron Booster (PSB) which increases the energy to 1.4 GeV. The next stages of acceleration are done using the Proton Synchrotron (PS) and the Super Proton Synchrotron (SPS) which accelerate the proton beams to 25 GeV and 450 GeV respectively. Finally, the two proton beams are transferred to beam pipes of the LHC, where one beam will circulate clockwise while the other counter-clockwise. To keep the proton beams concentrated and circulating in the LHC ring superconducting dipole magnets were used. These magnets are cooled to 1.9K to produce the 8.33 T magnetic fields. The proton beams will each be accelerated to 6.5 TeV respectively before interacting and resulting in the final centre-of-mass energy of 13 TeV.

Once the beams have been accelerated, the next step is the interaction of the two beams. Quadrupole magnets are used to bend and focus the beams to cross at 4 points around the LHC ring as shown in figure 3.2. Each of these points is known as an interaction point and lies at the centre of one of the four main detectors which are the ALICE [40], ATLAS [41], CMS[42], and LHCb [43] detectors. At these interaction points, bunches of approximately 1.2×10^{11} protons cross every 25 ns resulting in a frequency of 40 MHz. In these bunch crossings, a hard scattering can occur from which processes of interest are produced such as the Higgs boson or top quarks. The decay products of these collisions are then ejected away

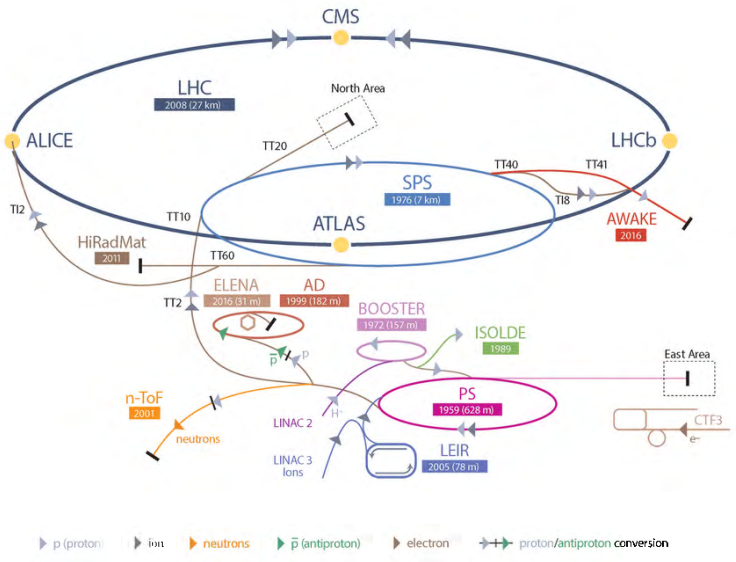

Figure 3.1: A schematic of the LHC accelerator complex is shown. The accelerators and beam lines are shown as well as the major detectors. [2]

from the interaction point in all directions. The purpose of the detectors is to accurately measure the energy and direction of these decay products so information can be inferred about the processes which created them. This dissertation makes use of data recorded using the ATLAS detector and information about the detector will be provided in section 3.2.

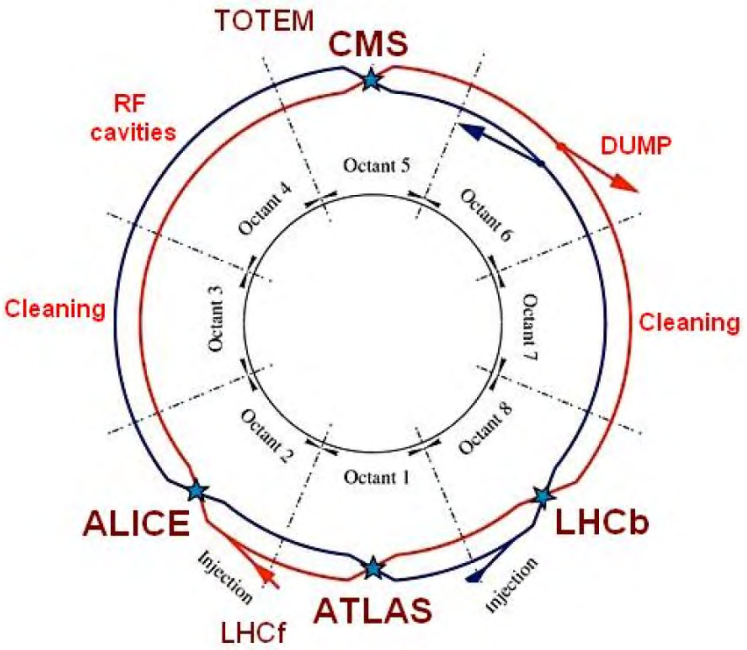

Figure 3.2: A diagram of the interaction points and their corresponding detector around the LHC ring are shown [3]

.

3.1 Luminosity

An important measure of merit for colliders is their luminosity. The instantaneous luminosity estimates the number of proton-proton collisions per unit area per unit time and has units of $cm^{-2} \cdot s^{-1}$. The equation for the instantaneous luminosity at the LHC is given by equation 3.1.

$$\mathcal{L} = \frac{k_b N_b^2 f_{rev} \gamma}{4\pi \epsilon_n \beta^*} \tag{3.1}$$

In equation 3.1 k_b is the number of bunches per beam, N_b is the number of protons per bunch, f_{rev} is the revolution frequency, ϵ_n is the normalised transverse beam emittance and β^* is related to the transverse size of the particle beam at the interaction point.[44] The maximum instantaneous luminosity at the LHC during run 2 was 10^{34} cm^{-2} s^{-1}. The instantaneous luminosity is used to calculate the integrated luminosity which is the integral of the instantaneous luminosity over time which is shown in equation 3.2.

$$L = \int \mathcal{L} dt \tag{3.2}$$

The data used in this measurement at the LHC must satisfy several criteria which relate to the LHC beams, and the status of the ATLAS sub-detectors. Satisfaction of these criteria ensures that the data is of sufficient quality to enable the measurement of physical observables at high precision. Events that satisfied these criteria were recorded during good runs of the LHC. The LHC run times are broken down into two-minute intervals which are known as luminosity blocks (LB). These good runs are stored in a list called the good runs list (GRL) which is made up of LB's which satisfied all of the above-mentioned criteria. Figure 3.3 shows the total integrated luminosity over the data taking period of 2015 to 2018. In figure 3.3 the cumulative luminosity delivered to the ATLAS detector is shown in green while the cumulative luminosity recorded by the ATLAS detector is shown in yellow. The portion of the cumulative luminosity which is good for physics as recorded by the ATLAS detector is shown in blue and results in a total integrated luminosity of 139 fb^{-1}.

3.2 The ATLAS detector

The ATLAS detector is the largest detector by volume ever built. The detector is 46m long, 25m in diameter with a weight of 7000 tonnes. There are two general-purpose detectors at the LHC one of which is the ATLAS detector. Figure 3.4 shows a labelled diagram of the interior of the ATLAS detector. In figure 3.4 it can be seen that the detector is comprised of several smaller sub-detectors. Each sub-detector is split up into two main regions the

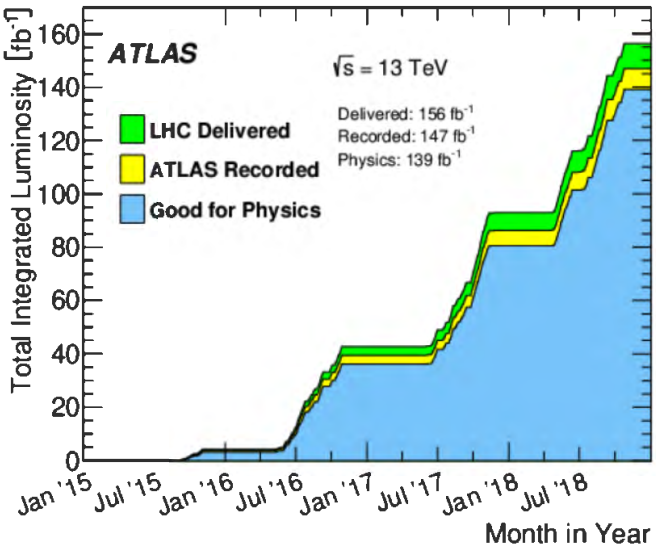

Figure 3.3: A figure of the cumulative luminosity delivered to ATLAS (green), recorded by ATLAS (yellow) and good for physics (blue) are shown over the data taking period of 2015 to 2018 for pp collisions at 13 TeV centre-of-mass energy [4]

barrel and the end-cap. In the barrel region, the detectors are arranged in concentric circles around the beam pipe. In the end-cap region, the detectors are arranged in discs that are perpendicular to the beam pipe.

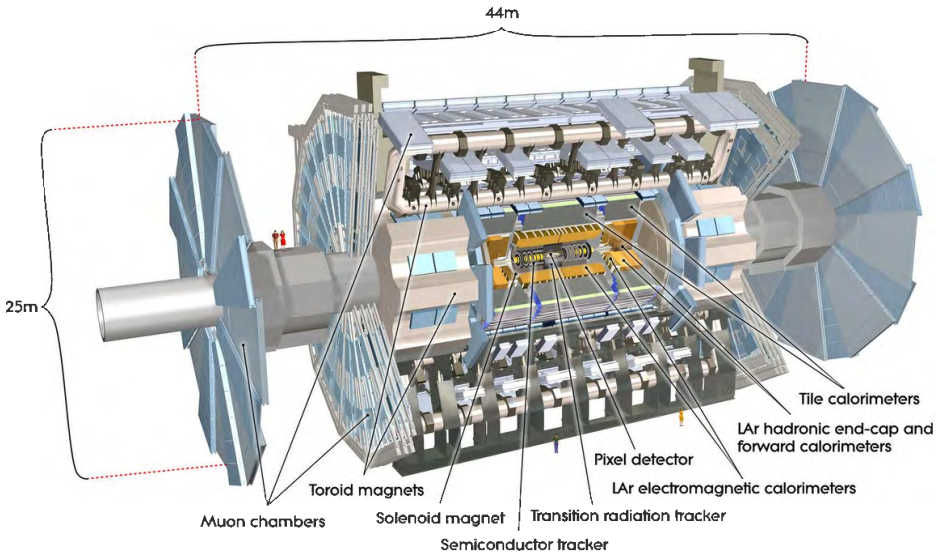

Figure 3.4: A schematic of the internal structure and components of the ATLAS detector are shown [5]

3.2.1 The co-ordinate system

The ATLAS detector uses a right-handed co-ordinate system centred at the interaction point (IP). The z-axis runs in the direction of the beam pipe while the x-y plane is perpendicular to the beam pipe. The x-axis points towards the centre of the LHC ring while the y-axis points upwards. The transverse plane is generally described in terms of the radial distance and the azimuthal angle (r-ϕ) where the azimuthal angle - ϕ - is the angle measured from the x-axis while the radial distance is the distance from the beam pipe. The polar angle (θ) is defined as the angle as measured from the positive z-axis. Figure 3.5 shows the co-ordinate system used at the ATLAS detector.

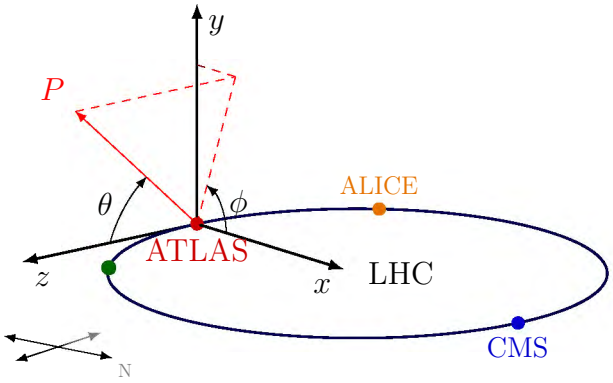

Figure 3.5: A figure showing the co-ordinate system used at the ATLAS detector.

It is a common convention to report the polar angle in terms of the pseudorapidity as shown in equation 3.3.

$$\eta = -\ln\left(\tan\left(\frac{\theta}{2}\right)\right) \tag{3.3}$$

An angular distance is defined using the pseudorapidity and polar co-ordinates and is defined in equation 3.4. The ΔR is the angular distance between object i and j.

$$\Delta R_{ij} = \sqrt{(\eta_i - \eta_j)^2 + (\phi_i - \phi_j)^2} \tag{3.4}$$

3.2.2 Inner detector

The inner detector (ID) is the first detector surrounding the beam pipe [45] and is optimised for the detection and tracking of charged particles with a high degree of accuracy. A high degree of accuracy was achieved as a result of the ID having a high granularity. The required resolution of the ID in terms of p_T is $\sigma_{p_T}/p_T = 0.05\%\ p_T \bigoplus 1\%$ with units of GeV. The high granularity is used to identify primary and secondary vertices and perform pattern recognition. The ID covers the pseudorapidity range of $|\eta| < 2.5$ and is comprised of three separate but complementary sub-detectors. These sub-detectors are the pixel tracker, silicon microstrip (SCT) tracker, and the transition radiation tracker (TRT). Each of these sub-detectors operates within the 2 T axial magnetic field produced by the central solenoid [46]. This powerful magnetic field interacts with charged particles causing their trajectories to curve and allowing their charge and transverse momentum to be measured. Two parameters which are used to identify primary and secondary vertices are the transverse and longitudinal impact parameters given by d_0 and z_0, respectively. The transverse impact parameter is defined as the shortest distance between the track and the z-axis in the x-y plane. The longitudinal impact parameter is defined in the r-z plane and is the distance in z between the primary vertex and the point on the track used to define d_0. Figure 3.6 demonstrates the construction of the impact parameters.

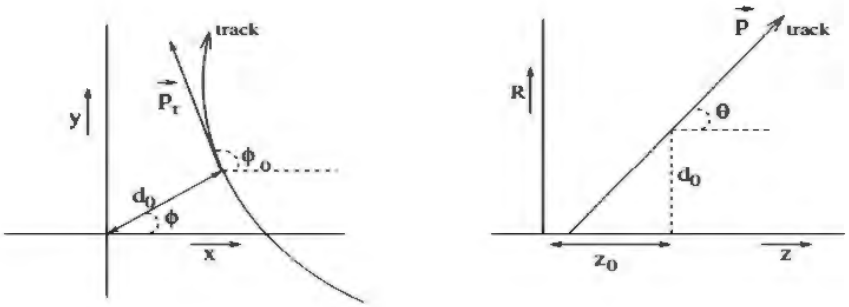

Figure 3.6: A diagram of the transverse and longitudinal impact parameters used at the LHC.

A schematic of the ID is shown in figure 3.7. The inner layers of the ID are comprised of silicon pixel layers followed by stereo pairs of silicon microstrip layers. The outer layer of the ID is the TRT which is comprised of layers of gaseous straw tube elements. The TRT provides continuous tracking over the range $|\eta| < 2.0$. The transition radiation tracker only provides $R - \phi$ information. The information gained from these three sub-detectors is used for pattern recognition and electron identification.

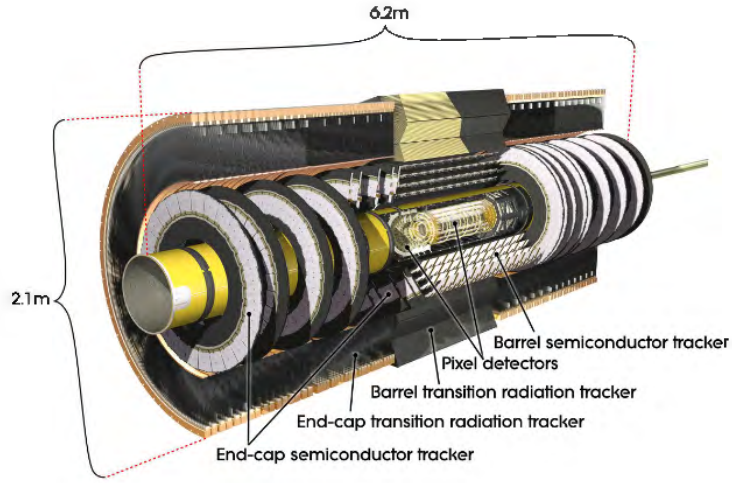

Figure 3.7: A schematic of the internal structure and composition of the inner detector used in the ATLAS detector is shown.

3.2.3 Calorimeters

The calorimeters used in ATLAS cover the range $|\eta| < 4.9$ and are split into two main categories, namely the electromagnetic (ECAL) and hadronic (HCAL) calorimeter. The purpose of these detectors is to identify and measure the energy of both particles and jets. The required resolution of the ECAL in terms of energy is $\sigma_E/E = 10\%/\sqrt{E} \bigoplus 0.7\%$ with units of GeV. The required resolution for the barrel and end-cap of the HCAL in terms of energy is $\sigma_E/E = 50\%/\sqrt{E} \bigoplus 3\%$ with units of GeV. Figure 3.8 provides a diagram showing a labelled cutaway of the calorimeter used in ATLAS.

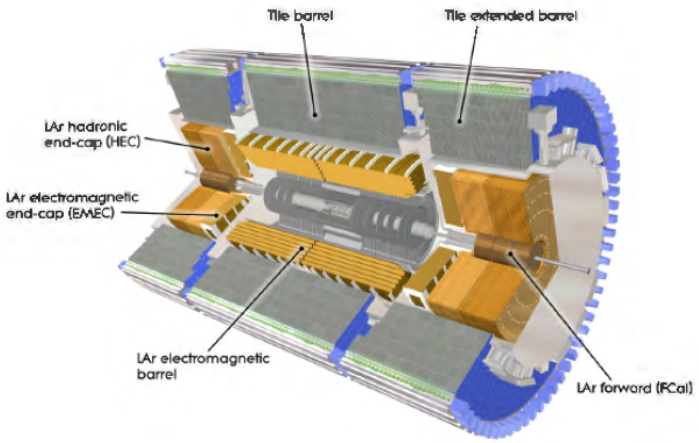

Figure 3.8: A schematic of the internal structure and composition of the calorimeters used in the ATLAS detector is shown.

The ECAL is a high-granularity liquid-argon (LAr) calorimeter that is used for precision measurements of electrons and photons. The ECAL is divided into two sections specifically

the barrel and end-cap. The barrel covers the range $|\eta| < 1.475$, while the end-cap covers the range $1.375 < |\eta| < 3.2$. The HCAL has a coarser granularity than the ECAL which is satisfactory for the reconstruction of jets and the measurement of $E_{\mathrm{T}}^{\mathrm{miss}}$. The HCAL is divided into three sections which are the tile calorimeter (TileCal), the hadronic end-cap (HEC) calorimeters, and the forward calorimeter (FCAL). The required resolution of the FCAL in terms of energy is $\sigma_E/E = 100\%/\sqrt{E} \bigoplus 10\%$ with units of GeV. The TileCAl covers the range $|\eta| < 1.7$ and is made up of plastic scintillator plates. The HEC covers the range $1.5 < |\eta| < 3.2$ while the FCAL covers $3.1 < |\eta| < 4.9$. Both the HEC and FCAL use LAr as their active material.

3.2.4 Muon spectrometer

Muons have a mass approximately 200x larger than the mass of the electron with masses of 105.658 MeV and 0.511 MeV respectively. This larger mass means that muons do not lose nearly as much momentum through bremsstrahlung. This, coupled with the fact that they are leptons and do not interact strongly, means that the muons have much higher penetrating capabilities compared to electrons. It is for this reason that the muon spectrometer (MS) is the most outer sub-detector of the ATLAS detector. The required resolution of the MS in terms of p_T is $\sigma_{p_T}/p_T = 10\%\ p_T$ with units of GeV at $p_T = 1$ TeV. The air-core toroidal magnets around the barrel and end-cap regions result in the MS being bathed in a 0.5-1 T magnetic field. Figure 3.9 provides a cutaway view of the layout of the muon spectrometer and its sub-detectors.

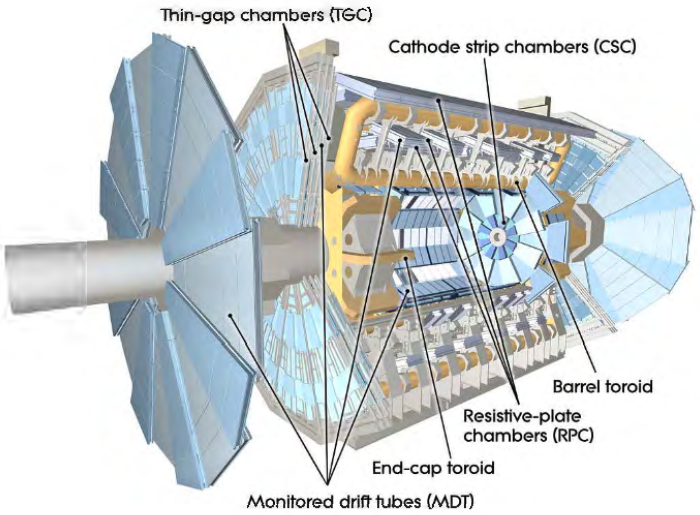

Figure 3.9: A schematic of the internal structure and composition of the muon spectrometer used in the ATLAS detector is shown.

The MS covers the range $|\eta| < 2.7$ and is able to trigger on muons in the range $|\eta| < 2.4$.

The sub-detectors of the MS are the resistive plate chambers (RPC) [47], thin gap chambers (TGC) [48], monitored drift tube (Monitored Drift Tube chambers (MDT)) [49] chambers and the cathode strip chambers (Cathode Strip Chambers (CSC)) [50]. The precision measurements in the MS use the MDT and CSC while the triggering uses the RPC and the TGC. The MDT covers the pseudorapidity range $|\eta| < 2.7$. In the innermost end-cap layer the coverage is limited to $|\eta| < 2.0$. The CSC covers the range $2.0 < |\eta| < 2.7$ and has a higher granularity than the MDT to deal with higher background rates in this region.

3.2.5 Trigger and data acquisition

Several constraints limit the amount of data that can be recorded at the LHC. Interactions at the LHC occur at a frequency of 40 MHz, however due to technological constraints and resource limitations, data can only be recorded at a rate of 200 Hz [41]. To reduce this rate, the trigger system is used to identify interactions of interest. The trigger system is composed of the Level-1 (L1) trigger [51] and the High-Level Trigger (HLT) [52]. The Level-1 trigger is a hardware-based system that selects interactions containing high p_T muons, electrons, photons, jets, and τ leptons decaying into hadrons as well as interactions with large amounts of missing transverse energy. High p_T muons are selected using information from the RPC and TGC, while information from all the calorimeter subsystems is used to select the remaining objects. The L1 selection reduces the event rate from 40 MHz to 75 kHz. The HLT is a software-based system that consists of two parts the Level-2 (L2) trigger and an event filter. The L2 trigger utilises information such as co-ordinates and energy of the objects to further reduce the event rate to below 3.5 kHz. The event filter uses additional algorithms to further reduce the rate to 200 Hz which are then stored for offline analysis.

3.2.6 Pile-up

On average 33 interactions will occur per bunch crossing at the LHC. Of the interactions, only one interaction is considered a signal interaction and corresponds to the reconstructed vertex with the highest $\sum p_T^2$. The rest of the interactions are considered background and are called pile-up. Pile-up is categorised into two categories which are in-time and out-of-time pile-up. In-time pile-up corresponds to the pp interactions that occur in the same bunch crossing, while out-of-time pile-up corresponds to interactions that occur from different bunch crossings. When simulating the physics process as outlined in section 2.3, pile-up needs to be taken into account to ensure that the simulation models the data well. Figure 3.10 shows the distribution of the mean number of interactions per bunch crossing for data taken during 2015 to 2018 at $\sqrt{s}$ =13 TeV.

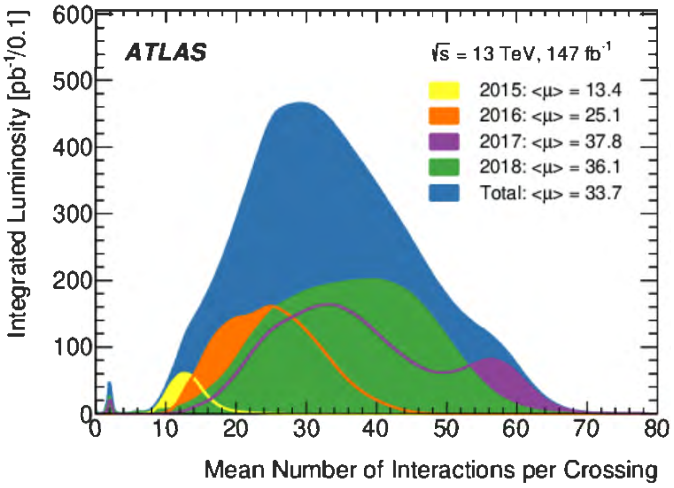

Figure 3.10: The luminosity-weighted distributions of the mean number of interactions per bunch crossing are shown for data taken during 2015 to 2018 period at $\sqrt{s}$ =13 TeV [4].

Chapter 4

The $t\bar{t}W^{\pm}$ process and charge asymmetry

This chapter introduces the key concepts of this measurement which are the pp $\rightarrow t\bar{t}W^{\pm}$ process and related charge asymmetry. A firm grasp of the physics underlying these two concepts provides the basis for the rest of the measurement presented in this dissertation. The $t\bar{t}W^{\pm}$ process is discussed and presented in section 4.1. This section provides a general outline of the $t\bar{t}W^{\pm}$ process followed by a discussion of previous measurements of the $t\bar{t}W^{\pm}$ cross section. Section 4.2 introduces the concept of charge asymmetry which is related to a difference in the angular distribution of the top quark as compared to the top anti-quark. A discussion of the theoretical predictions behind a charge asymmetry in top quark pair production is presented in 4.2.1. This is followed by a discussion of the previous measurements of the charge asymmetry in $t\bar{t}$, as shown in section 4.2.2. A comparison between the $t\bar{t}$ and $t\bar{t}W^{\pm}$ process is presented in section 4.2.3. Finally, a discussion of the leptonic charge asymmetry in $t\bar{t}W^{\pm}$ is presented in section 4.3.

4.1 The $t\bar{t}W^{\pm}$ process

The production of a top quark pair ($t\bar{t}$) in association with a W boson is a rare process with a cross section as predicted by the SM given by 0.628 ± 0.082 fb [9]. The second run of the LHC has recorded the largest pp at $\sqrt{s} = 13$ TeV data set of 139 fb^{-1}. This large data set provides an opportunity to further investigate in the rare $t\bar{t}W^{\pm}$ process. Figure 4.1 shows an example of the Feynman diagram for the $t\bar{t}W^{\pm}$ process at leading order (LO). At leading order, the emission of the W boson in the initial state requires that the $t\bar{t}W^{\pm}$ process is produced by a quark anti-quark ($q\bar{q}$) initial state. The qg initial state contributes to the $t\bar{t}W^{\pm}$ process at next-to-leading order (NLO) while the gg initial state contributes at next-to-next-to-leading order (NNLO). This means that the $q\bar{q}$ initial state is the dominant initial state for the $t\bar{t}W^{\pm}$ process.

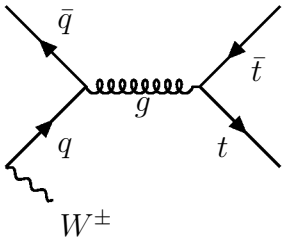

Figure 4.1: A Feynman diagram of the of $t\bar{t}W^{\pm}$ process at leading order is shown

The $t\bar{t}W^{\pm}$ process provides several observables which are sensitive to new physics. Several measurements of the $t\bar{t}W^{\pm}$ cross section have been used to investigate and constrain BSM models at both ATLAS [53] and CMS [9]. The A_C^{ℓ} observable provides independent constraining power when compared to the cross section. The BSM physics to which the A_C^{ℓ} observable is sensitive is the axigluon [19] as well as several operators in the EFT framework [9]. The $t\bar{t}W^{\pm}$ process is also sensitive to the electroweak coupling to the top quark due to a tW scattering which occurs at NLO [54, 55]. The $t\bar{t}W^{\pm}$ process is an important background in several BSM studies as well as to the $t\bar{t}H$ process which is defined as a top quark pair produced association with a Higgs boson. Hence better measurements of the $t\bar{t}W^{\pm}$ process could lead to improved constraints on BSM models such as those mentioned in section 2.2 and more precise measurements of $t\bar{t}H$.

4.1.1 Previous measurements of the $t\bar{t}W^{\pm}$ cross section

Previous measurements of the $t\bar{t}W^{\pm}$ cross section have been performed at the LHC and will be discussed as follows. The $t\bar{t}W^{\pm}$ process at $\sqrt{s} = 8$ TeV was observed at the LHC using both the ATLAS and CMS detectors [53, 56]. These studies observed $t\bar{t}W^{\pm}$ with significances of 5.0σ and 4.8σ respectively. Measurements of the $t\bar{t}W^{\pm}$ differential cross sections at $\sqrt{s} = 13$ TeV were performed at the LHC using the ATLAS [6, 7] and CMS [8, 9] collaborations. The ATLAS collaboration performed two measurements, one with an integrated luminosity of 3.2 fb^{-1} and a second with 36 fb^{-1}. The CMS collaboration also performed two measurements with 13 fb^{-1} and 36 fb^{-1} respectively. A summary of the cross sections measured by the ATLAS and CMS collaborations is presented in figure 4.2. Figure 4.2 shows the theoretical prediction from the SM in red with the uncertainties shown by a yellow band. The measurements are ordered from lowest luminosity at the top to highest at the bottom. For clarity measurements taken by ATLAS are shown in orange and CMS in blue. The values measured and their uncertainties, both statistical and systematic, are quoted on the left for each measurement. The corresponding luminosity for each is shown on the right-hand side of the plot.

Figure 4.2 shows that as the amount of data increases the measured cross sections begin to approach that predicted by the SM. Further theoretical studies into the $t\bar{t}W^{\pm}$ cross

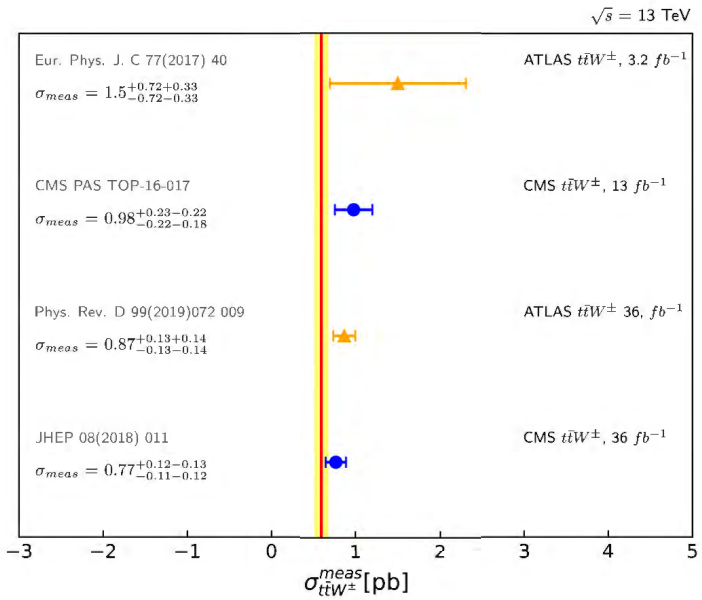

Figure 4.2: A figure summarising of the cross section measurements of the $t\bar{t}W^{\pm}$ process performed at the LHC at a centre-of-mass energy of $\sqrt{s} = 13$ TeV is shown. The measurements were performed using the ATLAS and CMS experiments shown in orange and blue respectively. For each measurement the cross section, uncertainties and luminosity are shown. The error bars presented use both statistical and systematic uncertainties [6, 7, 8, 9]

section have indicated that subleading electroweak corrections could cause the predicted cross section to increase by approximately 5% [57]. Increasing the integrated luminosity has two effects on the cross section measurement as shown in figure 4.2. The first effect is that the statistical uncertainties decrease with the second effect being that the measurements approach the value predicted by the SM. It should be noted that all of the measurements show an excess above the prediction, however, the theory and measurement agree within one standard deviation across all measurements. A deeper investigation of the $t\bar{t}W^{\pm}$ process through the charge asymmetry will provide an independent insight into the process.

4.2 Charge asymmetry

The charge asymmetry investigated in this measurement refers to the difference in angular distributions of the top quark and the top anti-quark in the production of top quark pairs. The theoretical predictions of the charge asymmetry in top quark pair production is outlined in section 4.2.1. Previous measurements of the charge asymmetry have been conducted in the $t\bar{t}$ process and the results of these measurements are presented in section 4.2.2. This is followed by a comparison between the $t\bar{t}$ and $t\bar{t}W^{\pm}$ process in section 4.2.3.

4.2.1 Theoretical predictions for charge asymmetry

The origins of the charge asymmetry in $t\bar{t}$ will be discussed in the following paragraphs but will also apply to the $t\bar{t}W^{\pm}$ process. The charge asymmetry arises as a result of a correlation between the initial and final state particles. The implication of this correlation is that an imbalance in the initial state results in a difference in the angular distributions of the top quark and top anti-quark in the final state. The initial states which produce a $t\bar{t}$ pair are the gluon-gluon (gg), quark anti-quark ($q\bar{q}$), and quark-gluon (qg) initial states. The charge asymmetry is dominantly produced in the $q\bar{q}$ initial state while the gg initial state is completely symmetric. An outline of the underlying physics that produces the asymmetry is presented in terms of $q\bar{q}$. The correlation between initial and final states arises due to interference between Feynman diagrams. The diagrams that contribute to the charge asymmetry in the production of heavy quarks $Q\bar{Q}$ are shown in figure 4.3. In figure 4.3, diagrams (a) and (b) represent the final and initial state gluon bremsstrahlung, respectively. Diagrams (c) and (d) represent the box and born-level diagrams. The interference between Feynman diagrams occurs between the final (a) and initial (b) state gluon bremsstrahlung as well as an interference between the box (c) and born-level diagrams (d) as shown in figure 4.3. These two sets of interferences are the underlying cause of the correlation between the initial and final states in $t\bar{t}$.

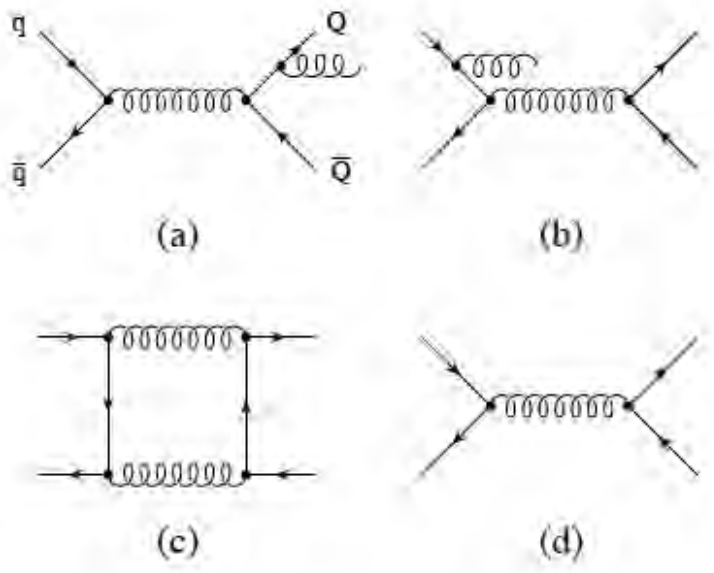

Figure 4.3: Feynman diagrams which contribute to the charge asymmetry in the production of heavy quarks $Q\bar{Q}$ [10] are shown. These diagrams correspond to the final-state (a) and initial-state (b) gluon brehmsstrahlung as well as the box (c) and born-level (d) diagrams.

The LHC is a proton-proton collider. Since the proton is made of two up quarks and a down quark - none of which are anti-quarks - the anti-quarks need to be produced in additional processes. Such a process is a gluon radiation from one of the quarks in the

proton which can then decay into a $q\bar{q}$ pair. As a result, the momenta of the anti-quarks are - on average - lower than that of the quarks. This causes a momenta imbalance between the q and $\bar{q}$. Since the initial and final states of the $t\bar{t}$ process are correlated this momenta imbalance propagates to the final-state, which leads to the η distributions of the top quark and top anti-quark to differ. The top quark, on average, tends to be emitted with a larger η as compared to the top anti-quark which is emitted with a smaller η. This difference in η distributions is then defined in terms of the charge asymmetry shown in equation 4.3.

4.2.2 Previous measurements of charge asymmetry in $t\bar{t}$

The first measurement of a charge asymmetry in $t\bar{t}$ was performed at the Tevatron using the CDF and DØ experiments [58, 59, 60]. The Tevatron is a proton-anti-proton ($p\bar{p}$) collider, resulting in protons always coming from one side of the detector while the anti-protons will come from the other side. This produces an imbalance in the initial state as well as a preferred direction for the decay of top quarks versus top anti-quarks. To capture this asymmetry a Forward-Backward (A_{FB}) asymmetry is defined for top quarks in equation 4.1. Due to the mass of the top quark the charge asymmetry is defined in terms of rapidity.

$$A_{FB} = \frac{N(\Delta_y^t > 0) - N(\Delta_y^t < 0)}{N(\Delta_y^t > 0) + N(\Delta_y^t < 0)} \tag{4.1}$$

Where $\Delta_y^t = y_t - y_{\bar{t}}$. The charge asymmetry can also be calculated in terms of the decay products of the top quarks which are the leptons and b-jets (ℓ, b). When using the decay products of the top quarks the charge asymmetry is calculated in terms of the pseudorapidity (η). The equation for the A_{FB} in terms of leptons is shown in equation 4.2.

$$A_{FB}^{\ell} = \frac{N(\Delta_\eta^\ell > 0) - N(\Delta_\eta^\ell < 0)}{N(\Delta_\eta^\ell > 0) + N(\Delta_\eta^\ell < 0)} \tag{4.2}$$

Where $\Delta_\eta^t = \eta_{\ell_t} - \eta_{\ell_{\bar{t}}}$. Figure 4.4a shows the summary of the results obtained from the Tevatron [11]. The SM predictions with their uncertainties are shown as a purple band. The measurements by CDF and DØ are shown with black dots and the uncertainties as horizontal lines. The top part of the figure refers to measurements of the A_{FB}^{ℓ} while the bottom refers to the A_{FB}. Figure 4.4a shows that there is a slight tension between the measured asymmetries and those predicted by the SM. The "naive world average" - as shown in red - shows an error-weighted average of the asymmetries measured and indicates an asymmetry larger than that of the SM and does not agree within one standard deviation. The tension

between the measurement and prediction of the A_{FB} at the Tevatron resulted in further measurements of the charge asymmetry in $t\bar{t}$ at the LHC. Since the LHC is a proton-proton collider the charge asymmetry differs from that measured at the Tevatron. The first difference is that there is no preferred direction for the top quark and the top anti-quark at the LHC. This means that the A_{FB} defined at the Tevatron vanishes at the LHC due to the symmetry of the initial state. The imbalance in the initial state at the LHC is due to a difference in the average momenta of the initial state quarks where the momenta of the initial state quarks are on average larger than the initial state anti-quarks. The implication of the momentum imbalance is that top quarks will, on average, decay with a larger rapidity as compared to top anti-quarks which will decay with a smaller rapidity. To account for these differences, a "forward-central" charge asymmetry (A_C) for top quarks is defined in equation 4.3 [11, 61, 62] in terms of the rapidity.

$$A_C = \frac{N(\Delta_y^t > 0) - N(\Delta_y^t < 0)}{N(\Delta_y^t > 0) + N(\Delta_y^t < 0)} \tag{4.3}$$

Where $\Delta_y^t = |y_t| - |y_{\bar{t}}|$. Similarly to the Tevatron, the charge asymmetry at the LHC can be defined using the decay products of the top quarks in terms of pseudorapidity. The equation for the leptonic charge asymmetry at the LHC is given in equation 4.4.

$$A_C^\ell = \frac{N(\Delta_\eta^\ell > 0) - N(\Delta_\eta^\ell < 0)}{N(\Delta_\eta^\ell > 0) + N(\Delta_\eta^\ell < 0)} \tag{4.4}$$

Where $\Delta_\eta^\ell = |\eta_{\ell_t}| - |\eta_{\ell_{\bar{t}}}|$. Measurements of both the A_C and the A_C^ℓ have been performed using the ATLAS and CMS experiments at $\sqrt{s} = 7{,}8$ TeV [25, 63, 64, 65]. Figure 4.4b provides a summary of the charge asymmetries investigated at the LHC. The SM prediction is indicated by the purple band, while the measurements and their uncertainties are shown with the black dots. The top portion of the figure refers to the A_C^ℓ and the bottom refers to the A_C. Only one of the measurements was performed at $\sqrt{s} = 8$ TeV and was performed using the CMS experiment. The "naive world average" shown in red only includes measurements done at 7 TeV in figure 4.4b. The results presented in figure 4.4b are in good agreement with the SM predictions. More recent measurements of the A_C have been performed at the LHC at a centre-of-mass energy $\sqrt{s} = 13$ TeV. This was performed using the ATLAS experiment and extracted the top quark charge asymmetry in $t\bar{t}$ [66]. The measured top quark charge asymmetry was $A_C = 0.60\% \pm 0.15$ % which included both statistical and systematic uncertainties [67] was found to be in good agreement with the SM prediction of $0.45\%^{+0.09\%}_{-0.06\%}$ [12].

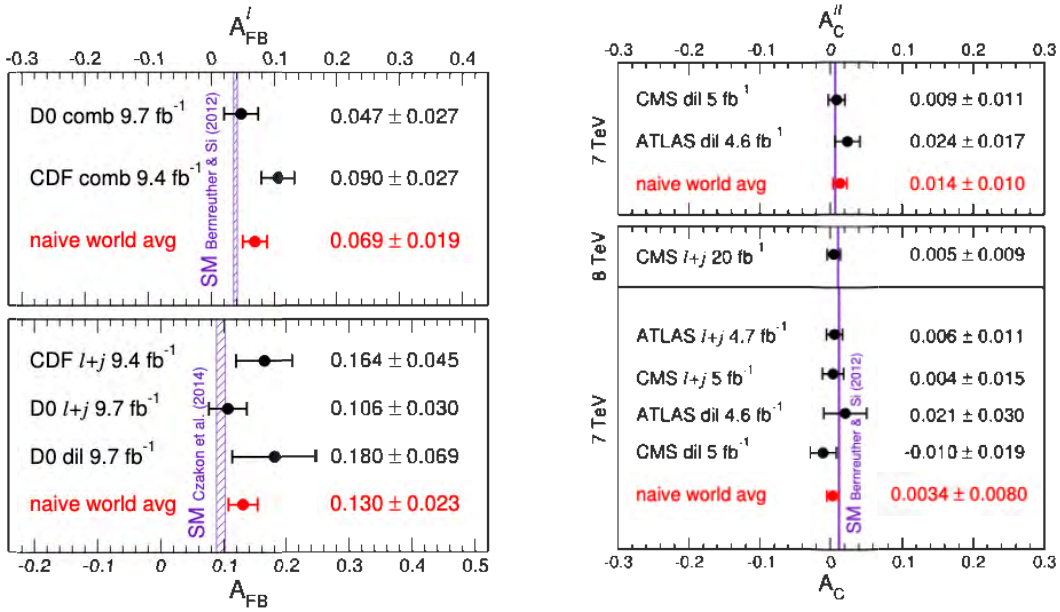

(a) Tevatron (b) LHC

Figure 4.4: A figure summarising the measurements of the A_{FB} at the Tevatron using the CDF and DØ experiments and the A_C at the LHC using the ATLAS and CMS experiments is shown. These measurements were performed for both the leptonic and top quark charge asymmetries. The "naive world average" is shown in red and correspond to an an error-weighted average of the asymmetries measured. In figure (b) the 'naive world averages" corresponds only to the 7 TeV measurements. [11].

4.2.3 A comparison between the $t\bar{t}$ and $t\bar{t}W^{\pm}$ processes

Thus far the discussion of the charge asymmetry, both theory and measurement, has been in terms of the $t\bar{t}$ process. This section highlights the differences between the $t\bar{t}W^{\pm}$ and $t\bar{t}$ processes as well as the implications of these differences on the charge asymmetry. One of the disadvantages of $t\bar{t}W^{\pm}$, when compared to $t\bar{t}$, is the cross section. The predicted cross sections at NLO in QCD for $t\bar{t}$ and $t\bar{t}W^{\pm}$ differ by several orders of magnitude and are 661 pb and 0.678 pb [12]. The implication of this is that a measurement of the charge asymmetry in $t\bar{t}W^{\pm}$ could be limited by the size of the data set used. The advantage of the $t\bar{t}W^{\pm}$ process over the $t\bar{t}$ process is the predicted size of the charge asymmetry. As stated in section 4.2.1, the $q\bar{q}$ initial state plays a dominant role in charge asymmetry. The $t\bar{t}$ process is dominated by gg at LO with $q\bar{q}$ only contributing at NLO. By comparison the $t\bar{t}W^{\pm}$ process is dominated by $q\bar{q}$ at LO, the qg initial state contributes at NLO and only at NNLO does the symmetric gg initial state contribute. Table 4.1 shows a comparison between the $t\bar{t}$ and $t\bar{t}W^{\pm}$ processes for the cross section and charge asymmetry at centre-of-mass energies of 8 TeV and 13 TeV. The A_C^{ℓ} is also shown for the $t\bar{t}W^{\pm}$ process. This difference in initial state contributions causes the predicted top quark charge asymmetry to be approximately five times smaller in the $t\bar{t}$ process as compared to the $t\bar{t}W^{\pm}$ process as shown in table 4.1. A second advantage of the $t\bar{t}W^{\pm}$ process is due to the radiation of the W boson from the initial state, which acts as a polariser within the $t\bar{t}W^{\pm}$ process. The polarisation results in an angular correlation between the decay products and the spin orientation of the top quark and top anti-quark respectively. The correlation results in the angular distributions of the decay products of the top quarks displaying noticeably different η distributions at LO [12]. Referring to table 4.1 the sign of the A_C^{ℓ} is flipped when compared to A_C and is approximately six times larger. The comparatively large size of the A_C^{ℓ} in $t\bar{t}W^{\pm}$ coupled with the precision measurement of leptons in ATLAS makes the A_C^{ℓ} observable ideal for investigating the $t\bar{t}W^{\pm}$ process.

		8 TeV	13 TeV
$t\bar{t}$	$\sigma(pb)$	198	661
	$A_C^t(\%)$	0.72	0.45
$t\bar{t}W^{\pm}$	$\sigma(pb)$	0.587	0.678
	$A_C^t(\%)$	2.37	2.24
	$A_C^{\ell}(\%)$	-14.83	-13.16

Table 4.1: A table comparing the charge asymmetry [%] and cross section [pb] for $t\bar{t}$ and $t\bar{t}W^{\pm}$ is shown. [12] The leptonic charge asymmetry is also shown for the $t\bar{t}W^{\pm}$ process.

4.3 The A_C^ℓ in $t\bar{t}W^\pm$

To measure the A_C^ℓ in $t\bar{t}W^\pm$, the information regarding the two leptons that decay from top quarks are required. The leptons decaying from the top quark pair have an opposite sign (OS) and as a result, there are only two channels from which the A_C^ℓ can be measured. These two channels are the two OS lepton (2ℓ OS) and the three lepton (3ℓ) channels. The channel chosen for this measurement is the 3ℓ channel. The reason behind this choice is that it has been assumed in this dissertation that the 2ℓ OS channel will have a much larger background contribution as compared to the 3ℓ channel in the form the $t\bar{t}$ plus jets and the Z plus jets processes. As a result the 2ℓ OS would have a lower signal purity than the 3ℓ channel and as a result will have larger uncertainties on the measurement of A_C^ℓ. The Feynman diagram in figure 4.5 shows the trilepton final state of the $t\bar{t}W^\pm$ process where all three W bosons have decayed leptonically. One of the main challenges in measuring the A_C^ℓ in the 3ℓ channel is identifying the leptons that decayed from top quarks. It should be noted that there will be the OS leptons decaying from the top quarks and the charge of the ISW can be either positive or negative. From this, it can be seen that there will always be two same-sign leptons and one lepton with an opposite sign to the other two. As a result, one of the leptons decaying from top quarks can be identified as a result of its charge. The remaining lepton decaying from a top quark will require a lepton-top association. If the two leptons which decay from top quarks are selected at random, the asymmetry will be severely diluted as the orientation of the ISW lepton is random with respect to the leptons decaying from top quarks. The more efficiently leptons that decay from top quarks can be identified corresponds to a greater sensitivity to the A_C^ℓ.

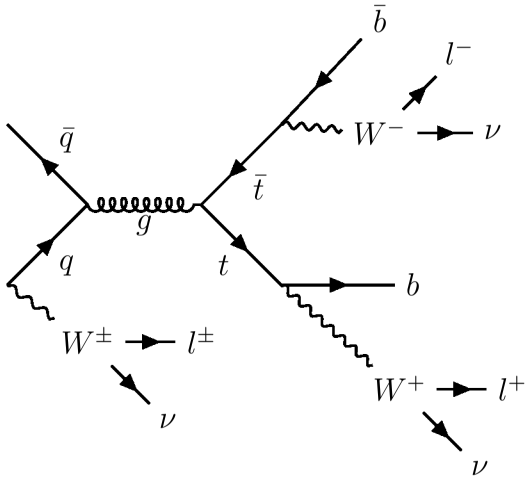

Figure 4.5: A Feynman diagram of the trilepton final state of $t\bar{t}W^\pm$ at leading order is shown.

Chapter 5

The measurement of the leptonic charge asymmetry in $t\bar{t}W^{\pm}$ using the trilepton final state

This chapter presents the measurement of the A_C^ℓ in $t\bar{t}W^{\pm}$. In section 5.1, information regarding the data and simulation, such as the period of data acquisition, the size of the data set, as well as the simulation samples used, are provided. An outline of the strategy used to measure the A_C^ℓ is given in 5.2. In section 5.3 the definition of the objects used in this measurement including the charged leptons, jets, $E_{\mathrm{T}}^{\mathrm{miss}}$ and overlap removal is discussed. The event-selection criteria are detailed in section 5.4 including the triggers, the signal and control regions, and the normalization and calibration of the simulation. One of the prominent backgrounds is top quark pair production ($t\bar{t}$) with an additional fake lepton. Hence section 5.5 discusses the method used to estimate fake leptons. To ensure that the simulation accurately models the data, section 5.6 studies the agreement between data and simulation in the control region. Section 5.7 discusses the strategy of identifying leptons decaying from top quarks. This section demonstrates the different methods investigated for the lepton-top association and the efficiency of each method. In section 5.8, the two methods used to measure the A_C^ℓ are discussed as well as a brief introduction to maximum likelihood estimation.

5.1 Data and simulation

The data used in this measurement consist of proton-proton collisions at a centre-of-mass energy of 13 TeV. The ATLAS experiment recorded this data set during Run 2 of the LHC between 2015 and 2018 and this data set is referred to as the full Run 2 data set. Only events which were stored during a good run of the LHC, as discussed in section 3.1, are used in this measurement. The total integrated luminosity for the full run 2 using only events recorded during good runs is 139 fb^{-1} [68]. Each year has different conditions of data acquisition and

as a result, it is useful to consider the integrated luminosity corresponding to each year of data acquisition which is shown in table 5.1. The distribution of pile-up differs from year to year which needs to be taken into account to ensure the simulation is calibrated correctly. Hence each of the samples is simulated and calibrated on a year-by-year basis. The uncertainty of the total integrated luminosity recorded during the data acquisition period of 2015 - 2018 is 1.7%. This uncertainty was obtained using the LUCID-2 detector [69] for the primary luminosity measurements where LUCID-2 is the luminosity Cherenkov integrating detector.

Year	$\int \mathcal{L}$ dt [fb^{-1}]
2015	3.219
2016	32.988
2017	44.307
2018	58.45

Table 5.1: A table showing the total integrated luminosity recorded by the ATLAS detector on a year-by-year basis.

When events are recorded, only the final state objects are detected and stored. Although the detector measures objects in the final state of a process, however, the detector is unable to identify the underlying process which produced final state objects. This results in the data being composed of several processes. To accurately describe the data, all of the physics processes which contribute must be simulated. This simulation can then be used to estimate the expected amounts of signal and background events as well as testing hypotheses, such as the SM and BSM theories. By estimating the likelihood of the data under different hypotheses, statistical statements can be constructed concerning the validity of these hypotheses. The following paragraphs will outline the simulations used in this measurement. For each process simulated the matrix element generator, parton shower [70], and parton distribution function (PDF) set used will be listed. The first process introduced will be the signal simulation ($t\bar{t}W^{\pm}$) followed by the background simulation in descending order of importance.

The $t\bar{t}W^{\pm}$ process is modelled using the MG5_aMC@NLO 2.3.3 generator [34]. This simulation is calculated at next-to-leading order (NLO) in QCD with one additional jet and uses the NNPDF.3.0nnlo PDF set [71]. The NLO simulation is then interfaced with PYTHIA 8.210 [35] for the parton showering. A second $t\bar{t}W^{\pm}$ sample is included to train a machine learning algorithm and was produced using SHERPA 2.2.8 [36]. This simulation was calculated at NLO for $t\bar{t}W^{\pm}$ plus one and two jets and was interfaced with the SHERPA parton showering software. These two samples differ in the number of jets included at the matrix-element level. This difference causes the jet kinematics to differ between the two samples. The SHERPA sample has on average a higher jet multiplicity when

compared to the MADGRAPH sample. The $t\bar{t}$ process is simulated at NLO in QCD using POWHEG [37]. The PDF set used is NNPDF3.0NNLO and the parton shower is simulated using PYTHIA 8.230. The $t\bar{t}$ process decays into $t\bar{t} \to W^+bW^-\bar{b}$ where both W bosons are required to decay leptonically. Since this measurement focuses on the trilepton channel, the third lepton in $t\bar{t}$ will be a fake lepton 100% of the time. This sample has been included to help model the fake contribution within the A_C^ℓ measurement. The $t\bar{t}Z$ sample is simulated at NLO in QCD using MG5_aMC@NLO 2.3.3 and is one of the dominant backgrounds of this measurement. The PDF set used is NNPDF.3.0NNLO and the parton shower is simulated with PYTHIA 8.210. The Z + jets process is simulated using SHERPA 2.2.1 at NLO in QCD. The PDF set used is NNPDF.3.0NNLO and the parton shower is simulated using SHERPA. This sample is used in conjunction with the $t\bar{t}$ sample to estimate the contribution from events containing fake leptons. The tWZ process is simulated at NLO in QCD using MG5_aMC@NLO 2.3.3. The PDF set used is NNPDF.3.0NNLO and the parton shower was simulated using PYTHIA 8.235. It should be noted that the interference between tWZ and $t\bar{t}Z$ was removed using the diagram removal scheme called DR1 [72] that was applied to the tWZ sample. A summary all of the processes which were used in this measurement is presented in table 5.2. This table outlines the processes included in this measurement where the generator, parton showering, and PDF set are listed for each sample. The order in QCD in which the processes are simulated is also included.

Process	**Generator**	**Order in QCD**	**Parton shower**	**PDF**
$t\bar{t}W^\pm$	MG5_aMC@NLO 2.3.3	NLO	PYTHIA 8.210	NNPDF.3.0NNLO
	SHERPA 2.2.8	NLO	SHERPA	NNPDF.3.0NNLO
$t\bar{t}$	POWHEG	NLO	PYTHIA 8.230	NNPDF.3.0NNLO
$t\bar{t}Z$	MG5_aMC@NLO 2.3.3	NLO	PYTHIA 8.210	NNPDF.3.0NNLO
$WZ/ZZ+$ jets	SHERPA 2.2.2	NLO	SHERPA	NNPDF.3.0NNLO
$t\bar{t}H$	MG5_aMC@NLO 2.6.0	NLO	PYTHIA 8.230	NNPDF.3.0NNLO
tZ	MG5_aMC@NLO 2.3.3	NLO	PYTHIA 8.230	NNPDF.3.0NNLO
tWZ	MG5_aMC@NLO 2.3.3	NLO	PYTHIA 8.235	NNPDF.3.0NNLO
$t\bar{t}WW$	MG5_aMC@NLO 2.2.2	LO	PYTHIA 8.186	NNPDF.2.3LO [73]
$H + W/Z$	PYTHIA 8.186	LO	PYTHIA 8.186	NNPDF.2.3LO
VVV $(V = W/Z)$	SHERPA 2.2.2	NLO	SHERPA	NNPDF.3.0NNLO
ttt, $t\bar{t}t\bar{t}$	MG5_aMC@NLO 2.2.2	LO	PYTHIA 8.186	NNPDF.2.3LO
Z + jets	SHERPA 2.2.1	NLO	SHERPA	NNPDF.3.0NNLO

Table 5.2: A table presenting the simulated processes used in this measurement. For each process the generator, parton shower, order in QCD, and PDF set are presented.

5.2 Measurement strategy

This section details the strategy for the measurement of the A_C^ℓ in $t\bar{t}W^\pm$. The measurement can be broken down into several steps. A flow chart outlining the steps taken is shown in 5.1. As seen in the flowchart below the first step is the event selection. The event selection places criteria on the simulation and background to create signal and control regions. The criteria on signal regions are such that the region maximises $t\bar{t}W^\pm$ while minimising the background processes. These criteria will exploit the physics of the $t\bar{t}W^\pm$ system to differentiate it from the background processes. The criteria required for control regions produce regions that are enriched in dominant background processes such as $t\bar{t}$ and $t\bar{t}Z$. This is implemented to precisely evaluate and calibrate the background simulations and minimizes the uncertainties associated with the background processes. Following the event selection, the leptons that decay from top quarks need to be identified via the lepton-top association. The lepton-top association exploits the physics of the top quark system to differentiate between leptons produced by top quark decays and leptons from ISW boson decays in $t\bar{t}W^\pm$. The differentiation is done using a machine learning algorithm to combine the lepton information and score each lepton. The higher the score the more likely it is that the lepton decayed from a top quark. The two top leptons are then selected using the machine learning score. This will allow the Δ_η^ℓ to be reconstructed to calculate the A_C^ℓ shown in equation 4.4. To increase the sensitivity of this measurement to the $t\bar{t}W^\pm$ process an event-level BDT is trained with the purpose of differentiating background from signal processes. The final step is the extraction of the A_C^ℓ from the reconstructed Δ_η^ℓ distribution. The signal and control regions will be split up based on whether the event has a positive or negative Δ_η^ℓ. Each region will be binned in terms of the output of the event-level BDT and the yields from the regions with positive and negative Δ_η^ℓ will be extracted. These yields will then be used to calculate the A_C^ℓ and its uncertainties. The method of extraction outlined above is called the Fit Across Regions (FAR). A second method of extraction was also investigated and is called Template Morphing (TM).

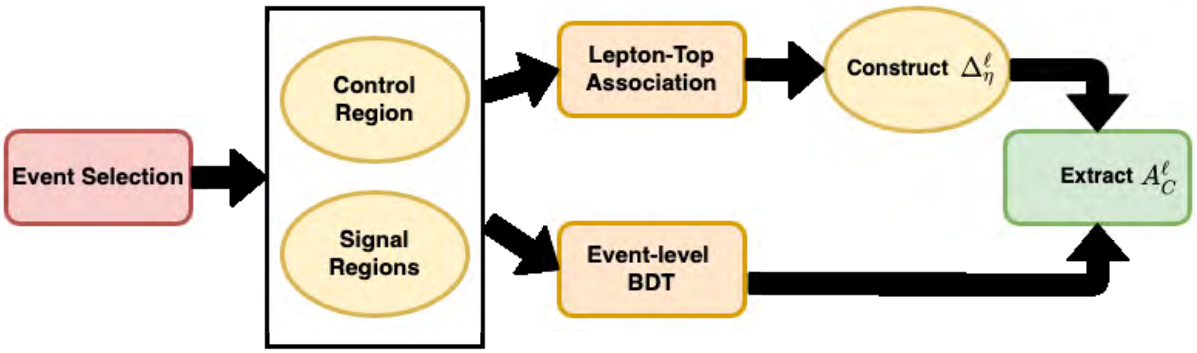

Figure 5.1: A flow chart of the strategy implemented to measure the A_C^ℓ is shown.

5.3 Object reconstruction and identification

The objects used in this measurement are charged leptons, jets and $E_{\mathrm{T}}^{\mathrm{miss}}$. For an object to be considered in this measurement is must pass a set of criteria which will be detailed in the following subsections.

5.3.1 Charged leptons

The leptons which are used in this measurement are the electron and muon. The tau lepton is not considered in this measurement as the tau lepton decays before interacting with the detector and would need to be reconstructed to be included in this measurement. Electrons are particles that are reconstructed from energy deposits in the electromagnetic calorimeter which are then matched to tracks within the inner detector. Electrons are required to have a p_T greater than 10 GeV and an $\eta < 2.47$. Electrons in the region $1.37 < |\eta| < 1.57$ are excluded from this measurement. A likelihood-based (LH) identification is used to select prompt electrons [74, 75]. The LH identification uses information from both the tracking and calorimeter sub-detectors to identify prompt electrons where prompt leptons are defined as leptons that originate from the primary vertex. There are several working points available for LH identification that correspond to identifying a prompt electron with $E_{\mathrm{T}}^{\mathrm{miss}}$ = 40 GeV. The available working points are `Loose`, `Medium`, and `Tight` which correspond to efficiencies of 93%, 88%, and 80%. Pre-selected electrons in this measurement are chosen using a variation of the `Loose` WP - called `LooseAndBLayerLH`, which uses the same `Loose` WP but has the extra requirement of a hit in the innermost pixel layer. For electrons, the `Tight` LH identification WP is required. Electrons are required to be isolated from other particles via the PromptLeptonVeto (PLV) algorithm. The PLV algorithm is a multivariate algorithm that matches electrons and muons to track jets where a track jet is a jet associated with tracks that have been detected within the inner detector. The PLV algorithm is used to distinguish prompt electrons from hadronic jets, photon conversions, and heavy-flavour (HF) hadron decays. The isolation working point used in this measurement is the `PLVTight` WP. Selection criteria are applied to the longitudinal (z_0) and transverse (d_0) impact parameters (IP) which are defined in section 3.2.1. It is required that the reconstructed track associated with the electron must pass the criteria $|z_0 \cdot sin(\theta)| < 0.5$mm and $|d_0/\sigma(d_0)| <$5.0. The $\sigma(d_0)$ is the uncertainty on the transverse (d_0) IP.

Muons are reconstructed using information from tracks within the muon detector. These tracks are then matched to tracks within the inner detector and are required to have a p_T greater than 10 GeV and an $|\eta| < 2.5$. The muon identification is also an LH identification scheme. The same working points available for electrons are available for muons. Both pre-selected muons and muons used in the measurement are required to pass the `Medium` LH identification working point. The PLV algorithm is used for the muon isolation and the

`PLVTight` WP is used. The selection criteria applied to the z_0 and d_0 impact parameters are as follows: $|z_0 \cdot sin(\theta)| < 0.5$mm and $|d_0/\sigma(d_0)| < 3.0$. The criteria used to select charged leptons are summarized in table 5.3. The table first defines the criteria applied to pre-selected leptons. These include criteria based on p_T, lepton identification WP, and impact parameters. Then the criteria for leptons used in the measurement are defined which are the lepton identification WP and the isolation WP. Leptons which satisfy all of these criteria are then available to be used within the measurement.

	Pre-selected electrons	**Pre-selected muons**
Acceptance	$p_T > 10$GeV, $\|\eta^{clust}\| < 2.47$ except $1.37 < \|\eta^{clust}\| < 1.52$	$p_T > 10$GeV, $\|\eta^{clust}\| < 2.5$
Idenctification WP	looseAndBLayer	Medium
Impact parameter	$\|d_0/\sigma(d_0)\| < 5.0$ $\|z_0 \cdot sin(\theta)\| < 0.5mm$	$\|d_0/\sigma(d_0)\| < 3.0$ $\|z_0 \cdot sin(\theta)\| < 0.5mm$
	Electrons	**Muons**
Identification WP	TightLH	Medium
Isolation WP	PLVTight	PLVTight

Table 5.3: A table summarising the criteria applied to both pre-selected leptons and leptons used in the measurement is shown.

5.3.2 Jets

Jets are reconstructed from particle-flow (`PFlow`) objects [76], which combine information from the electromagnetic and hadronic calorimeters and the tracker, using the anti-k_T algorithm [77], with the R parameter is set to 0.4. Jets are accepted if they have a p_T greater than 20 GeV and an $|\eta| < 4.5$. To suppress jets originating from pileup, a multivariate algorithm called the jet-vertex-tagger (JVT) is used [78, 79]. This algorithm utilises two variables: the jet-vertex-fraction and the number of reconstructed primary vertices. The jet-vertex-fraction uses tracking information to calculate the fraction of the total momentum in the jet associated with the primary vertex. There are two WP for `PFlow` objects the `Medium` and `Tight` which correspond to efficiencies of 97% and 96% respectively. The `Medium` working point is used for this measurement and corresponds to a cut on the JVT score of greater than 0.2.

A flavour tagging algorithm is used to be able to identify jets that decay from bottom quarks. The jets are identified as b-jets using a recurrent neural network known as the `DL1r` tagger [80]. This tagger uses information about the interaction point and the tracks

to output a probability that the jet resulted from a specific flavour. This tagger differentiates between whether the jet resulted from a light quark, charm quark, bottom quark, or a tau lepton. Only information about whether the jet is tagged as a b-jet is used in this measurement. The algorithm has five available working points. To allow this measurement to be optimized information from all five working points is considered. The working point which was selected for use in this measurement is the 77% WP. Jets are only b-tagged if the absolute value of the pseudorapidity is less than 2.5. A summary of the object definitions used for jets and b-tagged jets is provided in table 5.4. The criteria used to select jets are defined. This includes the η and p_T as well information about the JVT. The criteria used to select b-tagged jets are also listed. This includes further criteria on the η and p_T. The algorithm used to tag the b-jets is also stated.

Jets	
Collection WP	AntiKt4EMPFlowjets
Acceptance	$p_T > 20$ GeV, $\|\eta\| < 4.5$
Jet-Vertex Tagger (JVT)	$JVT > 0.2$ if $\|\eta\| < 2.4$ and $p_T < 60GeV$
b-tagged jets	
Acceptance	$p_T > 20$ GeV, $\|\eta\| < 2.5$
b-tagging algorithm	`DL1r` (pseudo-continuous)

Table 5.4: A table summarising the criteria applied to jets and b-tagged jets is shown.

5.3.3 Missing transverse energy

Neutrinos are not measured directly by the detector and as such information about these particles must be inferred from the conservation of momentum. This is performed by calculating the momentum imbalance in the plane perpendicular to the beam pipe. The magnitude of this variable is called the missing transverse momentum ($E_{\mathrm{T}}^{\mathrm{miss}}$). To calculate the x and y components of this variable, equation 5.1 is used [81].

$$E_{x(y)}^{\mathrm{miss}} = E_{x(y)}^{\mathrm{miss,calo}} + E_{x(y)}^{\mathrm{miss},\mu} \tag{5.1}$$

The two terms making up the x (y) components are known as the calorimeter and muon terms. The $E_{\mathrm{T}}^{\mathrm{miss}}$ and its corresponding azimuthal component is calculated as follows:

$$E_T^{\mathrm{miss}} = \sqrt{(E_x^{\mathrm{miss}})^2 + (E_y^{\mathrm{miss}})^2}, \quad \phi^{\mathrm{miss}} = \arctan\left(\frac{E_y^{\mathrm{miss}}}{E_x^{\mathrm{miss}}}\right) \tag{5.2}$$

$$\tag{5.3}$$

All of the objects defined in this chapter are used in this calculation as well as photons and the soft term. The soft term is found from any tracks which are not from any reconstructed object. The equation that defines the $E_{\mathrm{T}}^{\mathrm{miss}}$ is given in equation 5.4.

$$E_T^{\mathrm{miss,calo}} = E_T^{\mathrm{miss,e}} + E_T^{\mathrm{miss},\gamma} + E_T^{\mathrm{miss,jets}} + E_T^{\mathrm{miss,calo}\mu} \tag{5.4}$$

The accuracy of the $E_{\mathrm{T}}^{\mathrm{miss}}$ reconstruction is sensitive to several factors. These factors include misidentification of particles, inaccuracies in momentum measurements, and cosmic rays. The main source of uncertainty with regards to $E_{\mathrm{T}}^{\mathrm{miss}}$ reconstruction is due to the uncertainties on the particles which are used for the reconstruction.

5.3.4 Overlap removal

Once the objects used in this measurement have been identified a procedure known as overlap removal (OR) is implemented to ensure that any double-counting between the objects is identified and resolved. The pre-selected leptons and jets are used in this procedure which is implemented using the following steps:

- Pre-selected electrons that overlap with pre-selected muons within a $\Delta R < 0.01$ are removed. If the electron and muon share a track the electron is also removed.
- If the ΔR between a jet and a pre-selected electron is less than 0.2, the jet is discarded.
- Any remaining electron or muon with a $\Delta R < 0.4$ to a jet is removed.
- If the distance between a jet and a pre-selected muon is $\Delta R < 0.4$ and the jet has more than two associated tracks, then the muon is removed, otherwise the jet is removed.

5.4 Event selection and calibration of simulation

For an event to be considered in this measurement it must pass a set of event selection criteria. The triggers which are used are defined in section 5.4.1 followed by the criteria used to define the signal and control regions as given in section 5.4.2. This is then followed by a discussion of the normalisations and calibrations which are applied to simulation in section 5.4.3.

5.4.1 Trigger strategy

The HLT triggers, which are defined in section 3.2.5, used in this measurement are single and dilepton triggers. These triggers are the single electron, single muon, di-electron, di-muon, and electron-muon. For an event to be considered for this measurement at least one

of the triggers must have fired. A geometric matching is also included between the selected electrons (muons) which are identified in the event. For a lepton trigger to fire, there are a set of criteria that the lepton needs to pass. The first criteria for an electron (muon) to pass is a p_T requirement such as "e24" ("mu24") which requires that an electron(muon) has a p_T of greater than 24 GeV. The next requirement is that the lepton passes a specific likelihood identification working point. The likelihood identification WP are tighter at lower p_T and become looser at higher p_T. Certain triggers will also require that a level 1 trigger must fire first before the HLT trigger can fire. For example for the electron (muon) to fire it must pass the level 1 trigger "L1EM20VH" ("L1MU15"), which required that the electron (muon) p_T is greater than 20 (15) GeV. Several electron triggers also have the "nod0" criteria which means that there are no requirements placed on the transverse impact parameter, d_0. There are triggers included in this measurement that are specific to the data acquisition period corresponding to data taken in 2015. A summary of the lepton triggers used in this measurement is presented in table 5.5. This table shows the single and dilepton triggers which are used as well as the criteria required for a trigger to fire. The triggers corresponding to data taken in 2015 are denoted by a *.

Trigger Type	Trigger requirements
Single-muon	HLT_mu20_iloose_L1MU15*
	HLT_mu26_ivarmedium, HLT_mu50
Single-electron	HLT_e24_lhmedium_L1EM20VH*
	HLT_e26_lhtight_nod0_ivarloose
	HLT_e60_lhmedium_nod0
	HLT_e120_lhloose*
	HTL_e140_lhloose_nod0
Di-muon	HLT_mu18_mu8noL1*
	HLT_mu22_mu8noL1
Di-electron	HLT_2e12_lhloose_L12EM10VH1*
	HLT_2e17_lhvloose_nod0
Electron-muon	HLT_e17_lhloose_nod0_mu14

Table 5.5: A table defining the single lepton and dilepton triggers, for both electrons and muons, that were used to select events in data and simulation is shown. Triggers labelled with * are only used for 2015 data.

5.4.2 Regions

The outline and aim of each of the regions are discussed and analyzed in the following paragraphs. There are several criteria applied across all of the regions in this measurement

which will be introduced first. Then the region-specific criteria will be provided as well as the purpose of each region. The criteria applied across all of the regions are as follows. The first criteria are that all events are required to have exactly three leptons. The next set of criteria is on the lepton p_T, where the leading lepton (ℓ_0) is required to have a $p_T \geq 30$ GeV , the next-to-leading lepton (ℓ_1) is required to have a $p_T \geq 20$ GeV and the next-to-next-to-leading lepton (ℓ_2) is required to have a $p_T \geq 15$ GeV . The lepton p_T requirement on ℓ_2 is used to remove fake leptons. This is because on average, fake leptons have a lower pT than prompt leptons. A criterion was also applied which required that the mass of the opposite sign ($m_{\ell\ell}^{OS}$) leptons in an event must have a mass greater than 10 GeV. This is included to suppress low mass resonances of J/ψ and upsilon mesons that are not included in the simulation used in this measurement.

Jets that originate from a bottom quark are tagged using the DL1r tagger as discussed in section 5.3.2. The WP used in this analysis is the 77% WP. The last criteria applied to all regions is the requirement that the sum of the lepton charges is equal to ± 1. In $t\bar{t}W^{\pm}$, there are three leptons two coming from tops and one coming from an ISW boson. Referring to the Feynman diagram 5.7 it can be noted that the top leptons are of opposite charge while the ISW lepton can be either positive or negative. When summed this can be equal to either $+1$ or -1. This requirement selects for $t\bar{t}W^{\pm}$ events while removing any backgrounds with a sum of charges $= \pm 3$. With these criteria in place, I will now introduce the two signal regions. These are the "SR high jet" and the "SR low jet". Both require exactly zero Z boson candidates and 2 or more b-jets but are split based on jet multiplicity as the names suggest. Where a Z boson candidate is defined as two opposite sign same flavour (OSSF) leptons with a combined mass($m_{\ell\ell}$) between 80 GeV 100 GeV. The SR low jet region has a jet requirement of $2 \leq N_{jets} < 4$ while the high jet region has the requirement of $4 \leq N_{jets}$. The reason for splitting this region is it increases the sensitivity to the $t\bar{t}W^{\pm}$ process. The splitting up of the signal region into an SR high jet and SR low jet regions is due to the different jet multiplicities between signal and background. Both of the $t\bar{t}W^{\pm}$ and $t\bar{t}$ processes have two jets at LO while the $t\bar{t}Z$ process has four jets at LO. This split creates the SR low jet region which has a better signal over background as compared to the combined region of both SR high and low jet regions.

The next region is called the $t\bar{t}Z$ control region (CR) and the criteria in the $t\bar{t}Z$ CR are as follows. This region requires that 2 or more jets as well as 2 or more b-tagged jets. A further criterion is applied which requires exactly one leptonic Z boson candidate. The $t\bar{t}Z$ CR is dominated by $t\bar{t}Z$ with the second most dominant process being tZ. The $t\bar{t}Z$ CR will be used to verify the modelling of the background processes. Since this region has a limited number of $t\bar{t}W^{\pm}$ events, there is minimal information regarding the A_C^{ℓ} which could cause a bias to form. To constrain the $t\bar{t}$ process two regions with similar selections to the SR high

jet and SR low jet regions were created. The only difference between the SR and $t\bar{t}$ regions being the number of b-tagged jets where the $t\bar{t}$ regions require exactly 1 b-tagged jet. These $t\bar{t}$ regions are named $t\bar{t}$ high jet and $t\bar{t}$ low jet. Both require exactly zero Z boson candidates and are again split according to jet multiplicity to mirror the SR low and high jet regions. The regions are split as follows: tt low jet has a jet requirement of $2 \leq \mathrm{N}_{jets} < 4$ while the tt high jet region has the requirement of $4 \leq \mathrm{N}_{jets}$. It should also be noted that the $t\bar{t}$ regions have a comparable amount of $t\bar{t}W^{\pm}$ to the two SR regions but with an increased amount of background processes. The background processes which account for most of this increase are $t\bar{t}$ and VV. The comparitive increase of $t\bar{t}$ as compared to $t\bar{t}W^{\pm}$ in the $t\bar{t}$ regions is due to the fact that the third lepton in $t\bar{t}$ is generally a heavy flavour (HF) fake lepton. The OR between leptons and jets is likely to discard the second b-jet in a $t\bar{t}$ event as a result of the third lepton which results in a greater increase of $t\bar{t}$ events in regions with a requirement of exactly one b-jet as compared to $t\bar{t}W^{\pm}$.

A summary of all the selections used in the different regions is presented in table 5.6. This table breaks down the criteria into criteria that are applied across all regions and then criteria that are specific to each region. These are criteria on the lepton p_T, jet and b-jet multiplicities, b-tagging WP, number of Z boson candidates, and the sum of the lepton charges. Future research on this topic could improve the criteria used for the event selection through the reduction of the number of background events that enter the measurement. Such a reduction in background events would improve the sensitivity of this measurement to the $t\bar{t}W^{\pm}$ process and in turn improve the uncertainties extracted.

5.4.3 Normalisation and calibration of simulation

To ensure that the expectation for signal and backgrounds processes derived from the simulation are correctly normalised and calibrated several corrections are applied to the simulation. These corrections are in the form of per-event weights which adjust the contribution of a given event to the binned histograms from which the final results of the measurement are extracted. These weights ensure that the simulation is scaled correctly and the shape of the distribution is accurate.

Several calibrations are applied to the simulation. These correspond to the luminosity, the cross section, and any k-factor needed to adjust the cross section to match that of a higher-order are applied [82]. Calibrations that account for discrepancies between data and simulation in the pileup, lepton triggering, reconstruction and identification of leptons and jets, as well as b-tagging efficiencies are also applied.

General Criteria	
Lepton p_T selection	$\ell_0 \geq 30$ GeV, $\ell_1 \geq 20$ GeV , $\ell_2 \geq 15$ GeV
B-tag WP	DL1r = 77%
$\sum charge$	$= \pm 1$
$m_{\ell\ell}^{OS}$	$m_{\ell\ell}^{OS} \geq 10$ GeV

$N_b \geq 2$ b-jets

	SR lowJets	SR highJets	$t\bar{t}Z$ CR
No. Jets	$2 \leq N_{jets} < 4$	$4 \leq N_{jets}$	$2 \leq N_{jets}$
No. Z candidates	$= 0$	$= 0$	$= 1$

$N_b = 1$ b-jets

	tt lowJets	tt highJets
No. Jets	$2 \leq N_{jets} < 4$	$4 \leq N_{jets}$
No. Z candidates	$= 0$	$= 0$

Table 5.6: A table summarising the event selection criteria applied to the signal and control regions is shown.

5.5 Fake lepton contribution

This section outlines the methods used to estimate fake leptons.

For this dissertation a fake lepton is defined as a combination of non-prompt and mis-identified leptons where a mis-identified lepton is a $\Pi^{\pm}$ meson which is identified as either an electron or muon. Non-prompt leptons are the dominant source of fake leptons with the mis-identified leptons providing a small contribution. Fake electrons and muons can originate from several different sources such as meson decays and electrons from photon conversions. However, the most prominent origin of non-prompt leptons for this measurement results from heavy-flavour hadron decays. To classify fake leptons a tool known as the `IFFTruthClassifier` was used. This tool categorises electrons and muons based on their type and origin. The processes which are included in this measurement to estimate fakes are the $t\bar{t}$ and the Z + jets processes. Both of these processes produce two leptons with the third lepton being a fake.

5.6 Comparing data to simulation in the control region

This section will provide a comparison between data and simulation using the $t\bar{t}Z$ CR as defined in table 5.6. The comparison is performed to ensure that the simulation models the data well and to check that all the required samples are included, normalised, and calibrated

correctly. The comparison will also allow the modelling of the objects defined in section 5.3 to be checked which will be performed using binned histograms of selected observables. The measurement presented in this dissertation forms part of a larger ATLAS analysis and as a result the measurement has remained blinded. Hence, the reason for using the $t\bar{t}Z$ CR is due to the limited number of $t\bar{t}W^{\pm}$ events in this region which minimises the potential, for biases to form.

If the modelling of the data was inaccurate it would present itself as a discrepancy between the data and the simulation. For example, if a major background - such as $t\bar{t}$ - were not included the simulation would predict substantially fewer events than measured in data. Similarly, if the normalisations and calibrations were applied incorrectly it could result in the simulation predicting more or fewer events than data. The calibrations also affect the shapes of the distributions which could cause a difference between the shape of the data distribution when compared to the shape of the simulation distribution. A qualitative way of investigating the agreement between simulation and data is as follows. Good agreement is defined by the simulation differing from the data within one standard deviation (1 σ). If the simulation and data differ by less than two standard deviations the agreement is still acceptable. If it is greater than 2 σ and the agreement will be categorized as being bad which would warrant further investigation. Table 5.7 shows the pre-fit yields for each of the simulation processes in each region where the data is only shown for the $t\bar{t}Z$ CR. The uncertainties shown are a combination of statistical and some systematic uncertainties. The systematic uncertainties considered are normalizations of some of the samples and instrumental uncertainties. The sample normalizations included are on $t\bar{t}W^{\pm}$, $t\bar{t}Z$, $t\bar{t}$, tZ, and $t\bar{t}H$. The instrumental uncertainties that are included correspond to the luminosity, trigger efficiencies, JVT, pile-up, and b-tagging. The uncertainties outlined for table 5.7 will apply for the rest of the uncertainties presented in this section. The data shown for the $t\bar{t}Z$ CR in table 5.7 differs by more than 1 σ from the number of events predicted by simulation but does agree within 2 σ. The following paragraphs will present the investigation of the agreement in the jets, b-tagged jets, leptons, and missing transverse momentum.

Figure 5.2 presents information regarding the jets and b-tagged jets. These figures show the simulation plotted against the data within the $t\bar{t}Z$ control region. The uncertainties for the simulation are shown by the band of diagonal blue lines and the uncertainties for data are shown as black vertical lines. The y-axis of all three plots shows the number of events. Figure 5.2a shows the jet multiplicity, figure 5.2b shows the number of b-tagged jets, and figure 5.2c shows the sum of the transverse momentum for all the jets in the system known as H_T. All of the figures shown in this section are the pre-fit plots. In the three jet distributions in figure 5.2, the agreement is acceptable and generally within 1 σ. A few outliers can be seen the first of which is in figure 5.2a. The bins corresponding to

	SR lowJet	SR highJet	$t\bar{t}$Z CR	$t\bar{t}$ lowJet	$t\bar{t}$ highJet
$t\bar{t}Z$	13.5 ± 1.5	38.8 ± 4.1	169 ± 17	16.3 ± 1.7	28.6 ± 3.0
$t\bar{t}$	28 ± 15	16.8 ± 8.6	4.9 ± 2.6	78 ± 39	21 ± 11
$t\bar{t}H$	7.8 ± 1.2	21.4 ± 3.3	5.87 ± 0.91	9.0 ± 1.4	15.6 ± 2.4
tZ	1.86 ± 0.28	2.08 ± 0.32	25.7 ± 3.7	6.31 ± 0.92	2.11 ± 0.33
VV	4.31 ± 0.25	3.3 ± 0.16	32.9 ± 1.1	38.9 ± 1.6	16.43 ± 0.63
Z + Jets	0.78 ± 0.99	0.77 ± 0.32	3.7 ± 1.4	5.4 ± 3.0	1.42 ± 0.51
Other	1.49 ± 0.08	8.69 ± 0.31	15.99 ± 0.91	5.27 ± 0.21	5.68 ± 0.23
$t\bar{t}W^{\pm}$	29.9 ± 1.0	15.05 ± 0.54	6.0 ± 0.3	28.0 ± 1.0	11.39 ± 0.42
Total	88 ± 15	106 ± 10	264 ± 19	187 ± 39	103 ± 12
Data	-	-	319 ± 17	-	-

Table 5.7: A table of the pre-fit yields for each of the simulation processes in each region is shown. The data remains blinded in all regions except the $t\bar{t}Z$ CR

a jet multiplicity of two and three jets do not agree within 1 σ, however, they do agree within 2 σ. A similar statement can be made for figure 5.2c with regards to the fourth bin from the left. The agreement is generally within 1 σ with one bin differing by less 2 σ. Figure 5.2 provides strong evidence that there is an adequate agreement in the modelling of jets.

There are three leptons used in this measurement and the p_T, η, and ϕ for each one will be shown. It is important to note that the leptons are ordered according to their p_T in descending order. So the leading lepton is the lepton with the highest p_T in the event followed by the sub-leading and third lepton, respectively. Figures 5.3, 5.4 and 5.5 show the data versus simulation in the $t\bar{t}Z$ CR for the leading and sub-leading and third leptons - respectively. Figure 5.4 shows the data versus simulation in the $t\bar{t}Z$ CR for the third lepton. The y-axis corresponds to the number of events. The uncertainties are as defined for figure 5.2. The agreement in the set of figures 5.3, 5.4 and 5.5 is adequate as the agreement is generally within 1 σ. There are several instances where the agreement is not within 1 σ, the first example of which can be seen in figure 5.3a. In figure 5.3a, it can be seen that the fifth bin from the left does not agree within 1 σ, however, they do agree within 2 σ. There are several further instances where the data and simulation do not agree within 1 σ but do agree within 2 σ indicating acceptable agreement.

Figure 5.6 shows a histogram of the $E_{\mathrm{T}}^{\mathrm{miss}}$ where the y-axis and uncertainties are as have been outlined for the previous set of figures. The agreement in this histogram is good with all bins in the simulation distribution being within one standard deviation of the data. As has been shown the agreement between data and simulation within the jets, b-jets, leptons and $E_{\mathrm{T}}^{\mathrm{miss}}$ are all within acceptable limits in the $t\bar{t}Z$ CR. This provides a good indication that the simulation models the data accurately for each of these objects and that all of the normalisations and calibrations are applied correctly. It is worth noting that on av-

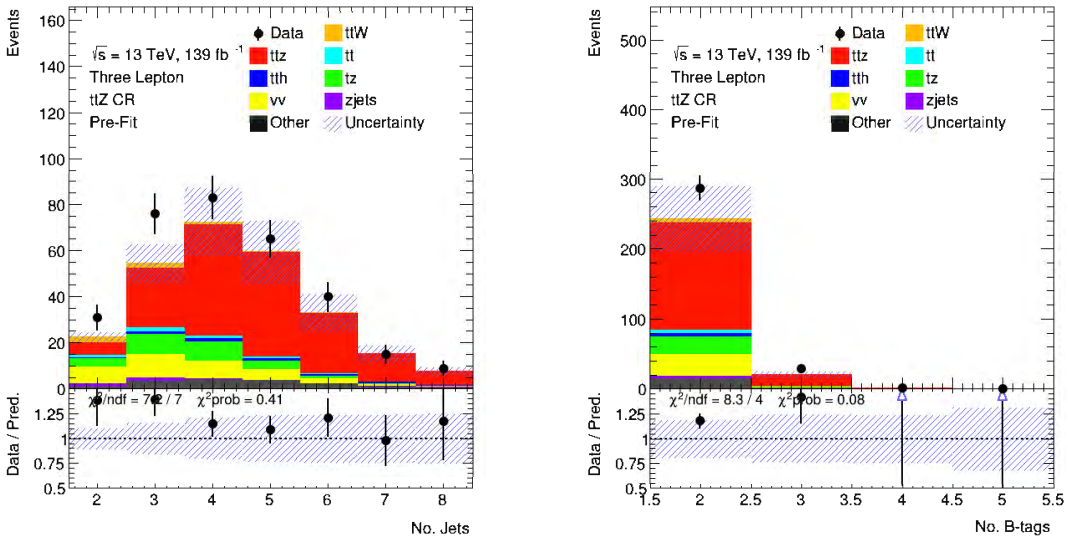

(a) No. of Jets

(b) No. of B-tagged Jets

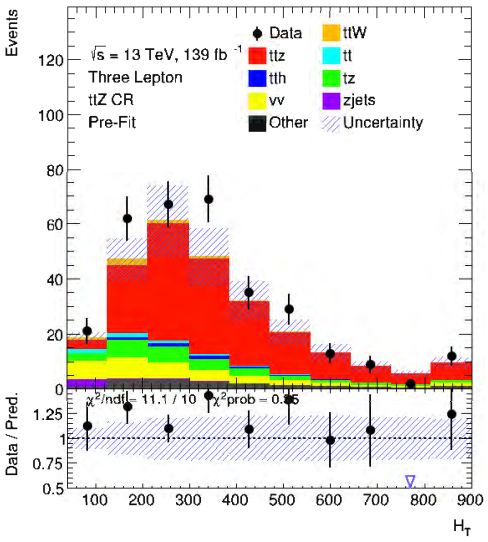

(c) H_T

Figure 5.2: A set of pre-fit histograms that compare data against simulation in the $t\bar{t}Z$ CR are shown. The (a) jet multiplicity, (b) the number of b-tagged jets, and (c) the sum of the transverse momentum for all the jets in the system known as H_T are shown.

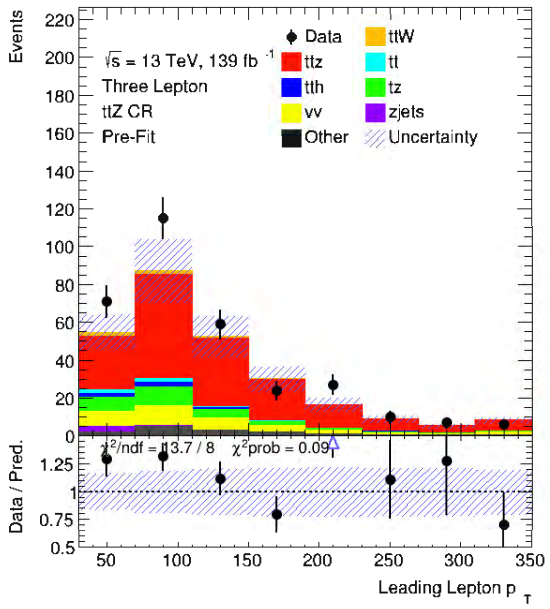

(a) Leading lepton p_T

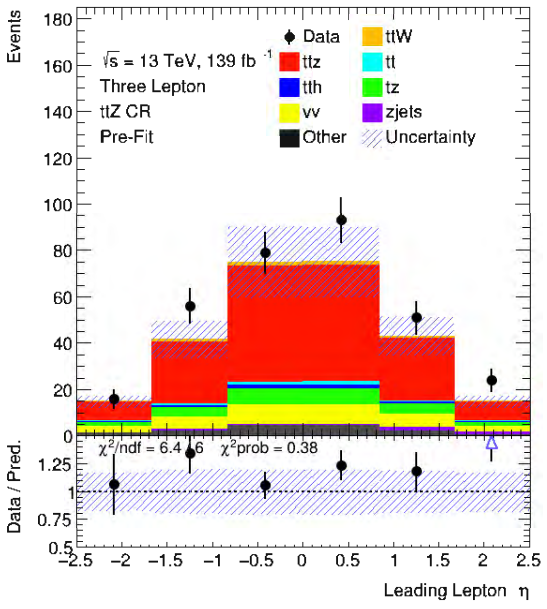

(b) Leading lepton η

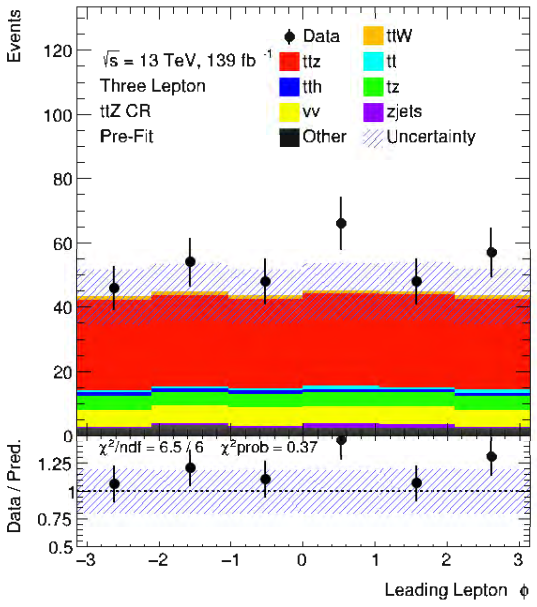

(c) Leading lepton ϕ

Figure 5.3: A set of pre-fit histograms comparing data against simulation in the $t\bar{t}Z$ CR for the leading lepton are shown for the variables p_T, η, and ϕ.

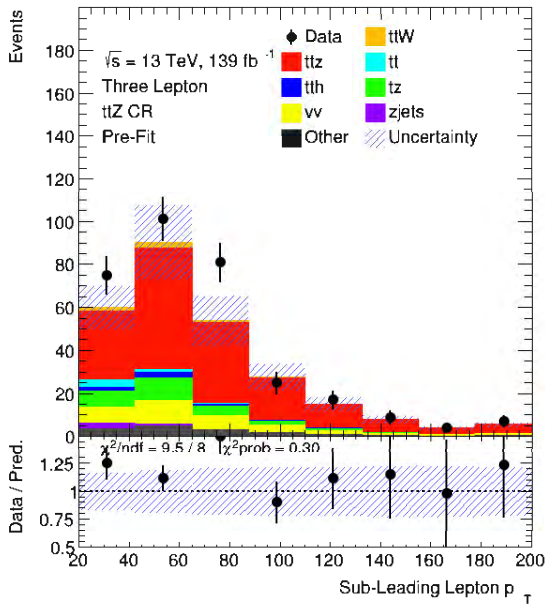

(a) Sub-leading lepton p_T

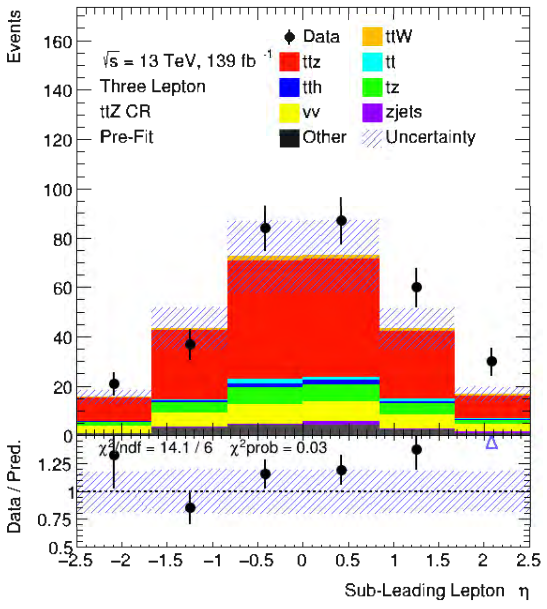

(b) Sub-leading lepton η

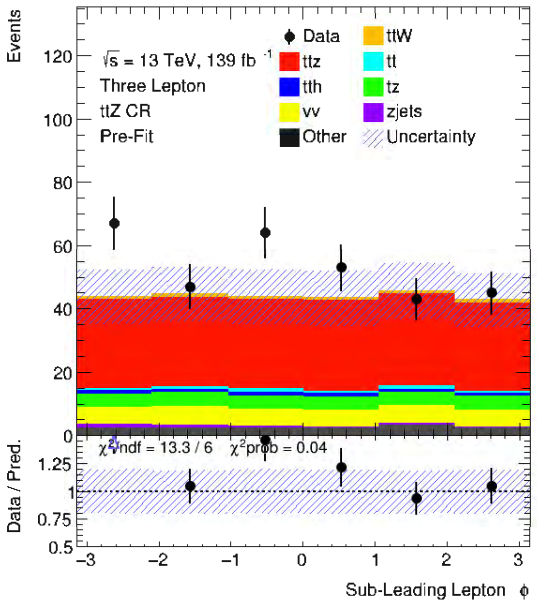

(c) Sub-leading lepton ϕ

Figure 5.4: A set of pre-fit histograms comparing data against simulation in the $t\bar{t}Z$ CR for the sub-leading lepton are shown for the variables p_T, η, and ϕ.

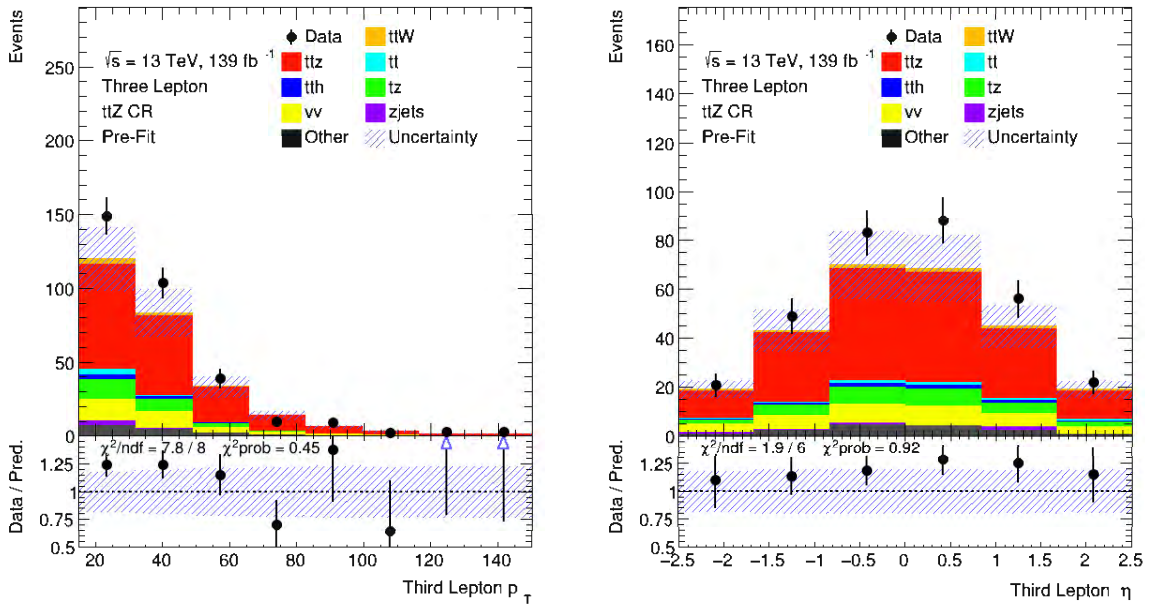

(a) Third lepton p_T

(b) Third lepton η

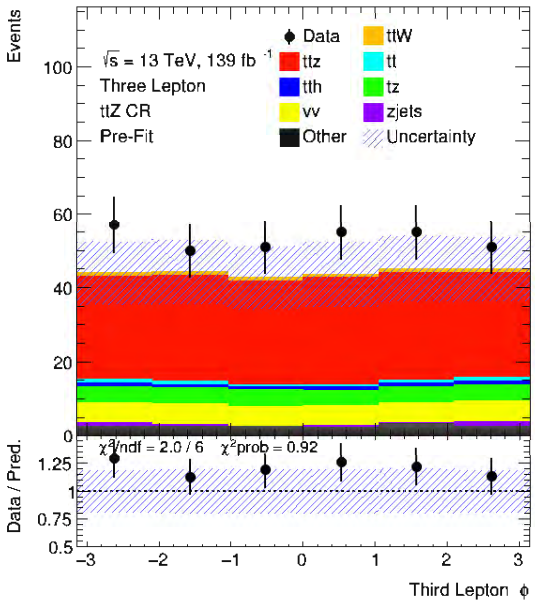

(c) Third lepton ϕ

Figure 5.5: A set of pre-fit histograms comparing data against simulation in the $t\bar{t}Z$ CR for the third lepton are shown for the variables p_T, η, and ϕ.

erage, the simulation underestimates the number of events when compared to data. The underestimation is most likely due to the estimation of fake lepton from simulation being underestimated, however this can be corrected for in the fit.

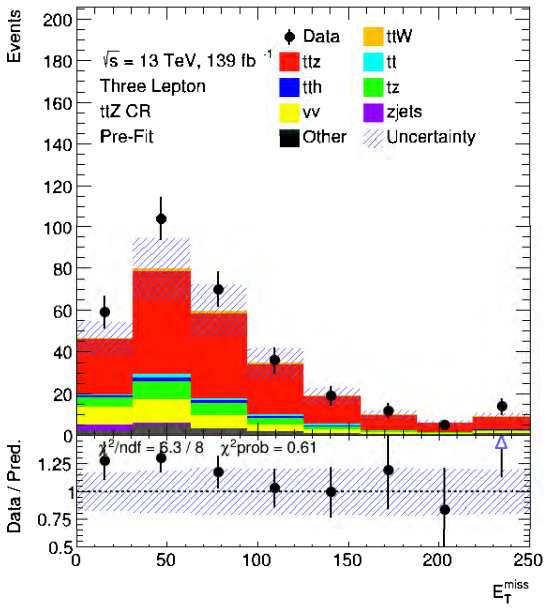

Figure 5.6: A pre-fit histogram of the comparison between simulation and data in the $t\bar{t}Z$ CR using the missing transverse momenta ($E_{\mathrm{T}}^{\mathrm{miss}}$) is shown.

5.7 Lepton-top association

The following section will describe the lepton identification process. A brief description of the motivation for the lepton-top association will be provided and will build on the information presented in section 4.3. This will be followed by the introduction to the notation which will be used throughout the rest of this chapter and is presented in section 5.7.1. Then the method used to associate leptons to the particles from which they decayed is described in section 5.7.2. Finally, the algorithms used to identify leptons that decay from top quarks is presented in sections 5.7.3 and 5.7.4. The calculation of the A_C^ℓ requires the pseudorapidity of the leptons that decay from top quarks. To calculate the A_C^ℓ the two leptons that decay from top quarks need to be identified which are then used to calculate the Δ_η^ℓ variable as shown in equation 5.5.

$$\Delta_\eta^\ell = |\eta_t| - |\eta_{\bar{t}}| \tag{5.5}$$

In a $t\bar{t}W^\pm$ event, the two leptons decaying from top quarks need to be identified over the

lepton coming from the ISW lepton. Figure 5.7 shows the Feynmann diagram for $t\bar{t}W^{\pm}$ once all of the particles have decayed to their final states. Using figure 5.7, it can be seen that the leptons coming from the top quark and top anti-quark are of opposite charge. The lepton decaying from the ISW can be either positive or negative in charge. These two points imply that the lepton charges for $t\bar{t}W^{\pm}$ will be either (+ - -) or (+ - +). In either case, there will be two same-sign leptons and one opposite sign lepton where the opposite sign lepton will have originated from a top quark.

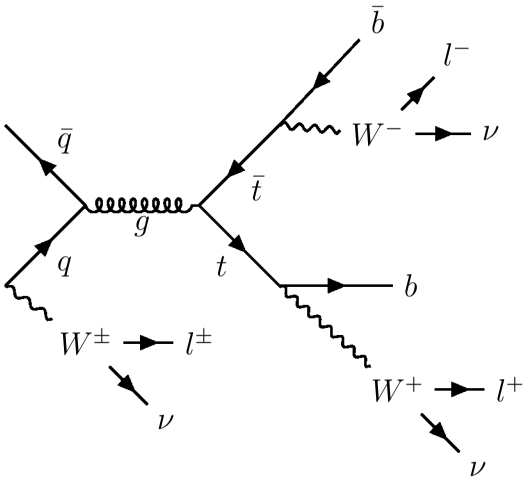

Figure 5.7: A Feynman diagram of the trilepton final state of the $t\bar{t}W^{\pm}$.

The following naming convention will be used going forward. The opposite sign lepton will be named the odd lepton while the two same-sign leptons will be referred to as even leptons. Lepton-top association is used to associate the final state leptons to the particles from which they decayed and are referred to as the mother. So in the case of $W^+ \rightarrow \ell^+\nu$ the W^+ boson is the mother of the ℓ^+ lepton. Table 5.8 shows the mother particles as well as the leptons that decay from for each mother particle in the $t\bar{t}W^+$ process. This table shows that the positively charged leptons come from the initial-state W boson and the top quark. The remaining negatively charged lepton decayed from the top anti-quark.

Mother	Lepton	Lepton Charge
t	ℓ^+	+1
$\bar{t}$	ℓ^-	-1
W^+	ℓ^+	+1

Table 5.8: A table of the mother objects in $t\bar{t}W^+$ and the corresponding leptons - as well as the charge of each lepton - are shown.

In terms of odd and even leptons in $t\bar{t}W^+$, the odd lepton will have originated from a top

anti-quark and have a negative charge. The even leptons will originate from the top quark and the ISW$^+$ boson which will both have positive charges. A similar argument will hold in the case of $t\bar{t}W^-$. Since the odd lepton can be identified based on charge this leaves the two even leptons that need to be identified as either decaying from a top quark or an ISW boson. Physics specific to top quark decay products will be used to differentiate between the even leptons.

5.7.1 Notation

The notation used in the following sections will be defined to keep everything concise while still clearly conveying the ideas and methodology used. In the lepton-top association, the important variables are the ΔR between the objects and the mass of the lepton b-jet system ($m_{\ell b}$) where the ΔR is defined in equation 3.4. These variables are calculated on a lepton-by-lepton basis. So the ΔR is calculated between the lepton and the b-jets in the system. Then the mass of the lepton b-jet system is calculated where the b-jets are ordered in ascending order of ΔR. This means that the closest b-jet will be b-jet zero (b_0) while the next closest will be b-jet one (b_1). So $\Delta R\ (\ell - b_0)$ is the ΔR between the lepton and its closest b-jet while $m_{\ell b_0}$ is the mass of the lepton and its closest b-jet.

5.7.2 Truth matching

In the process of identifying leptons, it is necessary to know which leptons in simulation decayed from top quarks and which decayed from ISW's. This is important for training algorithms as well as estimating the efficiency of the algorithms. Efficiency is defined as the probability that an object will be correctly identified. The simulation samples used in this measurement contain information concerning the objects at different stages of the simulation process. The two sets of information pertinent to this discussion correspond to the particles before they are passed through the detector simulation and after. The set of information corresponding to before being passed through the detector simulation is known as the truth information. This is because it corresponds to the particles without any uncertainties as a result of being measured and contains knowledge of what each of the particles in the final state decayed from. Once the particles pass through the detector simulation they are known as the reconstructed objects. This set does not contain information regarding what the objects decayed from. As a result, this section outlines the methodology used to associate objects between the two sets of information which would allow objects in the final state to be associated with the particles they decayed from.

Since the precision of the detector is finite, the measurement of these objects comes with some uncertainty and as such the true momenta and the reconstructed momenta can differ. The goal is to be able to match reconstructed leptons to true leptons which will

be implemented using the ΔR between the truth and reconstructed leptons. The ATLAS detector measures the tracks of electrons and muons precisely which means that the η and ϕ of the reconstructed leptons should be a close match to those in the truth information. The ΔR between the reconstructed and truth leptons is required to be Δ R < 0.3. Then each reconstructed lepton will be matched to the closest truth lepton in terms of ΔR. Figure 5.8 demonstrates this process. The figure shows a reconstructed lepton (r_1) and two truth leptons (t_1, t_2). A two dimensional representation of ΔR between the reconstructed and truth leptons are also shown. Since ΔR_1 is smaller than ΔR_2 the reconstructed lepton will be matched to t_1 assuming the $\Delta R < 0.3$. Using the truth matching process as outlined reconstructed leptons can now be matched the particle from which they decayed.

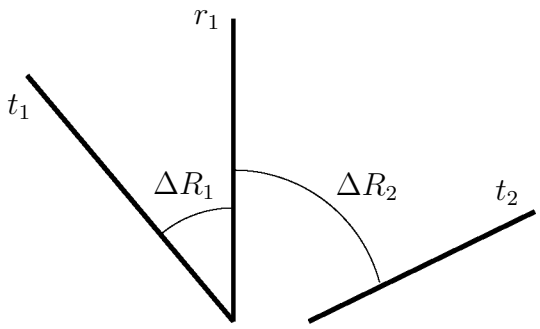

Figure 5.8: A figure demonstrating the truth matching between the reconstructed object (r_1) and the two truth objects (t_1, t_2) is shown

5.7.3 The $m_{\ell b}$ algorithm

The first method introduced to identify leptons that decay from top quarks, uses a single discriminating variable to differentiate between the two even leptons. When searching for discriminating variables, it is vital to keep the physics of the system in mind. Since the top quark almost always decays to a W boson and a bottom quark this implies that there should be a correlation between the W boson and the b quark that decay from the same top. One of the observables which will capture the correlation of the top quark system is the combined invariant mass of the b-jet and the lepton ($m_{\ell b}$) from the top quark, which should return the top quark mass bar the energy and momentum carried away by the neutrino. A second observable is the angular distance (ΔR) between the lepton and the b-jet which is dependent on the momentum of the top quark. These correlations discussed are not present for the lepton decaying from the ISW boson. However, the ISW lepton will be randomly oriented relative to the b-jets coming from the top quarks which implies that cases will arise where the ISW lepton is oriented such that it will have properties that are top-like. This means that the ΔR between the ISW and the b-jet as well as the mass of the combined objects will appear to be top-like. Several variables were tested on their ability to discriminate between

leptons decaying from top and ISW bosons. Of these variables the one with the strongest discrimination between signal and background leptons was the $m_{\ell b}$ of the lepton with the closest b-jet in terms of ΔR ($m_{\ell b_0}$). Figure 5.9 shows the normalised distribution of the $m_{\ell b_0}$ for leptons decaying from top quarks (red) versus the leptons coming from ISW's (blue) in the nominal MADGRAPH $t\bar{t}W^{\pm}$ sample. The y-axis is in arbitrary units as these histograms have been normalised. The reason for normalising is because it highlights differences in shapes between the distributions which are important for discrimination. The $m_{\ell b_0}$ for the leptons decaying from ISW's have a much longer tail as compared to the leptons from top quarks.

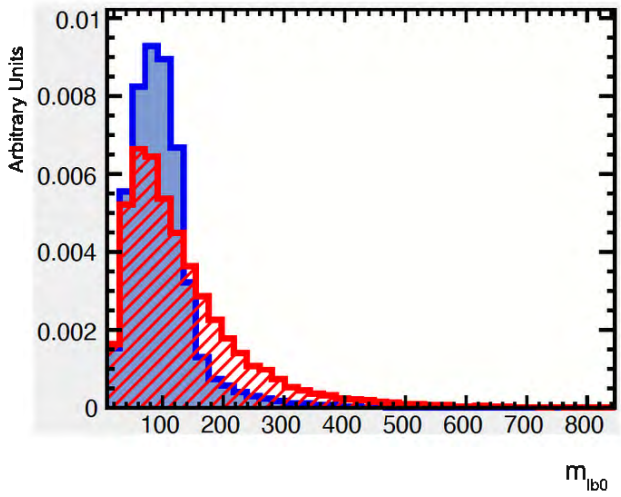

Figure 5.9: The normalised distributions comparing the leptons coming from top quarks (red) against the leptons coming from ISW's (blue) in $t\bar{t}W^{\pm}$ for several the combined invariant mass of the lepton and its closest b-jet ($m_{\ell b_0}$) [GeV] are shown.

To ensure that the $m_{\ell b_0}$ variable is well modelled by the simulation a comparison is done between data and simulation in the $t\bar{t}Z$ CR in figure 5.10. The uncertainties shown are as described in section 5.6. The y-axis shows the number of events while the x-axis shows the $m_{\ell b_0}$. This is done for the leading, sub-leading and third leptons. Of the three figures, all of the bins agree within 1σ bar one bin in figure 5.10a which is the second bin from the right and does agree within 2σ. As a result, it can be seen that the modelling of the $m_{\ell b_0}$ variable is adequate. The next step is to create a variable that is capable of discriminating between leptons that decay from top quarks versus ISW's - using the $m_{\ell b_0}$. The peak of the $m_{\ell b}$ distribution for leptons decaying from top quarks was found to be at 92 GeV which was then used to create the discriminating variable shown in equation 5.6. The D_{Peak} is calculated for both even leptons.

$$D_{Peak} = |m_{\ell b} - 92| \tag{5.6}$$

The lepton decaying from a top quark is selected based on which even lepton has the min(D_{Peak}) in the event. This method correctly identifies leptons decaying from top quarks approximately 68% of the time. This method provides a good starting point for being able to select leptons decaying from top quarks. Since this method only utilises a single observable it can be hypothesised that a multivariate analysis which utilises more information about the event will improve the lepton-top association.

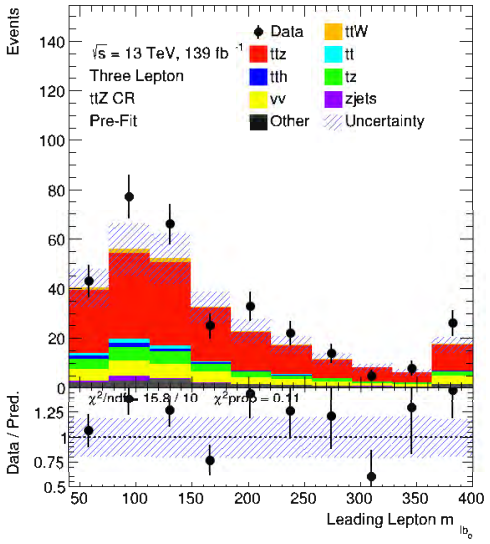

(a) Leading lepton $m_{\ell b_0}$

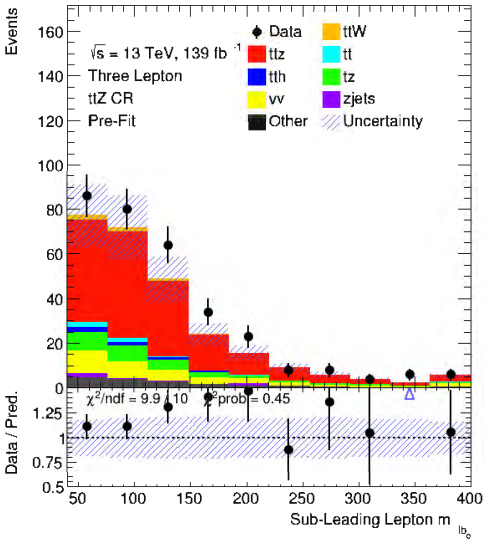

(b) Sub-leading lepton $m_{\ell b_0}$

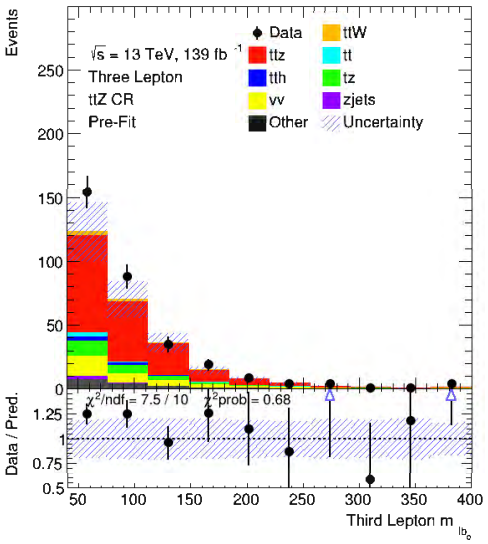

(c) Third lepton $m_{\ell b_0}$

Figure 5.10: A set of pre-fit histograms of the $m_{\ell b_0}$ for the leading, sub-leading and third leptons in the $t\bar{t}Z$ control region are shown.

5.7.4 Machine learning

This section describes the use of machine learning (ML) to improve the lepton-top association as compared to the $m_{\ell b}$ algorithm. These ML methods use information from several variables to differentiate between the even leptons. The ML algorithms were implemented using TMVA [83] which is a machine learning environment used for multivariate classification. Several different ML algorithms were investigated for the lepton-top association and are as follows [84]:

- Boosted Decision Tree (BDT)
- Gradient Tree Boosting (GTB)
- A Keras [85] Neural Network

Training

Training the lepton-top association requires the use of a portion of the simulation. If only one $t\bar{t}W^{\pm}$ sample were used for both the ML training and measurement this would cause a reduction of the number of $t\bar{t}W^{\pm}$ events available for the measurement. Since one of the dominant sources of uncertainty in this measurement is the number of $t\bar{t}W^{\pm}$ events a further reduction of these events would only serve to increase the uncertainties of the measurement. To maintain the number of $t\bar{t}W^{\pm}$ events a second $t\bar{t}W^{\pm}$ sample was included as discussed in section 5.1. This second sample was simulated using `SHERPA` 2.2.8 and will be used to train the ML algorithms. The `SHERPA` sample is independently simulated from the main `MADGRAPH` $t\bar{t}W^{\pm}$ sample but has several differences to the `MADGRAPH` sample which need to be accounted for. The main distinction between these two samples comes in the modelling of the jets within these systems. The number of jets simulated by `SHERPA` will have, on average, a higher multiplicity when compared to the `MADGRAPH` sample. To avoid sub-optimal training of the ML algorithms, the variables used in this association do not depend on the jet multiplicity. The variables used for the training are the $m_{\ell b_0}$, $m_{\ell b_1}$, $\Delta\mathrm{R}(\ell - b_0)$, $\Delta\mathrm{R}(\ell - b_1)$ and the lepton p_T. These variables have a minimal correlation with the jet multiplicity. Figure 5.11 shows the normalised distribution of the leptons decaying from top quarks (red) versus the leptons coming from ISW's (blue) in $t\bar{t}W^{\pm}$ for several discriminating variables. The y-axis is in arbitrary units as these histograms have been normalised. The $m_{\ell b_0}$ variable is shown in the previous section in figure 5.10. The discrimination of the variables shown in figure 5.11 is not as strong as that shown in figure 5.10 but each variable provides additional information.

To ensure that these variables are modelled well a comparison is done between data and simulation in the $t\bar{t}Z$ CR. The modelling for the $m_{\ell b_0}$ as well as the lepton p_T have both been checked in figures 5.10 and 5.3 respectively. The remaining variables are the

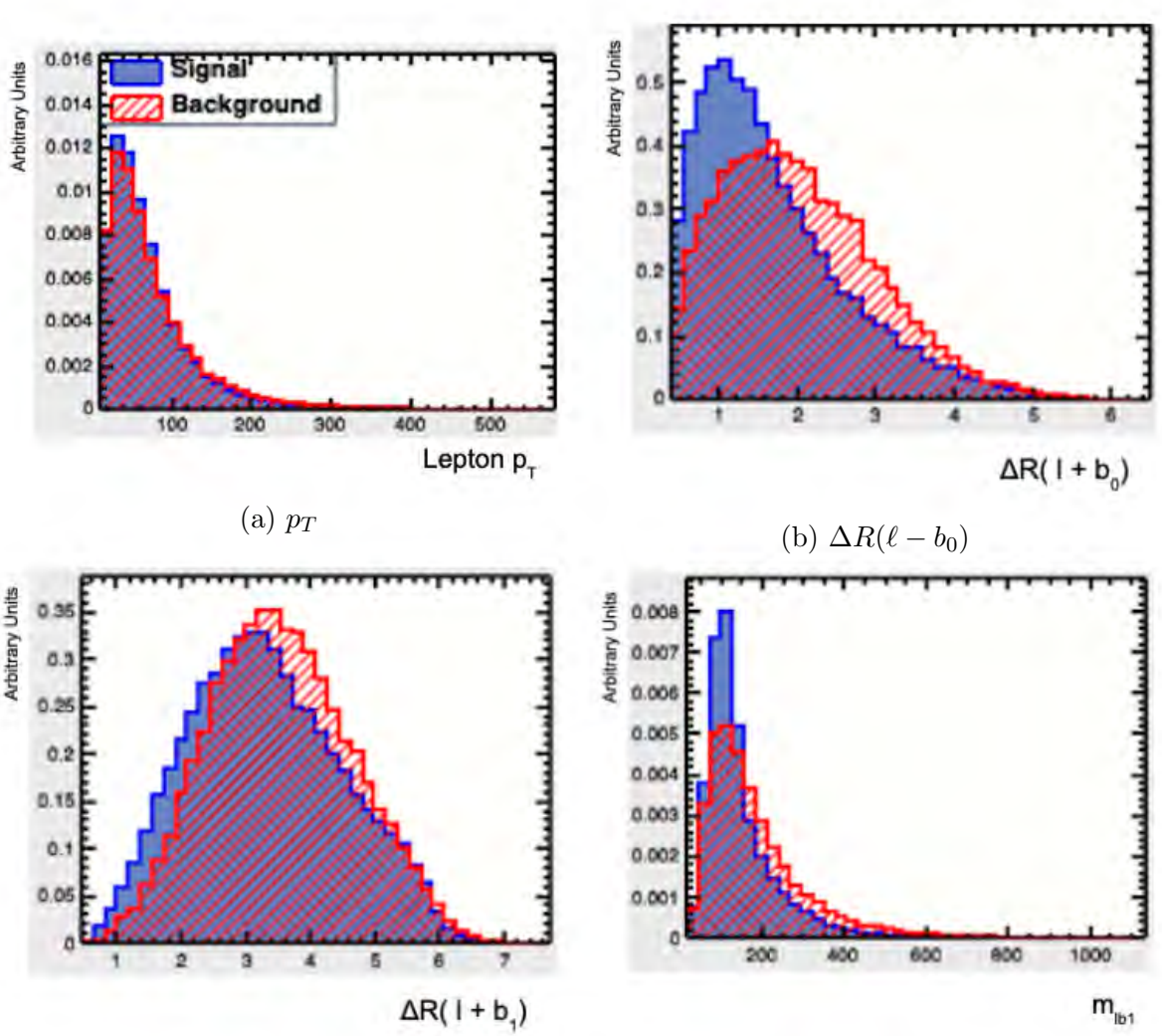

(a) p_T

(b) $\Delta R(\ell - b_0)$

(c) $\Delta R(\ell - b_1)$

(d) $m_{\ell b_1}$

Figure 5.11: The normalised distributions comparing the leptons coming from top quarks (red) against the leptons coming from ISW's (blue) in $t\bar{t}W^{\pm}$ for several observables are shown.

$m_{\ell b_1}$, $\Delta R(\ell - b_0)$ and $\Delta R(\ell - b_1)$ which are shown for the leading, sub-leading and third leptons in figures 5.13 and 5.14. The uncertainties shown are as described in section 5.6. The y-axis shows the number of events. Most of the bins shown agree within 1σ with all of the bins agreeing within 2σ. This indicates that the variables are adequately modelled by the simulation and can be used for the lepton-top association. Using the truth matching outlined in section 5.7.2 all of the leptons in $t\bar{t}W^{\pm}$ are matched to their mother particle. If a $t\bar{t}W^{\pm}$ event contains leptons that were not truth matched or did not pass the event selection defined in table 5.6 then the event is not used in training. The SHERPA $t\bar{t}W^{\pm}$ sample is then processed and split into signal and background classes which are then used to train the ML algorithms. The output of the training for each of the ML algorithms is as follows:

- Variable importance
- A receiver operating curve (ROC)
- The area under the curve (AUC)

Each of these training outputs is used to assess the algorithm's ability at associating leptons and top quarks. The variable importance is a metric used to identify which of the variables used by the ML algorithm provides the best discrimination between the signal and background. The ROC curve and more importantly the AUC is used to check the efficiency of selecting leptons decaying from top quarks. The AUC is the integral of the receiver operating curve which varies between zero and one. The closer the AUC is to one the better the algorithm is at distinguishing between the signal and background classes. Table 5.9 shows the integral of the receiver operating curve (AUC) for the different ML algorithms studied for the lepton-top association where it can be seen that the GTB provides the best AUC.

Method	AUC
GTB	0.721
BDT	0.718
PyKeras	0.714

Table 5.9: The integral of the receiver operating curve (AUC) for the different ML algorithms studied for the lepton-top association is shown.

In figure 5.15 the receiver operating curves (ROC) can be seen for the three ML algorithms. The y-axis shows the background rejection and the x-axis shows the signal efficiency. The three methods Keras neural network, GTB, and BDT are shown in blue, red, and green, respectively. Figure 5.15 highlights the fact that, although the GTB is the best performing

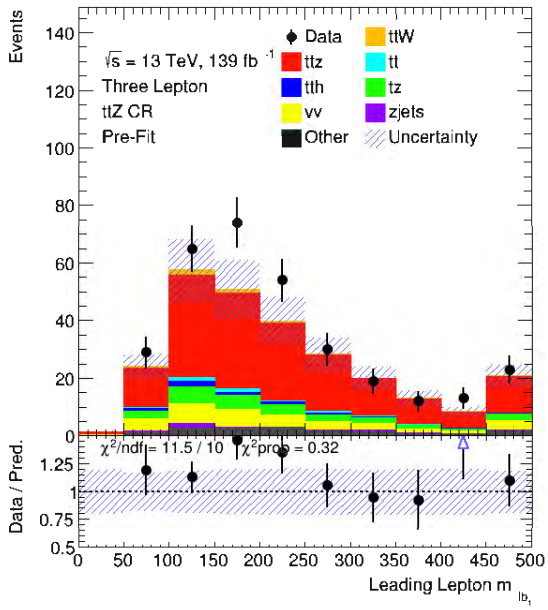

(a) Leading lepton $m_{\ell b_1}$

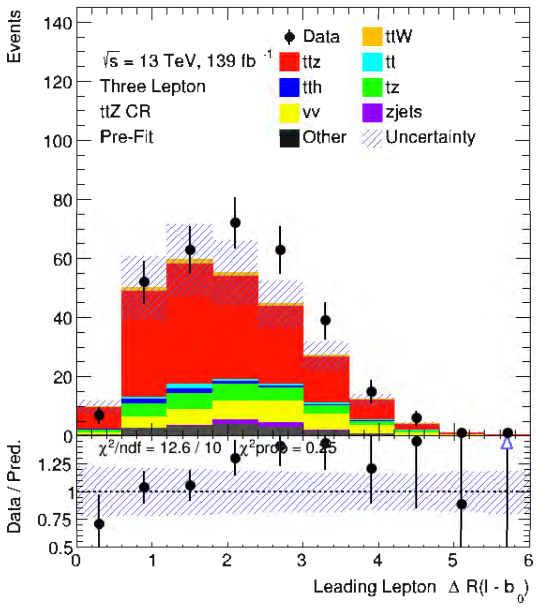

(b) Leading lepton $\Delta\mathrm{R}(\ell - b_0)$

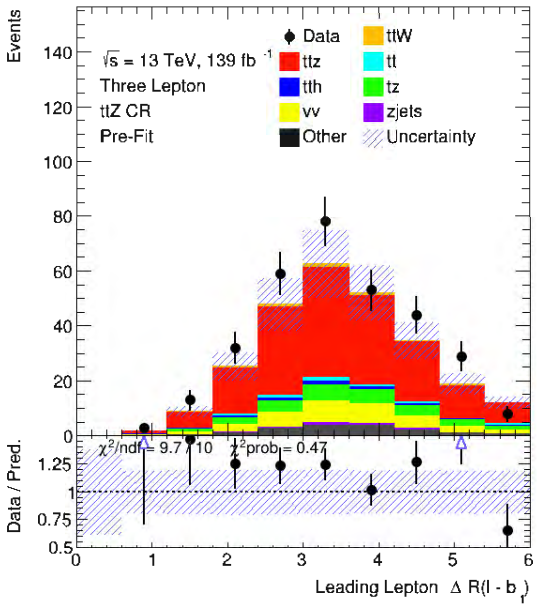

(c) Leading lepton $\Delta\mathrm{R}(\ell - b_1)$

Figure 5.12: A set of pre-fit histograms comparing data against simulation in the $t\bar{t}Z$ CR of the leading lepton for the variables $m_{\ell b_1}$, $\Delta\mathrm{R}(\ell - b_0)$ and $\Delta\mathrm{R}(\ell - b_1)$.

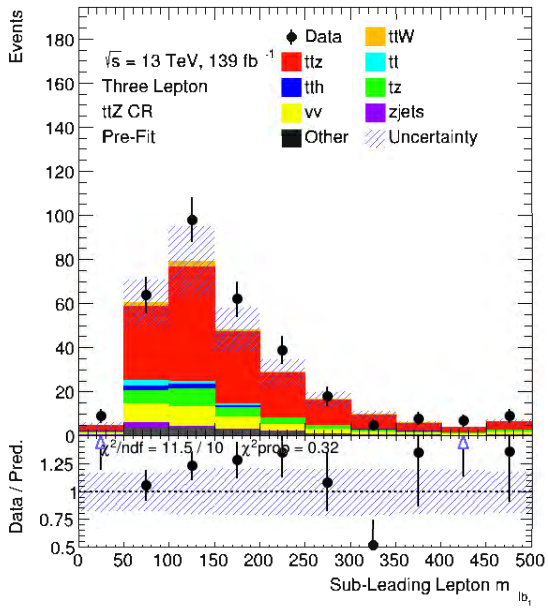

(a) Sub-leading lepton $m_{\ell b_1}$

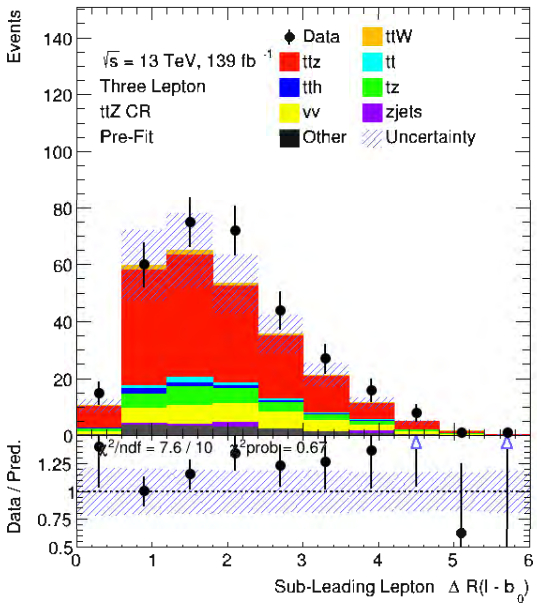

(b) Sub-leading lepton $\Delta\mathrm{R}(\ell - b_0)$

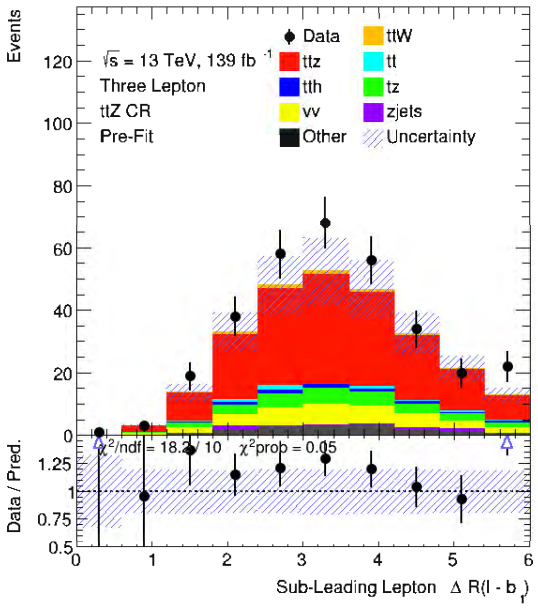

(c) Sub-leading lepton $\Delta\mathrm{R}(\ell - b_1)$

Figure 5.13: A set of pre-fit histograms comparing data against simulation in the $t\bar{t}Z$ CR of the sub-leading lepton for the variables $m_{\ell b_1}$, $\Delta\mathrm{R}(\ell - b_0)$ and $\Delta\mathrm{R}(\ell - b_1)$.

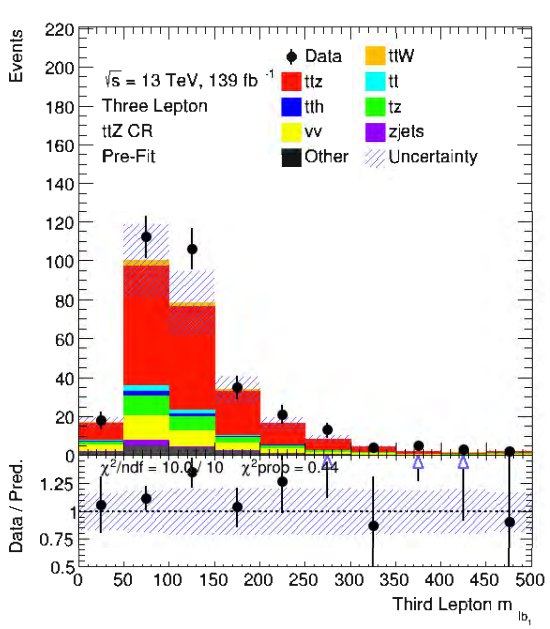

(a) Third lepton $m_{\ell b_1}$

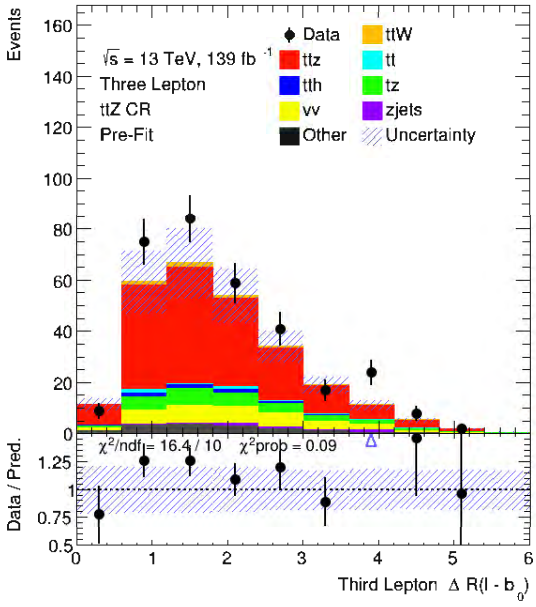

(b) Third lepton $\Delta\mathrm{R}(\ell - b_0)$

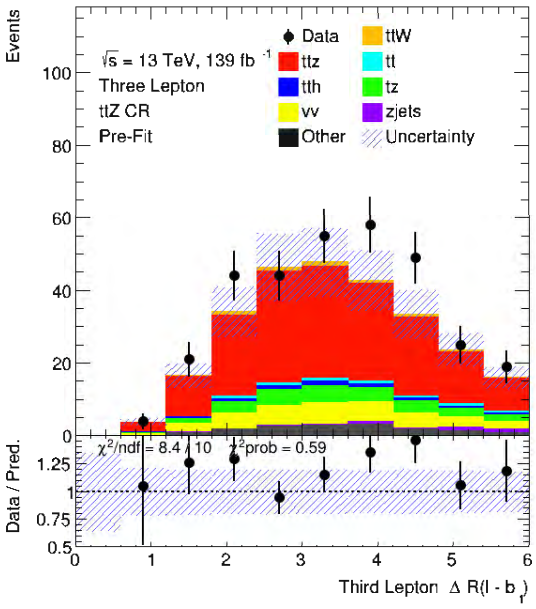

(c) Third lepton $\Delta\mathrm{R}(\ell - b_1)$

Figure 5.14: A set of pre-fit histograms comparing data against simulation in the $t\bar{t}Z$ CR of the third lepton for the variables $m_{\ell b_1}$, $\Delta\mathrm{R}(\ell - b_0)$ and $\Delta\mathrm{R}(\ell - b_1)$.

ML algorithm, the differences between the methods are minimal. Since the GTB has the highest AUC, this algorithm will be used in the lepton-top association. Table 5.10 shows the variable ranking table where each variable is ranked by its importance for the GTB algorithm. The variable importance is calculated by counting how often the variable is used in the GTB and by the level of separation between signal and background that variable provided [86]. The importance refers to the strength of each variable to discriminate between signal and background.

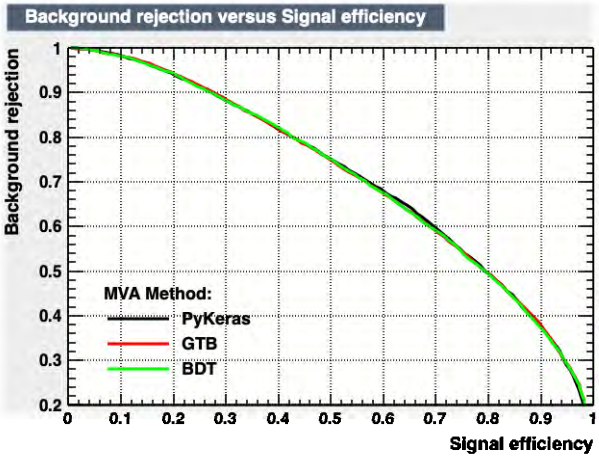

Figure 5.15: The signal efficiency versus the background rejection for three different machine learning methods used in the lepton-top association is shown.

Rank	Variable	Variable Importance
1	$m_{\ell b_0}$	5.456e-01
2	$m_{\ell b_1}$	2.276e-01
3	ΔR(ℓ + b_0)	9.772e-02
4	lepton p_T	6.403e-02
5	ΔR(ℓ + b_1)	3.930e-02

Table 5.10: A table ranking of the different variables used, by their importance for the GTB algorithm is shown.

Table 5.10 shows that $m_{\ell b_0}$ of the lepton matched with the closest b-jet is the best variable as given by the variable importance metric. This follows from the $m_{\ell b}$ algorithm, where it was found that the $m_{\ell b_0}$ variable provided the best discrimination between signal and background. The second variable in the table is the $m_{\ell b_1}$ of the lepton matched with the second closest b-jet. The importance assigned to this variable is of the same order of magnitude as the $m_{\ell b_0}$. These two variables provide most of the discrimination within the GTB algorithm. Figure 5.16 shows the GTB response for the signal (leptons from top

quarks) and background (leptons from ISW's) shown in blue and red respectively. The test and training samples are shown as histograms and points, respectively, for both signal and background classes. The reason for this plot is to test that the agreement between the test and training set is good. Poor agreement between the two sets would indicate that the ML algorithm has been overtrained and as a result will not generalise well to other data sets. It can be seen that almost all of the bins agree within 1σ and all of the bins agree within 2σ indicating that the agreement between the training and test data sets are adequate. This agreement implies that the algorithm has not been overtrained.

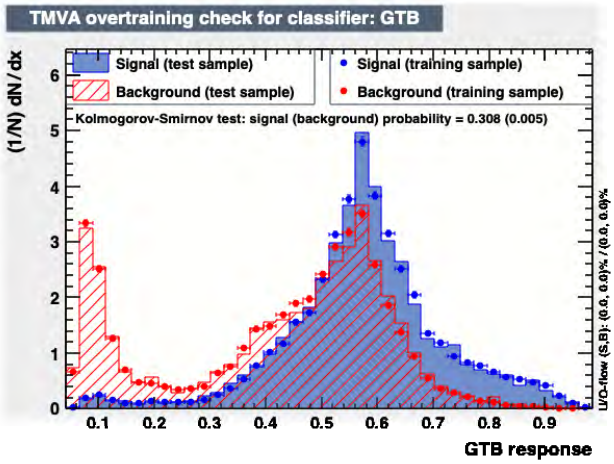

Figure 5.16: A histogram of the normalised signal (red) and background (blue) distributions of the output of the GBT response for both train and test samples is shown.

When identifying the leptons which decayed from top quarks the following process is applied. The odd lepton is identified based on its charge. This is followed by passing the remaining even leptons through the GTB algorithm which will then assign the even leptons with a GTB score. The score assigned is a number between zero and one where a GTB score of 1 strongly indicates that the lepton decayed from a top quark whereas a score of 0 strongly indicates that the lepton decayed from an ISW boson. The even lepton with the highest GTB score is then identified as a lepton that decayed from a top quark. Using the GTB algorithm, leptons decaying from top quarks were correctly identified with an efficiency of 72.7% of events. The odd lepton and the lepton identified using the lepton-top association are then used to calculate the Δ_η^ℓ. The ML algorithm does not provide a perfect identification of leptons decaying from top quarks and as such will select the ISW lepton some portion of the time. The pseudorapidity of the ISW lepton is random with respect to that of the odd lepton. As a result, when the ISW lepton is identified as a lepton decaying from a top quark the calculation of the Δ_η^ℓ calculated has an equal chance of being positive or negative. The incorrect association causes a portion of the Δ_η^ℓ distribution for $t\bar{t}W^\pm$ to be symmetric which dilutes the A_C^ℓ. Figure 5.17 shows the Δ_η^ℓ distribution, calculated using the lepton-top association is shown in the $t\bar{t}Z$ CR. The uncertainties shown are as

outlined in section 5.6 and the y-axis shows the number of events. The agreement between simulation and data is within 1σ indicating good agreement between the two. The good agreement indicates that the Δ_η^ℓ variable as calculated using the lepton-top association is modelled well and can be used to extract the A_C^ℓ in $t\bar{t}W^\pm$.

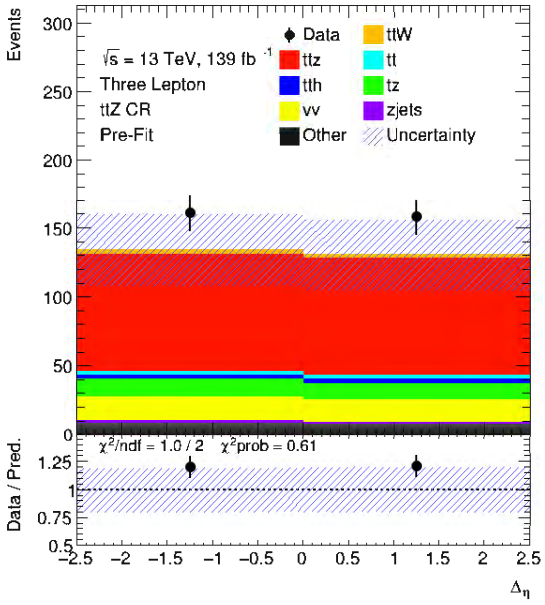

Figure 5.17: A figure comparing the data to simulation for the Δ_η^ℓ distribution in the $t\bar{t}Z$ CR is shown. The Δ_η^ℓ is calculated using the lepton-top association.

5.8 The A_C^ℓ extraction

This section discusses the methods used to extract the A_C^ℓ in $t\bar{t}W^\pm$. Both of the methods discussed in this section utilise a method called maximum likelihood estimation and a brief discussion of the maximum likelihood estimation method is presented in section 5.8.1. Section 5.8.2 discusses the sources of uncertainty that were taken into account as well as the blinding strategy implemented in this measurement. The two methods used to extract the A_C^ℓ are called Template Morphing (TM) and the Fit Across Regions (FAR) which are outlined in sections 5.8.4 and 5.8.5 respectively where the methodology and results are discussed for both. Finally, in section 5.8.6, an estimation of the expected uncertainties in future measurements of the A_C^ℓ in $t\bar{t}W^\pm$ at higher luminosity is investigated.

5.8.1 Maximum likelihood estimation

The method of maximum likelihood estimation (MLE) is used to estimate the value of a model parameter given a measured data set. In the case of this measurement, binned distributions, containing both signal and background processes are used to extract the parameter of interest (POI). The POI is the A_C^ℓ, which is determined from the yields with positive and negative Δ_η^ℓ represented by μ_{plus} and μ_{minus}, respectively. It is important to take into account sources of uncertainty, both statistical and systematic. The systematic uncertainties are included in the fit as NP and are represented using θ. The probabilities of the bin heights in data are estimated according to a Poisson ($\mathcal{P}$). The p.d.f. for each of the NP's are represented by Gaussian ($\mathcal{G}$) distributions. Equation 5.7 shows the likelihood function for binned distributions [87].

$$L(n|\mu,\theta) = \prod_{i\in bins} \mathcal{P}\left(n_i|\mu S_i(\theta) + B_i(\theta)\right) \times \prod_{j\in syst} \mathcal{G}\left(\theta_j^0|\theta_j, \Delta\theta\right) \tag{5.7}$$

Where S_i and B_i show the estimated amounts signal and background in bin i. The θ^0 are the nominal values for the NP's with the $\Delta\theta$ being the uncertainties on those values. The estimation of the parameters is performed by varying each of the parameters within the fit. If the θ values provided are good estimates for the real values then a high value should be returned for the likelihood. On the other hand, if the proposed values are poor representations for the real parameters they should return a low value for the likelihood. Therefore the aim is to find the set of parameters which maximise the probability of the data.

5.8.2 Blinding and uncertainties

Blinding is the withholding of information that could influence researchers by introducing biases. The reason blinding is used is to minimise the chance of introducing a bias into the measurement. In the case of this measurement the information which is withheld is the data in the SR and $t\bar{t}$ regions as these regions are enriched in our signal process. The measurement of the A_C^ℓ in $t\bar{t}W^\pm$ has remained blinded since the research forms part of a larger ATLAS analysis. The results shown will be a fit to Asimov data which is a fictional data set where all of the observed quantities are set equal to their expectation values [88]. This means that the A_C^ℓ and its uncertainties are measured in this idealised, blind situation. The only time data has been used in this measurement is in as the $t\bar{t}Z$ CR is used which contains a limited number of signal events.

Several systematic uncertainties are included in this measurement as NP. For each NP

the expected amount of variation is also quoted. These uncertainties can be broken down into theoretical uncertainties and experimental uncertainties. The theoretical uncertainties considered in this measurement are concerned with the theoretical prediction of the cross section for several of the processes considered which correspond to $t\bar{t}W^{\pm}$, $t\bar{t}Z$, $t\bar{t}$, tZ, and $t\bar{t}H$. The $\Delta\theta$ applied to each cross section listed are 30 %, 15 %, 50 %, 14 %, and 15 %. The $t\bar{t}W^{\pm}$ and $t\bar{t}Z$ variations are taken from the following source [9]. The large variation applied to the $t\bar{t}$ sample is used to estimate the fake contribution to the measurement. The variation for the tZ and $t\bar{t}H$ processes are taken from [89] and [90] respectively. The experimental uncertainties which are included correspond to uncertainties on the luminosity, trigger efficiencies, JVT, pile-up, and b-tagging. It should be noted that the NPs corresponding to the cross sections only affect the normalisation of the samples while the experimental NP's affect the shape and normalisation of the distributions. Although several sources of uncertainties are included in this measurement it is by no means complete and future measurements of A_C^ℓ in $t\bar{t}W^{\pm}$ will need to take all sources of uncertainty into account. It should be noted that the uncertainties considered are the dominant sources of uncertainty and as a result, the uncertainty extracted for the A_C^ℓ may still be well estimated as it is dominated by statistical uncertainty.

5.8.3 The A_C^ℓ and the cross section

To A_C^ℓ will be extracted using the Δ_η^ℓ which will be split into two bins which are a bin with Δ_η^ℓ being greater than zero and one where it is less than zero. The equation for the A_C^ℓ is given in equation 5.8 which requires the number of events with a positive and negative Δ_η^ℓ.

$$A_C^\ell = \frac{N(\Delta_\eta^\ell > 0) - N(\Delta_\eta^\ell < 0)}{N(\Delta_\eta^\ell > 0) + N(\Delta_\eta^\ell < 0)} \tag{5.8}$$

The A_C^ℓ is a purely shape effect where a shape effect is an effect that only represents itself in the shape of the histogram and does not depend on the normalisation of said histogram For the A_C^ℓ this means that it is independent of the $t\bar{t}W^{\pm}$ cross section. The sum of $t\bar{t}W^{\pm}$ events can be calculated by counting the expected number of events with a positive and negative Δ_η^ℓ as show in equation 5.9.

$$N_{tot} = N(\Delta_\eta^\ell > 0) + N(\Delta_\eta^\ell < 0) \tag{5.9}$$

If the $t\bar{t}W^{\pm}$ cross section is changed by a factor of δ the sum would in turn change by the same amount and would affect the normalisation of the Δ_η^ℓ distribution. Since the cross

section is a normalisation as discussed in section 5.4.3, the number of events with a positive and negative Δ_η^ℓ would change by the same δ. This means that equation 5.8 would become equation 5.10.

$$A_C^\ell = \frac{\delta \cdot N(\Delta_\eta^\ell > 0) - \delta \cdot N(\Delta_\eta^\ell < 0)}{\delta \cdot N(\Delta_\eta^\ell > 0) + \delta \cdot N(\Delta_\eta^\ell < 0)} \tag{5.10}$$

In equation 5.10 the factor of δ can be factored out of both the numerator as well as the denominator, causing it to cancel. This means that the cross section can vary independently of the A_C^ℓ and as a result measuring the A_C^ℓ provides an independent test of the modelling of the $t\bar{t}W^\pm$ process.

5.8.4 Template morphing

The first method investigated is called Template Morphing (TM) and is used to extract the POI based on the shape of the associated distribution. In the case of A_C^ℓ, the distribution corresponding to the POI is the Δ_η^ℓ distribution. The Δ_η^ℓ distribution is binned symmetrically around 0 and a two-bin distribution is used. This means that varying the relative amounts in the two bins while keeping the integral of the distribution constant will cause a corresponding change in the A_C^ℓ. It is this fact which template morphing aims to exploit. Since the A_C^ℓ is independent of the $t\bar{t}W^\pm$ cross section this measurement will be a pure shape-effect and will be implemented using the TRExFitter framework [91].

The TM method uses two distributions of the same observable but with different, known amounts of the POI. The two distributions, both using the same binning, are called templates and will have different known amounts of the A_C^ℓ. Due to an imperfect selection in the lepton-top association, the A_C^ℓ present in the reconstructed Δ_η^ℓ distribution will be diluted to some extent. However, the A_C^ℓ at detector level can be calculated - in simulation - with perfect selection of leptons decaying from top quarks due to the truth matching discussed in section 5.7.2. It is this A_C^ℓ at detector level calculated using perfect selection which will be extracted using the TM fit. The extraction is performed by associating the templates with the A_C^ℓ at detector level with perfect selection. In doing so the fit applies correction for the imperfect selection due to the lepton-top association. To measure the POI a new distribution is produced by linearly interpolating between the two distributions allowing the bins and the corresponding POI to vary. The interpolated distribution is checked against the data and the likelihood is calculated. The interpolated distribution with the maximum likelihood is then taken as the best fit which will correspond to the value of the POI measured [65]. The

templates are created by varying the event weights algorithmically depending on whether the event has a positive or negative Δ_η^ℓ. The variation of weights requires the following information: the total yields of the $t\bar{t}W^\pm$ sample, the number of events with a positive Δ_η^ℓ $\left(N_{nom}\left(\Delta_\eta^\ell > 0\right)\right)$ and the number of events with a negative Δ_η^ℓ $\left(N_{nom}\left(\Delta_\eta^\ell < 0\right)\right)$. This information will then be used to calculate the templates. The equations shown in 5.11 are used to calculate the number of events required to have a positive and negative Δ_η^ℓ for a specific A_C^ℓ.

$$N_{new}(\Delta_\eta^\ell < 0) = \frac{I}{2} \cdot (1 + A_C^\ell), \quad N_{new}(\Delta_\eta^\ell > 0) = I - N_{new}(\Delta_\eta^\ell < 0) \tag{5.11}$$

The information from equation 5.11 is used to create a scaling factor that increases or decreases the weight of an event depending on whether it has a positive or negative Δ_η^ℓ. For example, if a positive A_C^ℓ is desired then events with a positive Δ_η^ℓ are weighted up and the negative events are weighted down. The scaling factors for this weighting are calculated using equation 5.12. If the Δ_η^ℓ is greater than zero in an event then the event weight is scaled by the δ_+ whereas if the Δ_η^ℓ is less than zero then the event weight is scaled by the δ_-. By altering the weights as described a predetermined A_C^ℓ can be precisely propagated into the $t\bar{t}W^\pm$ sample across all distributions. The templates created using this method will have an A_C^ℓ of -0.5 and 0.5 A_C^ℓ respectively.

$$\delta_- = \frac{N_{new}(\Delta_\eta^\ell < 0)}{N_{nom}(\Delta_\eta^\ell < 0)}, \quad \delta_+ = \frac{N_{new}(\Delta_\eta^\ell > 0)}{N_{nom}(\Delta_\eta^\ell > 0)} \tag{5.12}$$

To ensure that the TM method can reliably measure the A_C^ℓ a signal injection test was performed. A fictional data set is created for this purpose and as follows. A $t\bar{t}W^\pm$ sample was created with a specific A_C^ℓ using the same process used to create the templates. The new $t\bar{t}W^\pm$ sample is then combined with the background sample to create a fictional data set with the same integral as the simulation but with a different expected A_C^ℓ in $t\bar{t}W^\pm$. The TM method is then used to fit the simulation to the fictional data set and the A_C^ℓ is measured. The observables used for extracting the A_C^ℓ in the TM fit for each of the regions are as follows. The two signal regions and the two $t\bar{t}$ regions are plotted using the Δ_η^ℓ variable. The $t\bar{t}Z$ CR is plotted using sum of the transverse momentum for all the jets in the system known as H_T. The $t\bar{t}Z$ CR is used to constrain the $t\bar{t}Z$ process and to a lesser degree the tZ and VV processes. As such the H_T observable was used as $t\bar{t}Z$ process has - on average - a higher jet multiplicity and thus a larger H_T than either tZ or VV. This process was

repeated for several values of A_C^ℓ between -0.5 and 0.5. Figure 5.18 shows the results of the signal injection test. The measured A_C^ℓ is on the y-axis and the injected A_C^ℓ is on the x-axis. The measured A_C^ℓ is plotted as a blue box with error bars shown which include both statistical and systematic uncertainties. If the TM method can reliably measure the A_C^ℓ it would return the exact value injected. This ideal situation is shown in the plot by the red line indicated by y = x. Figure 5.18 shows that the measured A_C^ℓ matches well with the ideal situation shown in the red line and is a strong indication that the template morphing method can reliably measure the A_C^ℓ. The extracted values which correspond to an injected A_C^ℓ less than -0.1 all fall below the expected red line. This indicates that there is a slight bias in the extraction method, however this effect is small enough to be considered negligible.

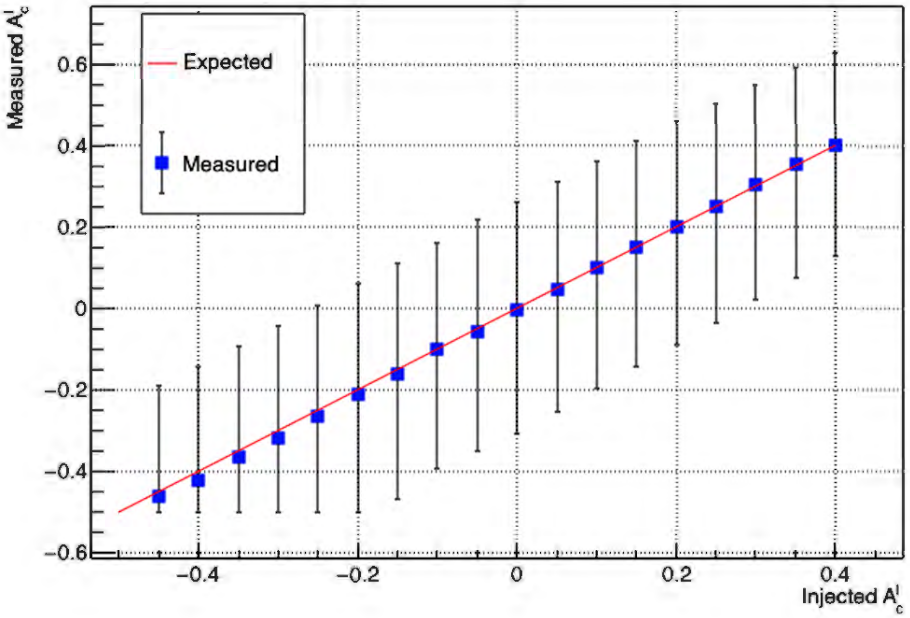

Figure 5.18: The signal injection test run for the TM method is shown where the x-axis shows the A_C^ℓ injected and the y-axis shows the measured A_C^ℓ. The red line of y = x indicates the situation where the fit extracts the exact value which was injected.

The results shown in figure 5.18 show that the TM method is working as expected and will be used to extract A_C^ℓ from an Asimov data set corresponding the SM expectation. The post-fit plots across the 5 regions are shown in figure 5.19. The plots shown are blinded as discussed in section 5.8.2. The uncertainties shown in these plots are as defined in section 5.8.2. There are several points to take away from the plots shown in figure 5.19. It should be noted that across all of the regions the signal purity is relatively low and is due to the large number of background processes populating these regions. The purity of these regions is correlated to how accurately the A_C^ℓ can be measured. The SR and $t\bar{t}$ low jet regions are the regions most sensitive to $t\bar{t}W^\pm$ so reducing the background contribution in these regions would increase the sensitivity of the measurement. Of the processes considered in figure 5.19

only processes with two leptons decaying from top quarks should exhibit an asymmetry. As a result, processes without two leptons decaying from top quarks will result in the lepton pairs being randomly oriented with respect to each other in terms of Δ_η^ℓ which causes the process to be symmetric.

The results of the TM fit are shown in table 5.11 for two cases. These cases correspond to when only statistical sources of uncertainty are considered compared with both statistical and systematic sources of uncertainty. Comparing the uncertainties measured between the two it should be noted that they are similar in size. This implies that the dominant source of uncertainty is due to the statistical uncertainties. The true A_C^ℓ predicted by the SM at detector level in this region of phase space is estimated using simulation and corresponds to a A_C^ℓ of -8.7% $\pm$ 3.1%. Since this measurement is blinded the extracted A_C^ℓ should match the expected A_C^ℓ almost exactly which is the case.

Uncertainties considered	$\mathbf{A_C^\ell}$ [%]
Statistical	-9^{+30}_{-30}
Total	-9^{+30}_{-32}

Table 5.11: A table of the A_C^ℓ measured using the TM method is shown. The measurement was performed with only statistical uncertainties as well as with systematic uncertainties included.

Although the dominant source of uncertainties is the statistical uncertainty, it is still useful to quantify the impact of each of the NP. The impact ($\Delta\mu$) is used to assess the effect of each of the NP of the A_C^ℓ extraction. The nominal pre-fit values for each NP are set to one and are denoted by θ_0 while the pre-fit uncertainties are denoted by $\Delta\theta$. The $\Delta\theta$ is set equal to one unless stated otherwise in section 5.8.2. The $\Delta\mu$ for each NP is calculated by comparing the predicted pre-fit value of A_C^ℓ with the result of the fit when the NP under consideration is fixed to its best-fit value, $\hat{\theta}$, shifted by its pre-fit (post-fit) uncertainties $\Delta\theta$ ($\Delta\hat{\theta}$) [92]. Figure 5.20 shows the ranking plot for several of the NP considered. The empty blue rectangles show the pre-fit impact on the A_C^ℓ while the filled blue rectangles show the post-fit impacts. The bottom axis shows the NP pull which is given by $\frac{(\hat{\theta}-\theta_0)}{\Delta\theta}$ where the $\hat{\theta}$ is best-fit value, the θ_0 is the nominal pre-fit value. The NP pulls are shown by black dots with their corresponding uncertainties. The top axis shows the impact $\Delta\mu$ where each of the NP is listed in descending order of their impact on the A_C^ℓ measurement. Due to the fit being blinded all of the NP pulls correspond to a value of zero as expected. It can

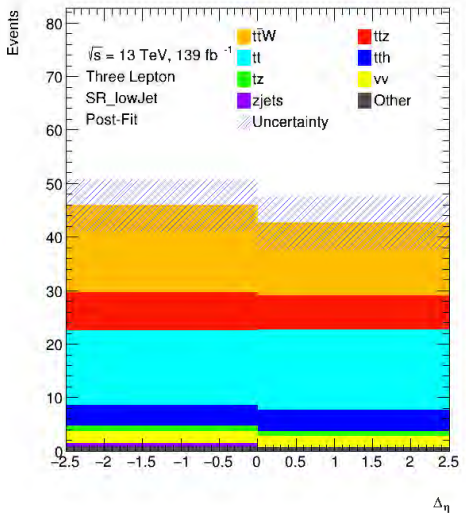

(a) SR low jet

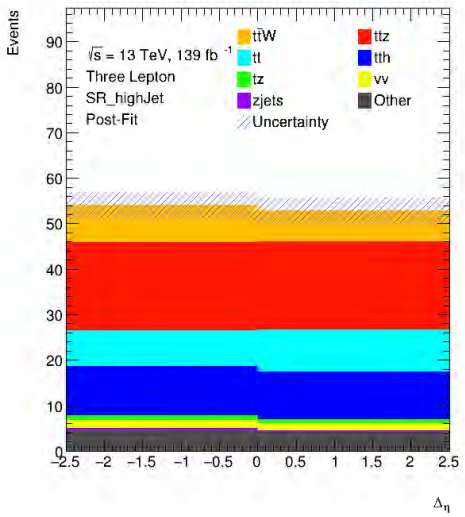

(b) SR high jet

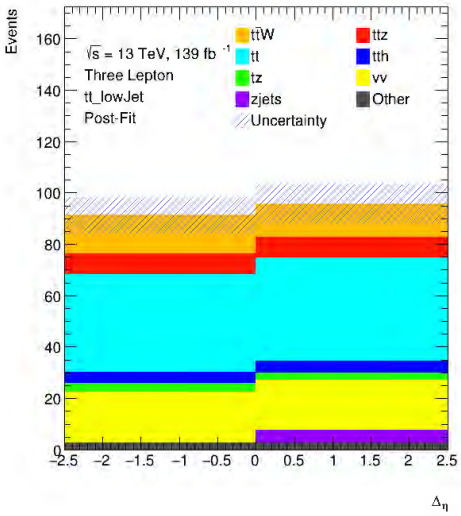

(c) $t\bar{t}$ low jet

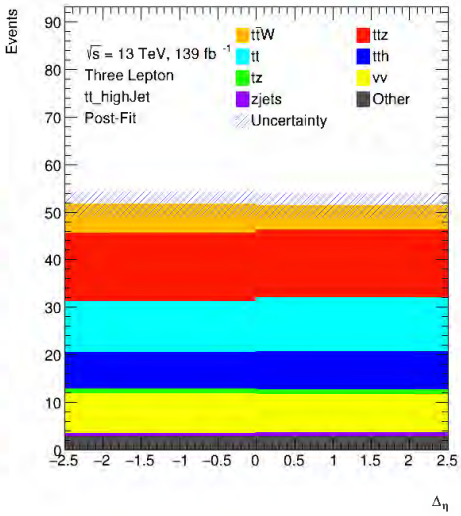

(d) $t\bar{t}$ high jet

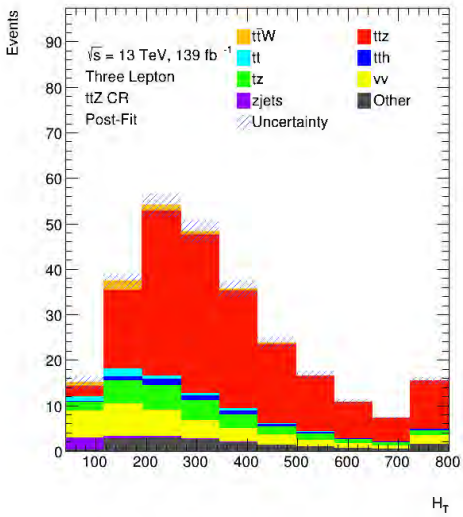

(e) $t\bar{t}Z$ CR

Figure 5.19: A set of blinded post-fit histograms of the five regions used in this fit are shown. The two SR regions and the two $t\bar{t}$ regions use the Δ_η^ℓ variable while the $t\bar{t}Z$ CR uses H_T.

be seen that two NP with the greatest impact on the measurement is the $t\bar{t}W^{\pm}$ and $t\bar{t}$ cross sections. The reason the pre-fit impact of $t\bar{t}$ is so large is to model the fake contribution due to the $t\bar{t}$ process. Figure 5.21 shows the correlation matrix for several of the NP considered in the fit. As discussed in section 5.8.3 the A_C^ℓ and cross section of $t\bar{t}W^{\pm}$ should be independent and should have a minimal impact on the A_C^ℓ measurement. The reason the $t\bar{t}W^{\pm}$ cross section has such a large impact is due to a large correlation between the NPs for the $t\bar{t}W^{\pm}$ and $t\bar{t}$ cross sections within the fit. This correlation can be seen in figure 5.21 where the strongest correlation is between the NP for the$t\bar{t}$ and $t\bar{t}W^{\pm}$ cross sections. Although the TM method is able to extract the A_C^ℓ there are several short-comings of this method specifically the large uncertainties and the correlation of the $t\bar{t}W^{\pm}$ and $t\bar{t}$ cross sections. In the next section these short-comings will be addressed and improve the A_C^ℓ extracted.

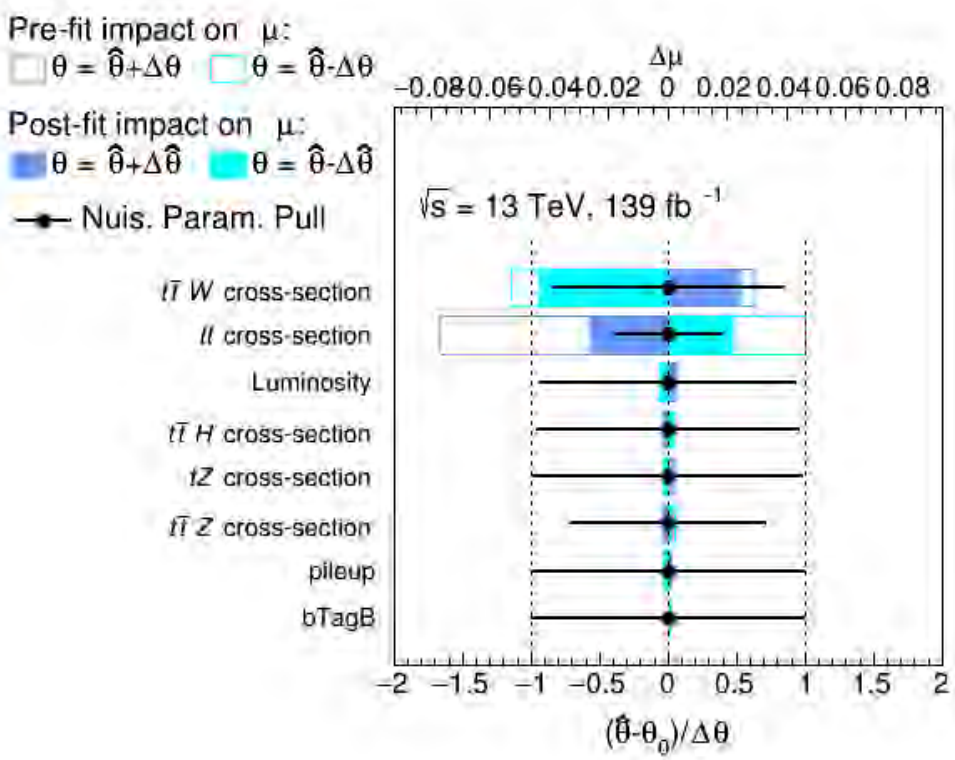

Figure 5.20: A figure ranking the impact of several of the NP considered in the fit. The bottom axis shows the plot of the NP pull $\left(\frac{(\hat{\theta}-\theta_0)}{\Delta\theta}\right)$ while the top axis shows the impact ($\Delta\mu$). The empty (filled) blue rectangles show the pre-fit (post-fit) impact on the A_C^ℓ. The NP are ranked in by their impact in descending order.

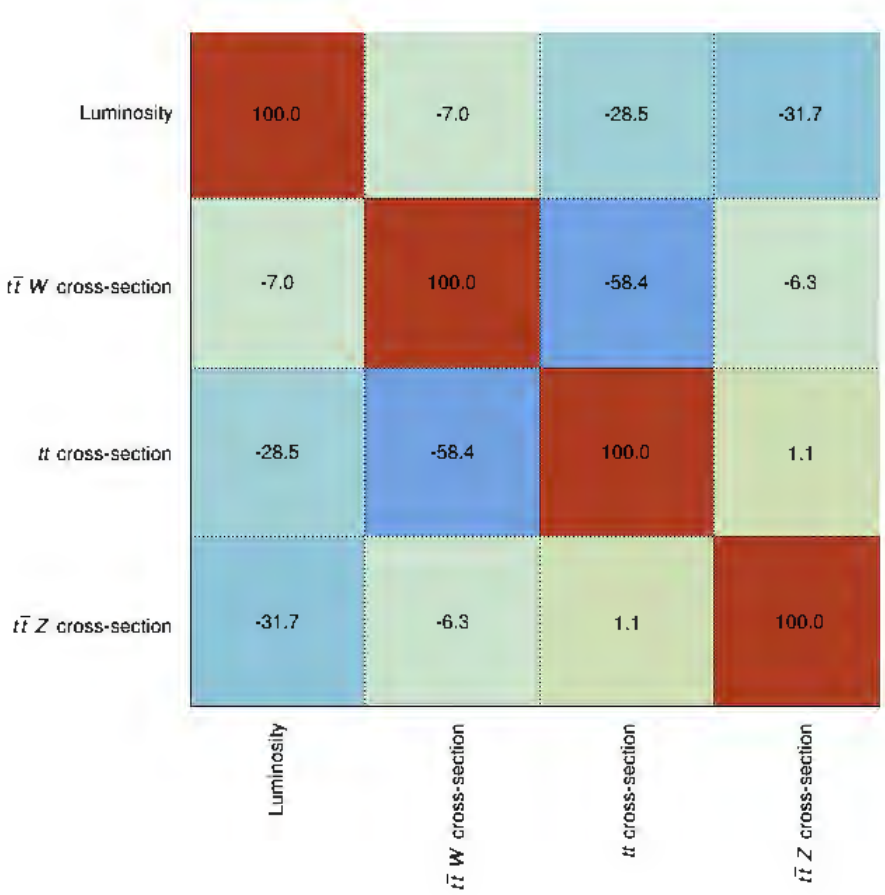

Figure 5.21: A correlation matrix is shown which provides the correlation between the normalisation NP's included in the TM fit.

5.8.5 Fit Across Regions

In section 5.8.4, the measurement of the A_C^ℓ used a two-bin distribution of the Δ_η^ℓ observable. The left bin provides the yields for the number of events with a negative Δ_η^ℓ while the right bin corresponds to the positive number of events where each bin contains more background than signal. The goal is to take the positive and negative bins in each region and bin them in terms of a variable that discriminates between signal and background processes. The discriminating variable will be created using ML as this will provide much stronger discrimination than any single variable. This new fit method is called the Fit Across Regions (FAR).

The FAR method is implemented by varying the yields in the negative and positive regions - this time independently of each other using two normalization factors for the positive and negative regions respectively. The varied yields will be checked against data and the likelihood will be calculated. The normalisation factors which correspond to a maximum in the likelihood will be used to calculate the A_C^ℓ which has been implemented using the TRExFitter framework [91]. The A_C^ℓ measured using this process does differ slightly as there is no correction applied for the lepton-top association. As a result, this method measures the reconstructed A_C^ℓ at detector level. The first step in the measurement process is training an ML algorithm to differentiate between signal and background processes. Two machine learning algorithms were trained for this purpose specifically a gradient boosted classifier (gBDT) and an ADA boosted classifier (ADA). The process of training the ML algorithms is outlined in the flowchart shown in figure 5.22 which starts by splitting the simulation in half. One half will be used to train the ML algorithms while the other half is used for the fit. Once the ML algorithms are trained the best-performing one will be selected and used to calculate the ML scores on the second half of the simulation as well as on the data. The distributions of the ML scores will then be used in the fit to measure the A_C^ℓ.

The ML algorithms were trained using events from all of the regions. Several variables were identified for this purpose and are the H_T, $E_{\mathrm{T}}^{\mathrm{miss}}$, $m_{\ell\ell_0}$ OS, $m_{\ell\ell_1}$ OS and the $m_{\ell\ell\ell}$. The $m_{\ell\ell}$ OS is the combined invariant mass of the odd lepton and each of the even leptons order by p_T while the $m_{\ell\ell\ell}$ is the combined invariant mass of all three leptons included in the event. Figure 5.23 shows the normalised distributions of $t\bar{t}W^\pm$ (blue) and all the background processes (orange) which combine events from all of the regions defined in table 5.6. These distributions serve to highlight differences in the shapes of the distributions between $t\bar{t}W^\pm$ and the backgrounds and the modelling of each of these variables needs to be verified.A comparison between simulation and data for the H_T and $E_{\mathrm{T}}^{\mathrm{miss}}$ observables was investigated in section 5.6 where the agreement was found to be adequate. A similar comparison is done for the remaining variables, $m_{\ell\ell_0}$ OS, $m_{\ell\ell_1}$ OS and the $m_{\ell\ell\ell}$, to ensure that they are modelled well. A comparison between simulation and data is shown in figure 5.24 in the $t\bar{t}Z$ CR. The

Figure 5.22: A flow chart detailing the process used to train the event-level machine learning algorithms is shown.

uncertainties are as discussed in section 5.8.2 and are shown as vertical lines for data and a band of diagonal blue lines shows the uncertainty for simulation. The y-axis shows the number of events. The agreement of these observables is generally within 1σ however two bins do not agree within 1σ. These occur in figure 5.24a in the first bin from the left and in figure 5.24b in the third bin from the left. These bins do not agree within 1σ but do agree within 2σ indicating that the modelling of these variables is adequate and can be used to train an ML algorithm.

The results of the training are presented in the following paragraphs with figure 5.25 showing the receiver operating curve (ROC) for the ML algorithms which were tested. The x-axis shows the false positive rate while the y-axis shows the true positive rate. The two ML methods trained are shown in this figure which are the gBDT (blue) and the ADA (orange) classifiers. A dashed line of y = x is shown which indicates what the ROC curve would be if signal and background were chosen at random. The AUC is used as a proxy for the performance of the ML algorithms where the AUC for the gBDT is 0.779 while the ADA is 0.768. Since this is a proxy for the strength of the algorithm's ability to discriminate between signal and background going forward the gBDT will be used to discriminate between $t\bar{t}W^{\pm}$ and the background processes. It should be noted that since both of the algorithms are decision trees the difference in AUC should be minimal and is the case as shown in figure 5.25. The differences that are noted are from one of two sources with the first option being that the gBDT has been more optimised than the ADA. The second is due to an unfavourable randomised initial state for the ADA as compared to the gBDT causing the differences. Since the gBDT performs slightly better than the ADA the majority of the time the difference is likely due to the gBDT being slightly more optimised for the task. The event-level gBDT

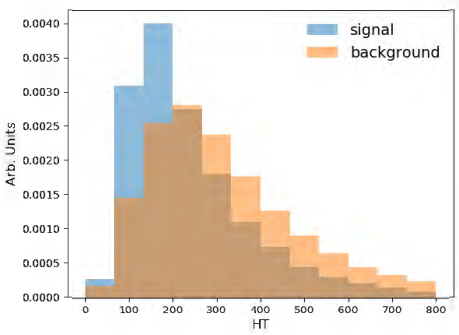

(a) H_T

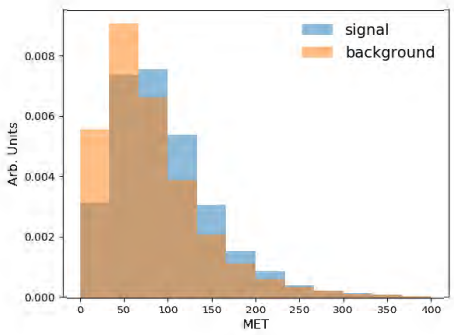

(b) $E_{\mathrm{T}}^{\mathrm{miss}}$

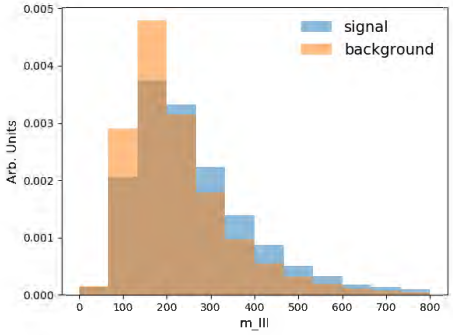

(c) $m_{\ell\ell\ell}$

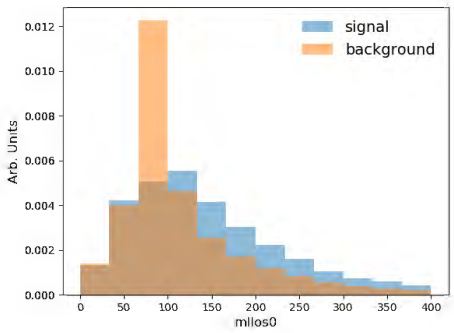

(d) $m_{\ell\ell_0}$ OS

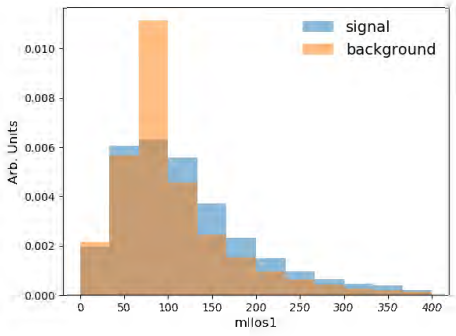

(e) $m_{\ell\ell_1}$ OS

Figure 5.23: The normalised distributions comparing signal ($t\bar{t}W^{\pm}$) to all background processes for several observables are shown. The events included in these plots combine all events which pass the criteria for any of the five regions.

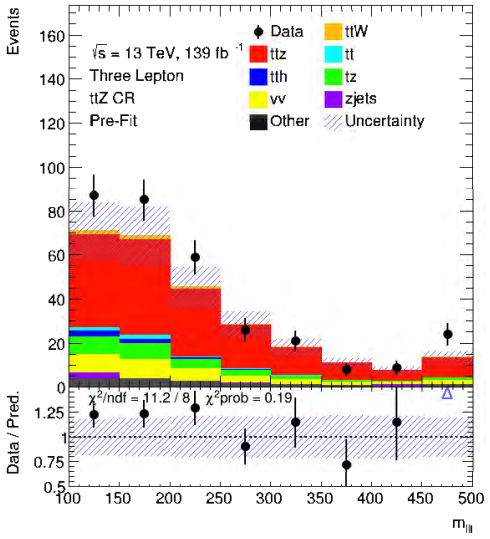

(a) $m_{\ell\ell\ell}$

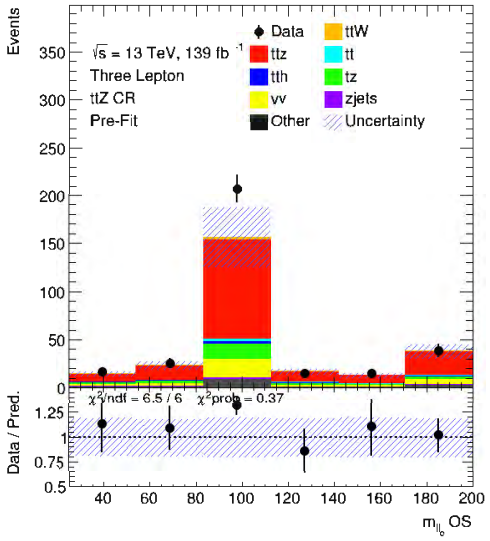

(b) $m_{\ell\ell_0}$ OS

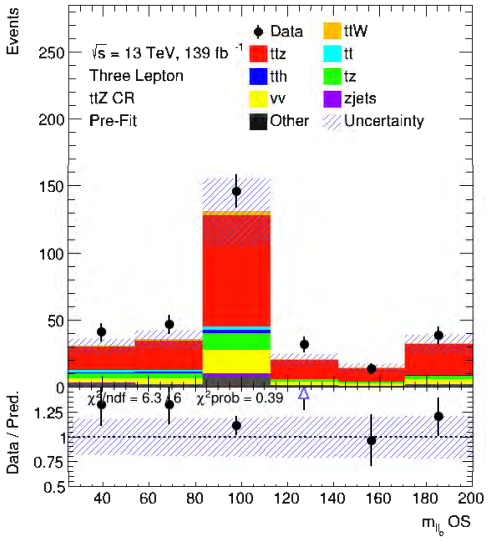

(c) $m_{\ell\ell_1}$ OS

Figure 5.24: A set of pre-fit histograms comparing data and simulation of the (a) $m_{\ell\ell\ell}$, (b) $m_{\ell\ell_0}$ OS, and (c) $m_{\ell\ell_1}$ OS in the $t\bar{t}Z$ control region are shown.

does provide discrimination between signal and background which was deemed adequate for this measurement however further improvements to the discrimination would increase the sensitivity of this measurement. Such improvements could come as a result of further optimising the ML algorithms as well as providing new, independent variables capable of discriminating between signal and background. The use of more sophisticated methods such as deep neural networks could also provide an improvement to the discrimination.

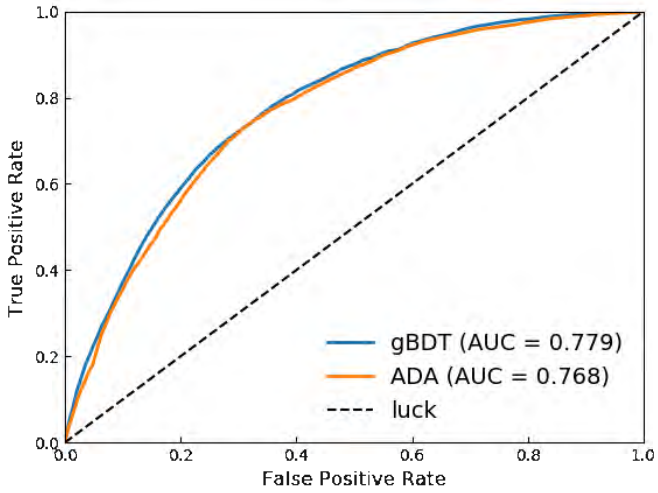

Figure 5.25: The receiver operating curve for the two machine learning algorithms which were trained to discriminate between $t\bar{t}W^{\pm}$ and all background processes is shown. The line y = x indicates what a ROC curve would be if signal and background were chosen at random.

The next check is shown in figure 5.26 which is used to ensure that the gBDT is not being overtrained. Figure 5.26 shows the normalised distributions of the signal (red) and background (blue) classes for both the training (histogram) and the test (point) samples. The variable plotted is gBDT score. Almost all of the bins are in agreement within one standard deviation (1σ). There are a few bins that do not agree within 1σ however they do agree within 2σ. This agreement provides a strong indication that the gBDT algorithm is not being overtrained. The double-peak structure shown in figure 5.26 is assumed to originate from the dominance of one feature in the BDT. This leads to two distinct paths through the tree depending on the value of the dominant variable resulting in a bimodal, double-peak structure in the output discriminator distribution. The output of the ML algorithm will then be calculated for the second half of the simulation as shown in figure 5.22. The gBDT score will be the variable that will be used in the positive and negative Δ_η^ℓ regions to improve discrimination between $t\bar{t}W^{\pm}$ and the background processes. As was performed for the TM fit, a signal injection test was run and the results of this test are shown in figure 5.27. Figure 5.27 shows the injected A_C^ℓ on the x-axis and the A_C^ℓ measured

using the FAR fit is shown on the y-axis. The uncertainties on the measured A_C^ℓ include both statistical and systematic sources of uncertainty as discussed in section 5.8.2. The red dashed line labelled expected shows what the results should return if the fit is working as intended.

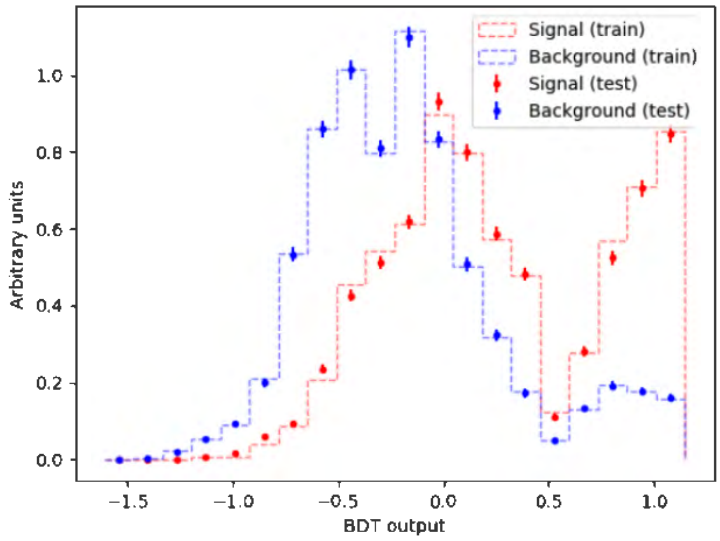

Figure 5.26: A histogram of the normalised signal (red) and background (blue) distributions of the output of the event-level gBDT for both train and test samples is shown.

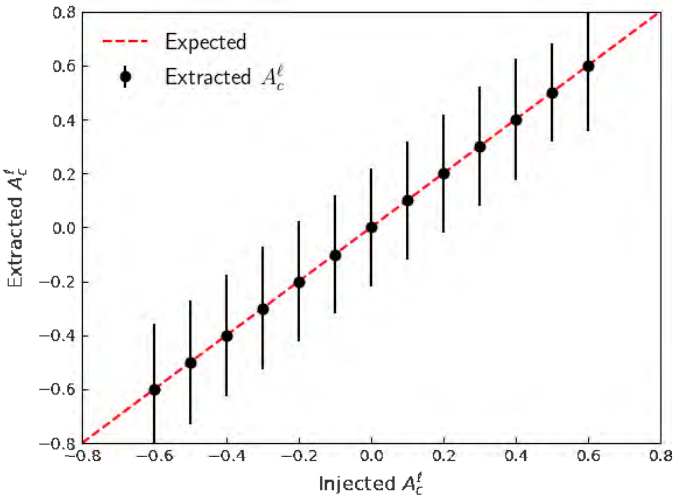

Figure 5.27: The signal injection test for the FAR fit is shown where the x-axis shows the A_C^ℓ injected and the y-axis shows the measured A_C^ℓ.

Figure 5.27 shows that the fit is working as expected as all of the points tested lie on the red line with no discernible deviation. This plot also indicates that this method has a negligible bias. The next step was optimising the regions used in this fit. In the template

morphing section, five regions were used which are: SR low jet, SR high jet, $t\bar{t}$ low jet, $t\bar{t}$ high jet, and the $t\bar{t}Z$ CR. The point then stands on how these regions are split up based on the Δ_η^ℓ variable. The simplest option would use two regions - positive and negative - and plot these in terms of the gBDT score to measure the A_C^ℓ. The most aggressive method splits the original 5 regions based on positive and negative Δ_η^ℓ, resulting in 10 regions in total. The simplest two region fit would not be ideal as it loses some of the constraining power of the original fit as the separate regions were dominated by different backgrounds. The five regions can be split in several possible ways. The SR high and low jet regions are those dominated by $t\bar{t}W^\pm$ and provide much of the sensitivity to the A_C^ℓ. The $t\bar{t}$ high and low jet regions are used to constrain $t\bar{t}$. Lastly, the $t\bar{t}Z$ CR is used to constrain the $t\bar{t}Z$ background. Using these regions the first option is a six region (6R) setup where the SR regions and $t\bar{t}$ regions are combined into a single SR and $t\bar{t}$ region. The SR, $t\bar{t}$ and $t\bar{t}Z$ CR regions are split based on Δ_η^ℓ. The second option considered is splitting all five regions based on Δ_η^ℓ resulting in a ten region (10R) setup. The auto bin feature of the TRExFitter framework was also implemented in the fit for both six and ten region fits. The autobin feature allows the width of the bins to vary to avoid bins with very few events and the results of these tests are shown in table 5.12. To show the effect that the gBDT has on the fit the 6R setup is also binned in terms H_T as shown at the top of the table. The rest of the table is binned in terms of the gBDT score.

Fit Setup	$\mathbf{A_C^\ell}$[%]
$\mathbf{H_T}$	
6R	-8.5 ± 26.6
gBDT score	
6R	-8.5 ± 23.6
6R + Autobin	-8.5 ± 23.1
10R	-8.5 ± 22.7
10R + Autobin	-8.5 ± 22.4

Table 5.12: The measured A_C^ℓ and the corresponding uncertainties for 5 different setups of the FAR fit are shown. The top portion of the table indicates the FAR fit using the H_T distribution while the bottom portion uses the gBDT score.

Table 5.12 shows the result of the FAR fit for several different setups. There are two aspects of the FAR fit and their effects each need to be quantified. The first is splitting the regions up and binning them more finely. This is shown at the top of table 5.12 which shows the 6R setup binned in terms of the H_T variable. Splitting the regions based on Δ_η^ℓ already improves the A_C^ℓ extraction as compared to the TM fit. The 6R setup is then binned in terms of the gBDT score. The improved discrimination due to the gBDT increases the sensitivity of the measurement to the A_C^ℓ and thus further reduces the uncertainties on the

measurement. Comparing the 6R to the 10R setup it can be seen that the uncertainties decrease when using the 10R setup. The decrease is due to the SR and $t\bar{t}$ regions for the 6R setup being split up based on jet multiplicity creating the SR and $t\bar{t}$ low jet regions which have a higher signal purity than any other region. The inclusion of the autobin feature improves the sensitivity of the measurement for both the 6R and 10R setups. Going forward the results quoted will be using the 10R setup binned in terms of the gBDT score with the auto binning feature turned on as this provides the best results.

The blinded post-fit plots are shown in figures 5.28 and 5.29. The layout of these plots matches that shown for equivalent figures shown for the template morphing in figure 5.19 with regards to the ordering of the regions. Figure 5.28 shows the regions with the negative Δ_η^ℓ while figure 5.29 shows the regions with a positive Δ_η. All of these regions use the gBDT score as the variable plotted. The takeaway from the histograms in figures 5.28 and 5.29 is the discrimination of the signal against the background. Across all of the regions, there is a separation between the signal and background where more of the background is towards zero while more of the signal is towards one.

The results of the measurement using the FAR fit are shown in equation 5.13. By splitting the regions based on Δ_η^ℓ and binning these regions in terms of a discriminating variable the uncertainties on the A_C^ℓ have been reduced. The reconstructed A_C^ℓ at detector level as predicted by the SM is given be A_C^ℓ = -8.53%. It should be taken into account that the A_C^ℓ measured using the FAR fit differs from that measured using the TM fit. As a result, it is not a direct comparison between the two methods as the TM method corrects for the deficiency in the lepton-top association. With this in mind, the increase in sensitivity of the FAR fit to the $t\bar{t}W^\pm$ process has greatly reduced the uncertainties when compared to those measured by the TM fit.

$$A_C^\ell = -9\% \pm 22 \tag{5.13}$$

As was shown for the TM fit, a plot showing the impact of several of the NP will be shown in figure 5.20. The empty blue rectangles show the pre-fit impact on the A_C^ℓ while the filled blue rectangles show the post-fit impacts. The bottom axis shows the NP pull ($\frac{(\hat{\theta}-\theta_0)}{\Delta\theta}$). The NP pulls are shown by black dots with their corresponding uncertainties. The top axis shows the impact $\Delta\mu$ where each of the NP is listed in descending order of their impact on the A_C^ℓ measurement. Due to the fit being blinded all of the NP pulls correspond to a value of zero as expected. Comparing figure 5.30 to figure 5.20 it can be seen that the $t\bar{t}W^\pm$ cross section is no longer the dominant NP and is now one of the least dominant. This is in good agreement with the fact that the A_C^ℓ is independent of the cross section. The reason that the impact of the $t\bar{t}W^\pm$ cross section has been reduced is since the $t\bar{t}W^\pm$ and $t\bar{t}$ cross

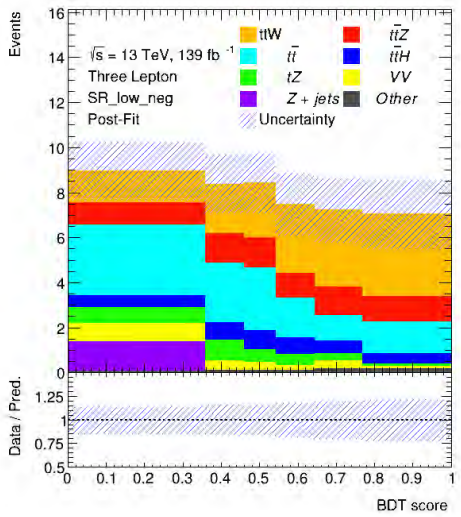

(a) SR low jet

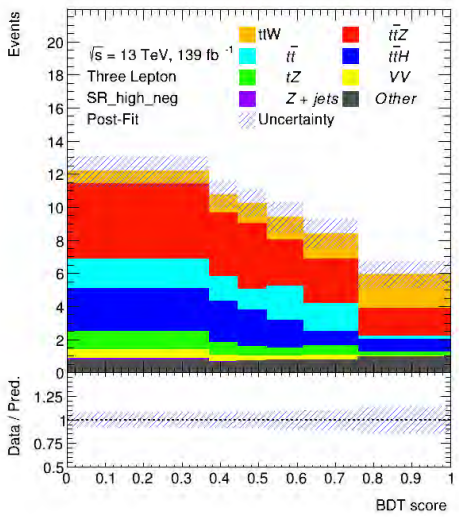

(b) SR high jet

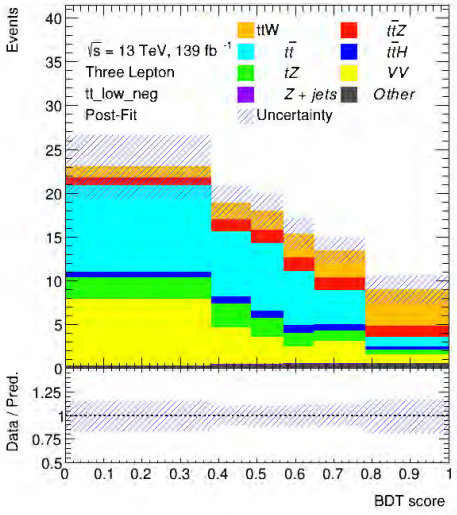

(c) $t\bar{t}$ low jet

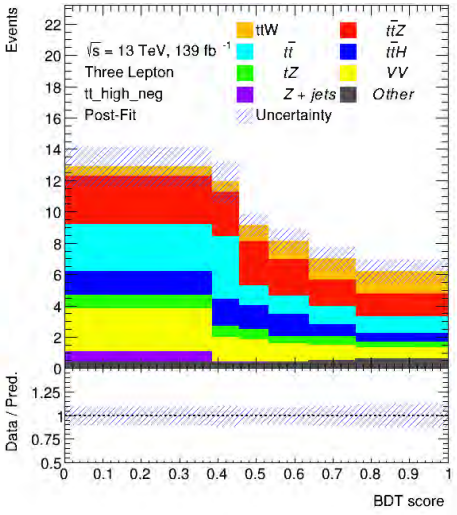

(d) $t\bar{t}$ high jet

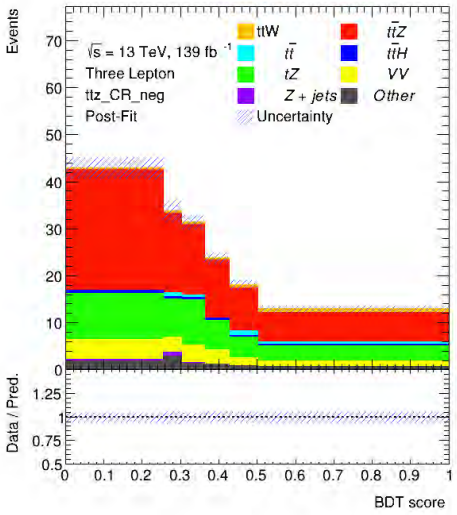

(e) $t\bar{t}Z$ CR

Figure 5.28: A set of blinded post-fit histograms of the five regions with negative Δ_η^ℓ used in the FAR fit plotted in terms of the gBDT output are shown.

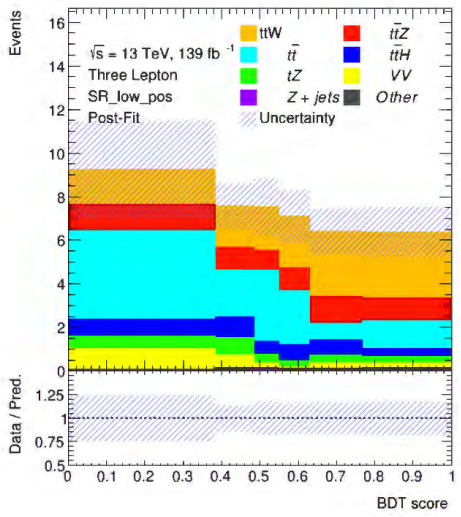

(a) SR low jet

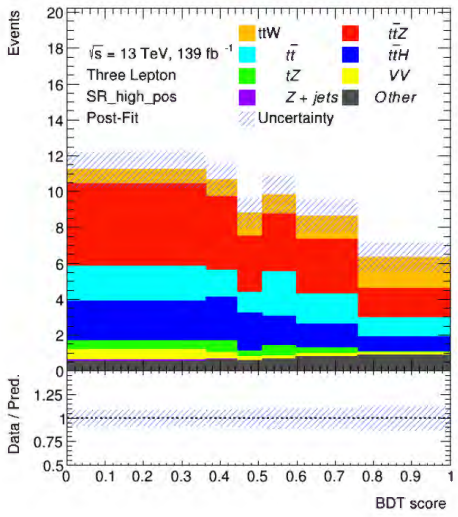

(b) SR high jet

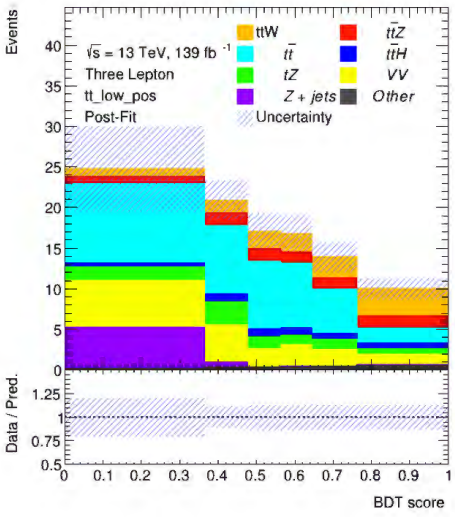

(c) $t\bar{t}$ low jet

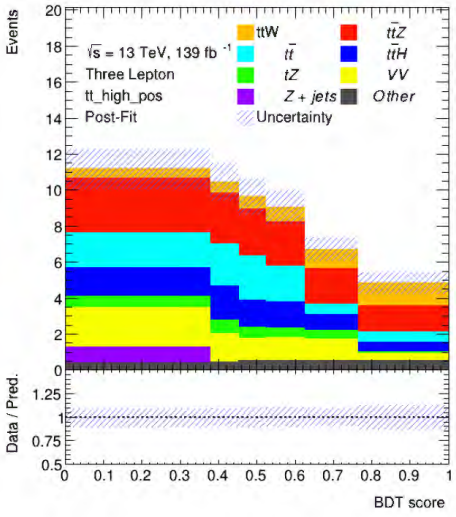

(d) $t\bar{t}$ high jet

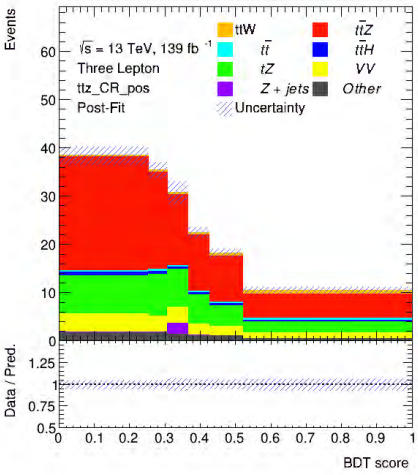

(e) $t\bar{t}Z$ CR

Figure 5.29: A set of blinded post-fit histograms of the five regions with positive Δ_η^ℓ used in the FAR fit plotted in terms of the gBDT output are shown.

sections now have a negligible correlation. In figure 5.31 a correlation matrix is shown which provides the correlation between the normalisation NP's included in the fit. As compared to figure 5.21 there are two additional parameters shown which are the "minus_NF" and the "asymmetry". These two factors correspond to the normalisation factor of the regions with a negative Δ_η^ℓ and the A_C^ℓ extracted. The normalisation factor of the regions with a positive Δ_η^ℓ is not shown as it is directly calculated using the "minus_NF" and the "asymmetry".

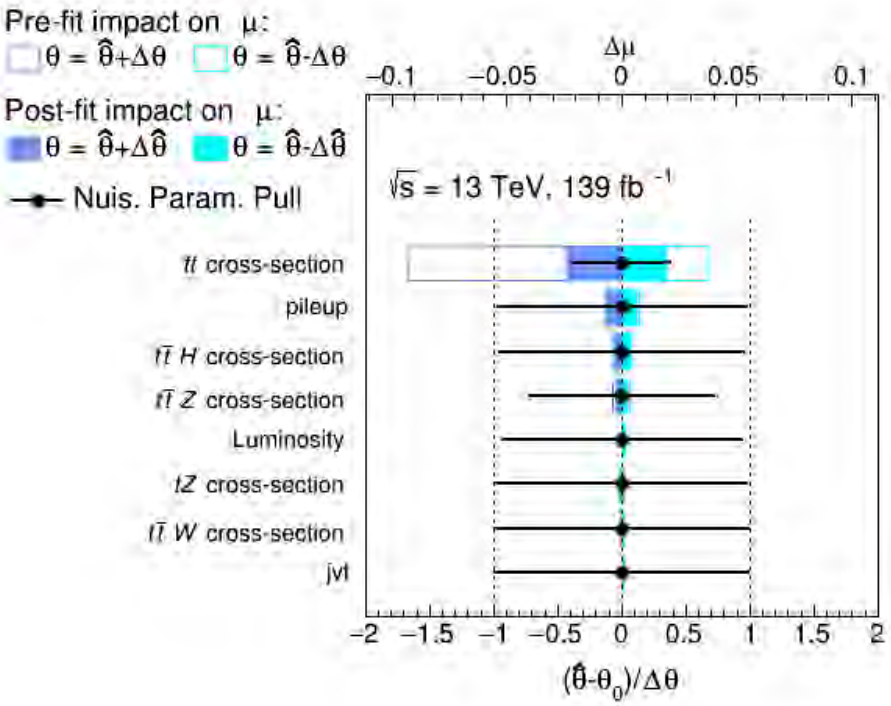

Figure 5.30: A figure ranking the impact of several of the NP considered in the fit. The bottom axis shows the plot of the NP pull ($\frac{(\hat{\theta}-\theta_0)}{\Delta\theta}$ where the $\hat{\theta}$) while the top axis shows the impact ($\Delta\mu$). The empty (filled) blue rectangles show the pre-fit(post-fit) impact on the A_C^ℓ. The NP are ranked in by their impact in descending order.

The FAR fit improves on the two main disadvantages of the TM method. By splitting the regions based on Δ_η^ℓ and binning them in terms of the gBDT score the sensitivity to the $t\bar{t}W^\pm$ process was improved. This provided a large reduction on the extracted errors as compared to the TM fit. Secondly the $t\bar{t}W^\pm$ cross section is no longer the NP with the largest impact on the fit as there is no correlation between the $t\bar{t}$ and $t\bar{t}W^\pm$ cross sections in the FAR fit. This fits with the theoretical expectation outline in section 5.8.3.

5.8.6 Projecting to higher luminosity

The following section presents an estimation of the uncertainties of future measurements of the A_C^ℓ at higher luminosity. The main limiting factor of this measurement is the limited size of the data set used which is directly correlated to the luminosity. Within the next

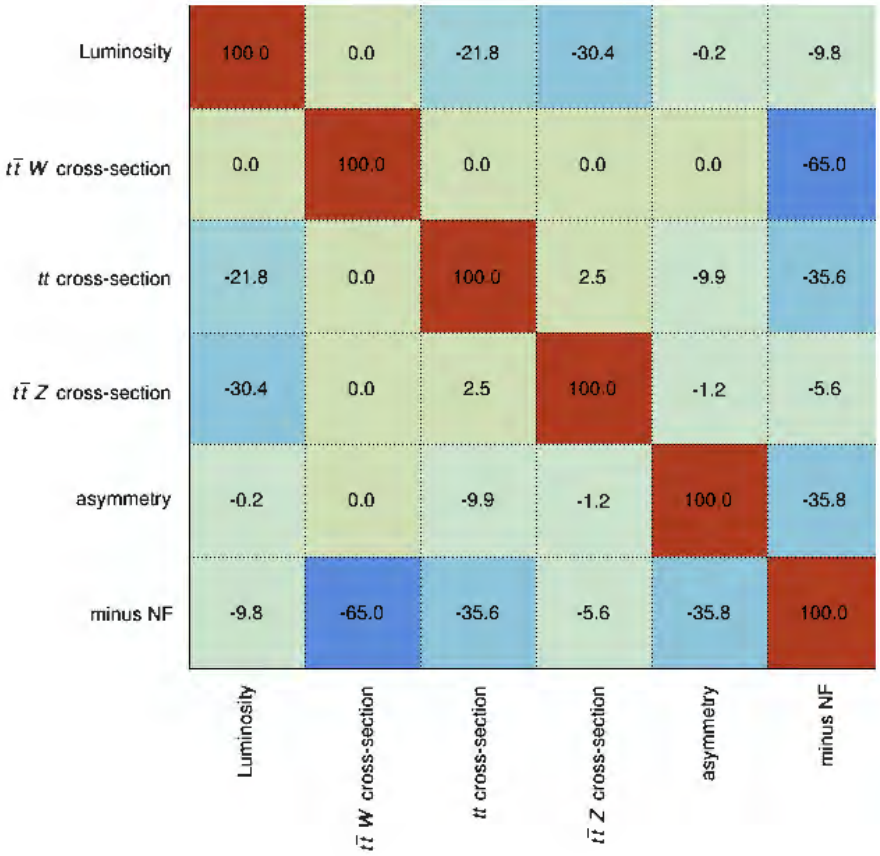

Figure 5.31: A correlation matrix is shown which provides the correlation between the normalisation NP's included in the FAR fit. A value of 0.0 corresponds to a linear correlation coefficient of less than 0.05.

decade at CERN aims to increase the luminosity substantially as the LHC should begin Run 3 within the next year and the High Luminosity (HL) LHC is set to begin running in the late 2020's/early 2030s. By combining Run 2 and Run 3 total luminosity of 300 fb^{-1} is expected. Including the HL-LHC, the total integrated luminosity is expected to increase to approximately 3000 fb^{-1}. As such it is useful to be able to estimate what uncertainties the current measurement setup would extract with much larger luminosities. When the simulation is normalised one of the factors is the total integrated luminosity. By changing the value of the luminosity used in the normalisation to match that of a higher luminosity, the simulation can predict the corresponding number of events that will occur. The fit is run using Asimov data as defined in section 5.8.2. The A_C^ℓ can then be measured at several different luminosity values and then plotted which would show how the uncertainties evolve as the luminosity increases.

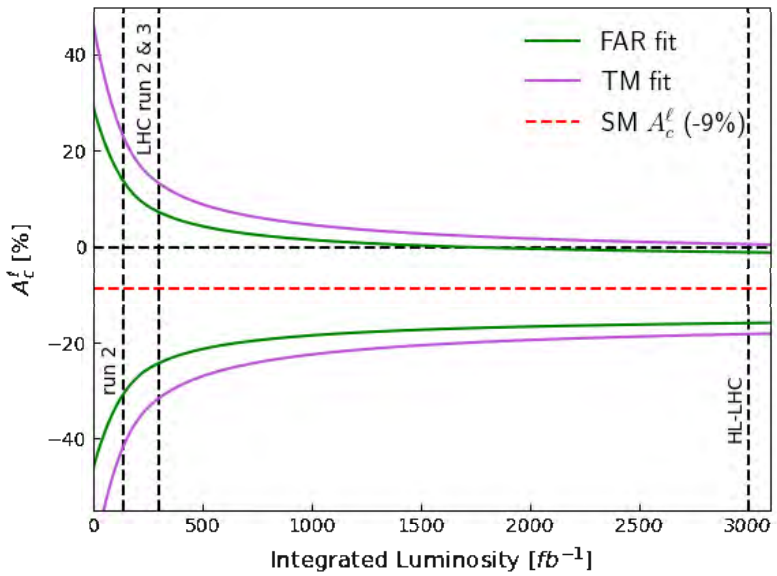

Figure 5.32: The expected uncertainties on the A_C^ℓ [%] measurement for the TM and FAR fits are shown with respect to the total integrated luminosity [fb^{-1}]. This plot also indicates the expected luminosity's for the run 2 + 3 and the HL-LHC.

Figure 5.32 shows the uncertainties measured on the A_C^ℓ versus the assumed integrated luminosity for both the TM (purple) and FAR (green) fits. The errors on the measured A_C^ℓ are shown in purple (green) for the TM (FAR) fit. Although the two methods measure slightly different A_C^ℓ it is beneficial to show how the uncertainties compare between the two methods. The SM predictions for the two methods correspond to -9% when round to the nearest whole number and this is shown with a red dotted line. The uncertainties on the SM prediction are not shown as these are negligible. Several milestones are indicated on the plot, each referring to a specific luminosity. These milestones are Run 2, the combination

of Runs 2 and 3, and the high-luminosity LHC which correspond to 139 fb^{-1}, 300fb^{-1} and 3000 fb^{-1} respectively. In figure 5.32 several points should be noted. The first is that there is a substantial reduction in errors between the TM and the FAR fit. Secondly, when the luminosity is increased from run 2 to also include run 3 the uncertainties decrease sharply which occurs for both of the fits. Once both fits reach a high enough luminosity they no longer agree, within 1σ, with a $A_C^\ell = 0\%$. This is not a statistically powerful statement as it would only start to be considered as a disagreement when it reaches a 3σ difference. For both methods, once the measurement no longer agrees with a $A_C^\ell = 0\%$ within 1σ, the gradient of the uncertainty curves flattens out. This indicates that the main source of uncertainties has shifted from statistical to being dominated by systematic uncertainty. Future studies could improve on these uncertainty estimates by further suppressing the background contribution through the use of a neural network.

Chapter 6

Conclusion

In this dissertation, the measurement of the A_C^ℓ in $t\bar{t}W^\pm$ in the trilepton final state in proton-proton collisions at $\sqrt{s} = 13$ TeV using the ATLAS experiment has been presented. The A_C^ℓ observable is calculated using the pseudorapidities of the leptons that decay from processes with top quark pair production such as in $t\bar{t}W^\pm$. The A_C^ℓ is sensitive to new physics beyond the standard model such as the axigluon as well as several operators in EFT and, as a result, a measurement of the A_C^ℓ could prove useful in searches for new physics. The data set used in this measurement corresponds to an integrated luminosity of 139 fb^{-1} which provides the opportunity to measure the A_C^ℓ in the rare $t\bar{t}W^\pm$ process. Before measurement of the A_C^ℓ could occur, the following steps needed to be taken - specifically the event selection, the lepton-top association and extraction of the A_C^ℓ.

The $t\bar{t}W^\pm$ process is a rare process with several dominant backgrounds in the trilepton channel such as $t\bar{t}$ and $t\bar{t}Z$. As such an event selection was used to create signal regions that are sensitive to the $t\bar{t}W^\pm$ process as well as control regions for constraining background processes. This event selection resulted in five signal and control regions which were two signal regions, two $t\bar{t}$ regions and one $t\bar{t}Z$ control region. The $t\bar{t}Z$ control region was used to constrain the modelling and normalisation of the $t\bar{t}Z$ process and a lesser degree the tZ process. The SR and $t\bar{t}$ regions provided sensitivity to the $t\bar{t}W^\pm$ process with the $t\bar{t}$ regions also being used to constrain the $t\bar{t}$ process. It should be noted that the signal and $t\bar{t}$ regions were dominated by background processes and as a result reductions of backgrounds within these regions, in particular, the SR low jet and $t\bar{t}$ low jet regions would improve the sensitivity of the measurement. A prominent background contribution is due to fake leptons, where the dominant source of fake leptons is the $t\bar{t}$ process. To ensure that the fake contribution to the background is modelled well the $t\bar{t}$ and Z + jets samples were used and the normalisation of the $t\bar{t}$ process was allowed to vary within the fit.

The two leptons which decay from top quarks need to be identified to reconstruct the A_C^ℓ and as a result, a lepton-top association was performed to identify the leptons that

decay from top quarks within a $t\bar{t}W^{\pm}$ event. The lepton-top association utilised information relating to the top quark systems such as the mass of the lepton-b-jet system and the ΔR between leptons and b-jets. Several methods were investigated for this purpose and the method with the best classification was an ML algorithm known as a GTB. The GTB algorithm was trained on a second $t\bar{t}W^{\pm}$ sample and was able to correctly identified leptons decaying from top quarks approximately 72 % of the time. Using the lepton-top association the Δ^{ℓ}_{η} variable could be calculated.

Several methods were investigated for the measurement of the A^{ℓ}_{C}, which are template morphing and the fit across regions (FAR), where the FAR fit provided increased sensitivity and reduced uncertainties as compared to the TM fit. The FAR fit split the five regions defined in the event selection into regions with positive and negative Δ^{ℓ}_{η} resulting in ten regions. An event-level gBDT was then trained to discriminate between $t\bar{t}W^{\pm}$ and all of the background processes. Each of the ten regions was plotted in terms of the gBDT score and the yields of $t\bar{t}W^{\pm}$ in the positive and negative regions were extracted from which the A^{ℓ}_{C} was calculated. The results as measured by the template morphing are $A^{\ell}_{C} = -9\%^{+30}_{-32}$ and the results as measured by the FAR fit are $A^{\ell}_{C} = -9\% \pm 22\%$. The uncertainties on the A^{ℓ}_{C} extracted using the FAR fit are greatly reduced when compared to the template morphing due to an increase in sensitivity. The improved sensitivity is due to two factors. The first is splitting the regions up based on the sign of Δ^{ℓ}_{η} and binning the regions more finely in terms of a separate variable. The second reason is variable which was used in these regions was the gBDT score which discriminates between $t\bar{t}W^{\pm}$ and the background processes. Although the FAR fit was able to reduce the uncertainties on the measured A^{ℓ}_{C} improvements in the discrimination between $t\bar{t}W^{\pm}$ and background process could further improve the sensitivity to the $t\bar{t}W^{\pm}$ process. Improvements to the event-level gBDT could come from better optimisation of the algorithm as well as providing new independent information to the algorithm. Finally, the dominant source of uncertainty in this measurement is due to the limited size of the data set. The data acquired at the LHC over the next decade should rectify this problem and help to further reduce the uncertainties on the measurement of the A^{ℓ}_{C} in $t\bar{t}W^{\pm}$.

Bibliography

[1] Matic Lubej. Standard model. URL https://www.physik.uzh.ch/groups/serra/StandardModel.html. (accessed: 14.07.2021).

[2] Esma Mobs. The CERN accelerator complex - August 2018. Complexe des accélérateurs du CERN - Août 2018. Aug 2018. URL https://cds.cern.ch/record/2636343. General Photo.

[3] Ramon Cid Manzano Xabier Cid Vidal. Lhc layout. URL https://www.lhc-closer.es/taking_a_closer_look_at_lhc/0.lhc_layout.

[4] ATLAS collaboration. Luminositypublicresultsrun2. URL https://twiki.cern.ch/twiki/bin/view/AtlasPublic/LuminosityPublicResultsRun2.

[5] Joao Pequenao. Computer generated image of the whole ATLAS detector. Mar 2008. URL https://cds.cern.ch/record/1095924.

[6] M. Aaboud, G. Aad, B. Abbott, J. Abdallah, O. Abdinov, B. Abeloos, R. Aben, O. S. AbouZeid, N. L. Abraham, and et al. Measurement of the $t\bar{t}Z$ and $t\bar{t}W^{\pm}$ production cross sections in multilepton final states using 3.2 fb^{-1} of pp collisions at $\sqrt{s} = 13$ tev with the atlas detector. *The European Physical Journal C*, 77(1), Jan 2017. ISSN 1434-6052. doi: 10.1140/epjc/s10052-016-4574-y. URL http://dx.doi.org/10.1140/epjc/s10052-016-4574-y.

[7] M. Aaboud, G. Aad, B. Abbott, D. C. Abbott, O. Abdinov, B. Abeloos, D. K. Abhayasinghe, S. H. Abidi, O. S. AbouZeid, N. L. Abraham, and et al. Measurement of the $t\bar{t}Z$ and $t\bar{t}W^{\pm}$ cross sections in proton-proton collisions at $\sqrt{s} = 13$ TeV with the atlas detector. *Physical Review D*, 99(7), Apr 2019. ISSN 2470-0029. doi: 10.1103/physrevd.99.072009. URL http://dx.doi.org/10.1103/PhysRevD.99.072009.

[8] Measurement of the top pair-production in association with a W or Z boson in pp collisions at 13 TeV. Technical report, CERN, Geneva, 2016. URL https://cds.cern.ch/record/2205283.

[9] A. M. Sirunyan, A. Tumasyan, W. Adam, F. Ambrogi, E. Asilar, T. Bergauer, J. Brandstetter, E. Brondolin, M. Dragicevic, and et al. Measurement of the cross section for top

quark pair production in association with a w or z boson in proton-proton collisions at $\sqrt{s} = 13$ tev. *Journal of High Energy Physics*, 2018(8), Aug 2018. ISSN 1029-8479. doi: 10.1007/jhep08(2018)011. URL http://dx.doi.org/10.1007/JHEP08(2018)011.

[10] J. H. Kühn and G. Rodrigo. Charge asymmetry in hadroproduction of heavy quarks. *Physical Review Letters*, 81(1):49–52, Jul 1998. ISSN 1079-7114. doi: 10.1103/physrevlett.81.49. URL http://dx.doi.org/10.1103/PhysRevLett.81.49.

[11] J. A. Aguilar-Saavedra, D. Amidei, A. Juste, and M. Pérez-Victoria. Asymmetries in top quark pair production at hadron colliders. *Reviews of Modern Physics*, 87(2): 421–455, May 2015. ISSN 1539-0756. doi: 10.1103/revmodphys.87.421. URL http://dx.doi.org/10.1103/RevModPhys.87.421.

[12] F. Maltoni, M.L. Mangano, I. Tsinikos, and M. Zaro. Top-quark charge asymmetry and polarization in $t\bar{t}W^{\pm}$ production at the lhc. *Physics Letters B*, 736:252–260, Sep 2014. ISSN 0370-2693. doi: 10.1016/j.physletb.2014.07.033. URL http://dx.doi.org/10.1016/j.physletb.2014.07.033.

[13] Mark Thomson. *Modern particle physics*. Cambridge University Press, New York, 2013. ISBN 978-1-107-03426-6.

[14] Vera C. Rubin. One hundred years of rotating galaxies1. *Publications of the Astronomical Society of the Pacific*, 112(772):747–750, jun 2000. doi: 10.1086/316573. URL https://doi.org/10.1086/316573.

[15] Andrew Liddle. *An introduction to modern cosmology; 2nd ed.* Wiley, Chichester, 2003. URL https://cds.cern.ch/record/1010476.

[16] B. Grzadkowski, M. Iskrzyński, M. Misiak, and J. Rosiek. Dimension-six terms in the standard model lagrangian. *Journal of High Energy Physics*, 2010(10), Oct 2010. ISSN 1029-8479. doi: 10.1007/jhep10(2010)085. URL http://dx.doi.org/10.1007/JHEP10(2010)085.

[17] CERN collaborators. What is an accelerator? URL https://home.cern/science/accelerators.

[18] Brüning, Oliver Sim and Collier, Paul and Lebrun, P and Myers, Stephen and Ostojic, Ranko and Poole, John and Proudlock, Paul. *LHC Design Report*. CERN Yellow Reports: Monographs. CERN, Geneva, 2004. doi: 10.5170/CERN-2004-003-V-1. URL http://cds.cern.ch/record/782076.

[19] Paul H. Frampton and Sheldon L. Glashow. Chiral color: An alternative to the standard model. *Physics Letters B*, 190(1):157–161, 1987. ISSN 0370-2693. doi: https://doi.org/10.1016/0370-2693(87)90859-8. URL https://www.sciencedirect.com/science/article/pii/0370269387908598.

[20] Sheldon L. Glashow. Partial-symmetries of weak interactions. *Nuclear Physics*, 22(4): 579–588, 1961. ISSN 0029-5582. doi: https://doi.org/10.1016/0029-5582(61)90469-2. URL https://www.sciencedirect.com/science/article/pii/0029558261904692.

[21] Steven Weinberg. A model of leptons. *Phys. Rev. Lett.*, 19:1264–1266, Nov 1967. doi: 10.1103/PhysRevLett.19.1264. URL https://link.aps.org/doi/10.1103/PhysRevLett.19.1264.

[22] F. Englert and R. Brout. Broken Symmetry and the Mass of Gauge Vector Mesons. *Phys. Rev. Lett.*, 13:321–323, 1964. doi: 10.1103/PhysRevLett.13.321.

[23] Peter W. Higgs. Broken symmetries and the masses of gauge bosons. *Phys. Rev. Lett.*, 13:508–509, Oct 1964. doi: 10.1103/PhysRevLett.13.508. URL https://link.aps.org/doi/10.1103/PhysRevLett.13.508.

[24] G. Aad, T. Abajyan, B. Abbott, J. Abdallah, S. Abdel Khalek, A.A. Abdelalim, O. Abdinov, R. Aben, B. Abi, M. Abolins, and et al. Observation of a new particle in the search for the standard model higgs boson with the atlas detector at the lhc. *Physics Letters B*, 716(1):1–29, Sep 2012. ISSN 0370-2693. doi: 10.1016/j.physletb.2012.08.020. URL http://dx.doi.org/10.1016/j.physletb.2012.08.020.

[25] S. Chatrchyan, V. Khachatryan, A.M. Sirunyan, A. Tumasyan, W. Adam, E. Aguilo, T. Bergauer, M. Dragicevic, J. Erö, C. Fabjan, and et al. Observation of a new boson at a mass of 125 gev with the cms experiment at the lhc. *Physics Letters B*, 716(1): 30–61, Sep 2012. ISSN 0370-2693. doi: 10.1016/j.physletb.2012.08.021. URL http://dx.doi.org/10.1016/j.physletb.2012.08.021.

[26] P.A. Zyla et al. Review of Particle Physics. *PTEP*, 2020(8):083C01, 2020. doi: 10.1093/ptep/ptaa104.

[27] Y. Fukuda, T. Hayakawa, E. Ichihara, K. Inoue, K. Ishihara, H. Ishino, Y. Itow, T. Kajita, J. Kameda, S. Kasuga, and et al. Evidence for oscillation of atmospheric neutrinos. *Physical Review Letters*, 81(8):1562–1567, Aug 1998. ISSN 1079-7114. doi: 10.1103/physrevlett.81.1562. URL http://dx.doi.org/10.1103/PhysRevLett.81.1562.

[28] Q. R. Ahmad, R. C. Allen, T. C. Andersen, J. D. Anglin, G. Bühler, J. C. Barton, E. W. Beier, M. Bercovitch, J. Bigu, S. Biller, and et al. Measurement of the rate ofe+dp+p+einteractions produced byb8solar neutrinos at the sudbury neutrino observatory. *Physical Review Letters*, 87(7), Jul 2001. ISSN 1079-7114. doi: 10.1103/physrevlett.87.071301. URL http://dx.doi.org/10.1103/PhysRevLett.87.071301.

[29] S. Bilenky. Neutrinos: Majorana or dirac?, 2020.

[30] Laurent Canetti, Marco Drewes, and Mikhail Shaposhnikov. Matter and antimatter in the universe. *New Journal of Physics*, 14(9):095012, Sep 2012. ISSN 1367-2630. doi: 10.1088/1367-2630/14/9/095012. URL http://dx.doi.org/10.1088/1367-2630/14/9/095012.

[31] Nicolas Deutschmann. Higgs production at NLO in the standard model effective field theory. *Journal of Physics: Conference Series*, 878:012020, jul 2017. doi: 10.1088/1742-6596/878/1/012020. URL https://doi.org/10.1088/1742-6596/878/1/012020.

[32] R. Aaij, C. Abellán Beteta, T. Ackernley, B. Adeva, M. Adinolfi, H. Afsharnia, C. A. Aidala, S. Aiola, Z. Ajaltouni, and S. Akar et al. Test of lepton universality in beauty-quark decays, 2021.

[33] T. Albahri, A. Anastasi, A. Anisenkov, K. Badgley, S. Baeßler, I. Bailey, V. A. Baranov, E. Barlas-Yucel, T. Barrett, A. Basti, and et al. Measurement of the anomalous precession frequency of the muon in the fermilab muon g2 experiment. *Physical Review D*, 103(7), Apr 2021. ISSN 2470-0029. doi: 10.1103/physrevd.103.072002. URL http://dx.doi.org/10.1103/PhysRevD.103.072002.

[34] J. Alwall, R. Frederix, S. Frixione, V. Hirschi, F. Maltoni, O. Mattelaer, H.-S. Shao, T. Stelzer, P. Torrielli, and M. Zaro. The automated computation of tree-level and next-to-leading order differential cross sections, and their matching to parton shower simulations. *Journal of High Energy Physics*, 2014(7), Jul 2014. ISSN 1029-8479. doi: 10.1007/jhep07(2014)079. URL http://dx.doi.org/10.1007/JHEP07(2014)079.

[35] Torbjörn Sjöstrand, Stefan Ask, Jesper R. Christiansen, Richard Corke, Nishita Desai, Philip Ilten, Stephen Mrenna, Stefan Prestel, Christine O. Rasmussen, and Peter Z. Skands. An introduction to pythia 8.2. *Computer Physics Communications*, 191:159–177, Jun 2015. ISSN 0010-4655. doi: 10.1016/j.cpc.2015.01.024. URL http://dx.doi.org/10.1016/j.cpc.2015.01.024.

[36] T Gleisberg, S Höche, F Krauss, M Schönherr, S Schumann, F Siegert, and J Winter. Event generation with sherpa 1.1. *Journal of High Energy Physics*, 2009(02):007–007, Feb 2009. ISSN 1029-8479. doi: 10.1088/1126-6708/2009/02/007. URL http://dx.doi.org/10.1088/1126-6708/2009/02/007.

[37] C. Oleari. The powheg box. *Nuclear Physics B - Proceedings Supplements*, 205-206: 36–41, Aug 2010. ISSN 0920-5632. doi: 10.1016/j.nuclphysbps.2010.08.016. URL http://dx.doi.org/10.1016/j.nuclphysbps.2010.08.016.

[38] Davison E. Soper. Basics of QCD perturbation theory. In *24th Annual SLAC Summer Institute on Particle Physics: The Strong Interaction, From Hadrons to Protons*, pages 15–42, 8 1996.

[39] Stefan Höche. Introduction to parton-shower event generators, 2015.

[40] K Aamodt, A Abrahantes Quintana, R Achenbach, S Acounis, D Adamova, C Adler, M Aggarwal, F Agnese, G Aglieri Rinella, and Z et al Ahammed. The ALICE experiment at the CERN LHC. A Large Ion Collider Experiment. *JINST*, 3:S08002. 259 p, 2008. doi: 10.1088/1748-0221/3/08/S08002. URL http://cds.cern.ch/record/1129812. Also published by CERN Geneva in 2010.

[41] The ATLAS Collaboration, G Aad, E Abat, J Abdallah, A A Abdelalim, A Abdesselam, O Abdinov, B A Abi, M Abolins, H Abramowicz, and E Acerbi et al. 3(08):S08003–S08003, aug 2008. doi: 10.1088/1748-0221/3/08/s08003. URL https://doi.org/10.1088/1748-0221/3/08/s08003.

[42] The CMS Collaboration, S Chatrchyan, G Hmayakyan, V Khachatryan, A M Sirunyan, W Adam, T Bauer, T Bergauer, and H Bergauer et al. 3(08):S08004–S08004, aug 2008. doi: 10.1088/1748-0221/3/08/s08004. URL https://doi.org/10.1088/1748-0221/3/08/s08004.

[43] The LHCb Collaboration, A Augusto Alves, L M Andrade Filho, A F Barbosa, I Bediaga, G Cernicchiaro, G Guerrer, H P Lima, and A A Machado et al. 3 (08):S08005–S08005, aug 2008. doi: 10.1088/1748-0221/3/08/s08005. URL https://doi.org/10.1088/1748-0221/3/08/s08005.

[44] Michael Benedikt, Paul Collier, V Mertens, John Poole, and Karlheinz Schindl. *LHC Design Report*. CERN Yellow Reports: Monographs. CERN, Geneva, 2004. doi: 10.5170/CERN-2004-003-V-3. URL http://cds.cern.ch/record/823808.

[45] *ATLAS inner detector: Technical Design Report, 1*. Technical design report. ATLAS. CERN, Geneva, 1997. URL https://cds.cern.ch/record/331063.

[46] *ATLAS magnet system: Technical Design Report, 1*. Technical design report. ATLAS. CERN, Geneva, 1997. URL https://cds.cern.ch/record/338080.

[47] G. Aielli, A. Aloisio, M. Alviggi, V. Aprodu, V. Bocci, E. Brambilla, D. Bartos, S. Buda, P. Camarri, and G. Chiodi et al. The rpc first level muon trigger in the barrel of the atlas experiment. *Nuclear Physics B - Proceedings Supplements*, 158:11–15, 2006. ISSN 0920-5632. doi: https://doi.org/10.1016/j.nuclphysbps.2006.07.031. URL https://www.sciencedirect.com/science/article/pii/S0920563206004178. Proceedings of the 8th International Workshop on Resistive Plate Chambers and Related Detectors.

[48] S. Majewski, G. Charpak, A. Breskin, and G. Mikenberg. A thin multiwire chamber operating in the high multiplication mode. *Nuclear Instruments and Methods in Physics Research*, 217(1):265–271, 1983. ISSN 0167-5087. doi: https://doi.org/10.1016/

0167-5087(83)90146-1. URL https://www.sciencedirect.com/science/article/pii/0167508783901461.

[49] F. Bauer, U. Bratzler, H. Dietl, H. Kroha, Th. Lagouri, A. Manz, A. Ostapchuk, R. Richter, S. Schael, and S. Chouridou et al. Construction and test of mdt chambers for the atlas muon spectrometer. *Nuclear Instruments and Methods in Physics Research Section A: Accelerators, Spectrometers, Detectors and Associated Equipment*, 461(1):17–20, 2001. ISSN 0168-9002. doi: https://doi.org/10.1016/S0168-9002(00)01156-6. URL https://www.sciencedirect.com/science/article/pii/S0168900200011566. 8th Pisa Meeting on Advanced Detectors.

[50] Theodoros Argyropoulos, Ketevi Adikle Assamagan, Brian Hugues Benedict, Valeri Chernyatin, Elliot Cheu, and Deng et al. Cathode strip chambers in atlas: Installation, commissioning and *in Situ* performance. *IEEE Transactions on Nuclear Science*, 56 (3):1568–1574, 2009. doi: 10.1109/TNS.2009.2020861.

[51] *ATLAS level-1 trigger: Technical Design Report*. Technical design report. ATLAS. CERN, Geneva, 1998. URL http://cds.cern.ch/record/381429.

[52] Peter Jenni, Marzio Nessi, Markus Nordberg, and Kenway Smith. *ATLAS high-level trigger, data-acquisition and controls: Technical Design Report*. Technical design report. ATLAS. CERN, Geneva, 2003. URL http://cds.cern.ch/record/616089.

[53] G. Aad, B. Abbott, J. Abdallah, O. Abdinov, R. Aben, M. Abolins, O. S. AbouZeid, H. Abramowicz, H. Abreu, and et al. Measurement of the $t\bar{t}W^{\pm}$ and $t\bar{t}Z$ production cross sections in pp collisions at $\sqrt{s} = 8$ tev with the atlas detector. *Journal of High Energy Physics*, 2015(11), Nov 2015. ISSN 1029-8479. doi: 10.1007/jhep11(2015)172. URL http://dx.doi.org/10.1007/JHEP11(2015)172.

[54] Andy Buckley, Christoph Englert, James Ferrando, David J. Miller, Liam Moore, Michael Russell, and Chris D. White. Constraining top quark effective theory in the lhc run ii era. *Journal of High Energy Physics*, 2016(4):1–32, Apr 2016. ISSN 1029-8479. doi: 10.1007/jhep04(2016)015. URL http://dx.doi.org/10.1007/JHEP04(2016)015.

[55] Jeff Asaf Dror, Marco Farina, Ennio Salvioni, and Javi Serra. Strong tw scattering at the lhc. *Journal of High Energy Physics*, 2016(1), Jan 2016. ISSN 1029-8479. doi: 10.1007/jhep01(2016)071. URL http://dx.doi.org/10.1007/JHEP01(2016)071.

[56] V. Khachatryan, A. M. Sirunyan, A. Tumasyan, W. Adam, E. Asilar, T. Bergauer, J. Brandstetter, E. Brondolin, M. Dragicevic, and et al. Observation of top quark pairs produced in association with a vector boson in pp collisions at $\sqrt{s} = 8$ tev. *Journal of High Energy Physics*, 2016(1), Jan 2016. ISSN 1029-8479. doi: 10.1007/jhep01(2016)096. URL http://dx.doi.org/10.1007/JHEP01(2016)096.

[57] Rikkert Frederix and Ioannis Tsinikos. Subleading EW corrections and spin-correlation effects in $t\bar{t}W$ multi-lepton signatures. *Eur. Phys. J. C*, 80(9):803, 2020. doi: 10.1140/epjc/s10052-020-8388-6.

[58] V. M. Abazov, B. Abbott, B. S. Acharya, M. Adams, T. Adams, G. D. Alexeev, G. Alkhazov, A. Alton, G. Alverson, G. A. Alves, and et al. Forward-backward asymmetry in top quark-antiquark production. *Physical Review D*, 84(11), Dec 2011. ISSN 1550-2368. doi: 10.1103/physrevd.84.112005. URL http://dx.doi.org/10.1103/PhysRevD.84.112005.

[59] T. Aaltonen, S. Amerio, D. Amidei, A. Anastassov, A. Annovi, J. Antos, G. Apollinari, J. A. Appel, T. Arisawa, A. Artikov, and et al. Measurement of the top quark forward-backward production asymmetry and its dependence on event kinematic properties. *Physical Review D*, 87(9), May 2013. ISSN 1550-2368. doi: 10.1103/physrevd.87.092002. URL http://dx.doi.org/10.1103/PhysRevD.87.092002.

[60] V. M. Abazov, B. Abbott, B. S. Acharya, M. Adams, T. Adams, J. P. Agnew, G. D. Alexeev, G. Alkhazov, A. Alton, A. Askew, and et al. Measurement of the forward-backward asymmetry in top quark-antiquark production inppcollisions using thelepton+jetschannel. *Physical Review D*, 90(7), Oct 2014. ISSN 1550-2368. doi: 10.1103/physrevd.90.072011. URL http://dx.doi.org/10.1103/PhysRevD.90.072011.

[61] Sunghoon Jung, Aaron Pierce, and James D. Wells. Top quark asymmetry from a non-abelian horizontal symmetry. *Physical Review D*, 83(11), Jun 2011. ISSN 1550-2368. doi: 10.1103/physrevd.83.114039. URL http://dx.doi.org/10.1103/PhysRevD.83.114039.

[62] Ross Diener, Stephen Godfrey, and Travis A. W. Martin. Using final state pseudorapidities to improves-channel resonance observables at the lhc. *Physical Review D*, 80(7), Oct 2009. ISSN 1550-2368. doi: 10.1103/physrevd.80.075014. URL http://dx.doi.org/10.1103/PhysRevD.80.075014.

[63] G. Aad, T. Abajyan, B. Abbott, J. Abdallah, S. Abdel Khalek, O. Abdinov, R. Aben, B. Abi, M. Abolins, and et al. Measurement of the top quark pair production charge asymmetry in proton-proton collisions at $\sqrt{s} = 7$ tev using the atlas detector. *Journal of High Energy Physics*, 2014(2), Feb 2014. ISSN 1029-8479. doi: 10.1007/jhep02(2014)107. URL http://dx.doi.org/10.1007/JHEP02(2014)107.

[64] S. Chatrchyan, V. Khachatryan, A. M. Sirunyan, A. Tumasyan, W. Adam, T. Bergauer, M. Dragicevic, J. Erö, C. Fabjan, and et al. Measurements of the $t\bar{t}$ charge asymmetry using the dilepton decay channel in pp collisions at $\sqrt{s} = 7$ tev. *Journal of High Energy Physics*, 2014(4), Apr 2014. ISSN 1029-8479. doi: 10.1007/jhep04(2014)191. URL http://dx.doi.org/10.1007/JHEP04(2014)191.

[65] V. Khachatryan, A. M. Sirunyan, A. Tumasyan, W. Adam, E. Asilar, T. Bergauer, J. Brandstetter, E. Brondolin, M. Dragicevic, J. Erö, and et al. Measurement of the charge asymmetry in top quark pair production in pp collisions at s=8 tevusing a template method. *Physical Review D*, 93(3), Feb 2016. ISSN 2470-0029. doi: 10.1103/physrevd.93.034014. URL http://dx.doi.org/10.1103/PhysRevD.93.034014.

[66] Inclusive and differential measurement of the charge asymmetry in $t\bar{t}$ events at 13 TeV with the ATLAS detector. Technical report, CERN, Geneva, Jul 2019. URL https://cds.cern.ch/record/2682109. All figures including auxiliary figures are available at https://atlas.web.cern.ch/Atlas/GROUPS/PHYSICS/CONFNOTES/ATLAS-CONF-2019-026.

[67] Georgios Choudalakis. Fully Bayesian Unfolding. *arXiv e-prints*, art. arXiv:1201.4612, January 2012.

[68] Luminosity determination in pp collisions at $\sqrt{s} = 13$ TeV using the ATLAS detector at the LHC. Technical Report ATLAS-CONF-2019-021, CERN, Geneva, Jun 2019. URL https://cds.cern.ch/record/2677054.

[69] G. Avoni, M. Bruschi, G. Cabras, D. Caforio, N. Dehghanian, A. Floderus, B. Giacobbe, F. Giannuzzi, F. Giorgi, and P. Grafström et al. The new LUCID-2 detector for luminosity measurement and monitoring in ATLAS. *Journal of Instrumentation*, 13(07):P07017–P07017, jul 2018. doi: 10.1088/1748-0221/13/07/p07017. URL https://doi.org/10.1088/1748-0221/13/07/p07017.

[70] Zoltán Nagy and Davison E. Soper. What is a parton shower? *Physical Review D*, 98(1), Jul 2018. ISSN 2470-0029. doi: 10.1103/physrevd.98.014034. URL http://dx.doi.org/10.1103/PhysRevD.98.014034.

[71] Richard D. Ball, Valerio Bertone, Stefano Carrazza, Christopher S. Deans, Luigi Del Debbio, Stefano Forte, Alberto Guffanti, Nathan P. Hartland, José I. Latorre, and et al. Parton distributions for the lhc run ii. *Journal of High Energy Physics*, 2015(4), Apr 2015. ISSN 1029-8479. doi: 10.1007/jhep04(2015)040. URL http://dx.doi.org/10.1007/JHEP04(2015)040.

[72] Stefano Frixione, Eric Laenen, Patrick Motylinski, Bryan R. Webber, and Chris D. White. Single-top hadroproduction in association with a W boson. *JHEP*, 07:029, 2008. doi: 10.1088/1126-6708/2008/07/029.

[73] Richard D. Ball et al. Parton distributions with LHC data. *Nucl. Phys. B*, 867:244, 2013. doi: 10.1016/j.nuclphysb.2012.10.003.

[74] M. Aaboud, G. Aad, B. Abbott, D. C. Abbott, O. Abdinov, B. Abeloos, D. K. Abhayasinghe, S. H. Abidi, O. S. AbouZeid, and et al. Electron reconstruction and identification in the atlas experiment using the 2015 and 2016 lhc proton–proton collision data at $\sqrt{s} = 13$ TeV. *The European Physical Journal C*, 79(8), Aug 2019. ISSN 1434-6052. doi: 10.1140/epjc/s10052-019-7140-6. URL http://dx.doi.org/10.1140/epjc/s10052-019-7140-6.

[75] G. Aad, B. Abbott, D.C. Abbott, A. Abed Abud, K. Abeling, D.K. Abhayasinghe, S.H. Abidi, O.S. AbouZeid, N.L. Abraham, H. Abramowicz, and et al. Electron and photon performance measurements with the atlas detector using the 2015–2017 lhc proton-proton collision data. *Journal of Instrumentation*, 14(12):P12006–P12006, Dec 2019. ISSN 1748-0221. doi: 10.1088/1748-0221/14/12/p12006. URL http://dx.doi.org/10.1088/1748-0221/14/12/P12006.

[76] M. Aaboud, G. Aad, B. Abbott, J. Abdallah, O. Abdinov, B. Abeloos, S. H. Abidi, O. S. AbouZeid, N. L. Abraham, and et al. Jet reconstruction and performance using particle flow with the atlas detector. *The European Physical Journal C*, 77(7), Jul 2017. ISSN 1434-6052. doi: 10.1140/epjc/s10052-017-5031-2. URL http://dx.doi.org/10.1140/epjc/s10052-017-5031-2.

[77] Matteo Cacciari, Gavin P Salam, and Gregory Soyez. The anti-ktjet clustering algorithm. *Journal of High Energy Physics*, 2008(04):063–063, Apr 2008. ISSN 1029-8479. doi: 10.1088/1126-6708/2008/04/063. URL http://dx.doi.org/10.1088/1126-6708/2008/04/063.

[78] Tagging and suppression of pileup jets with the ATLAS detector. Technical report, CERN, Geneva, May 2014. URL https://cds.cern.ch/record/1700870.

[79] G. Aad, B. Abbott, J. Abdallah, O. Abdinov, R. Aben, M. Abolins, O. S. AbouZeid, H. Abramowicz, H. Abreu, and et al. Performance of pile-up mitigation techniques for jets in pp collisions at $\sqrt{s} = 8 = 8$ TeV using the atlas detector. *The European Physical Journal C*, 76(11), Oct 2016. ISSN 1434-6052. doi: 10.1140/epjc/s10052-016-4395-z. URL http://dx.doi.org/10.1140/epjc/s10052-016-4395-z.

[80] Identification of Jets Containing b-Hadrons with Recurrent Neural Networks at the ATLAS Experiment. Technical Report ATL-PHYS-PUB-2017-003, CERN, Geneva, Mar 2017. URL https://cds.cern.ch/record/2255226.

[81] Reconstruction and Calibration of Missing Transverse Energy and Performance in Z and W events in ATLAS Proton-Proton Collisions at 7 TeV. Technical report, CERN, Geneva, Jun 2011. URL http://cds.cern.ch/record/1355703. All figures including auxiliary figures are available at

https://atlas.web.cern.ch/Atlas/GROUPS/PHYSICS/CONFNOTES/ATLAS-CONF-2011-080.

[82] C Santamarina and C Schuetz. Determination of the experimental k-factor. Technical report, 2003. URL http://cds.cern.ch/record/1369696.

[83] Jan Therhaag. TMVA Toolkit for multivariate data analysis in ROOT. *PoS*, ICHEP2010:510, 2010. doi: 10.22323/1.120.0510.

[84] Christopher M. Bishop. *Pattern Recognition and Machine Learning (Information Science and Statistics)*. Springer, 1 edition, 2007. ISBN 0387310738. URL http://www.amazon.com/Pattern-Recognition-Learning-Information-Statistics/dp/0387310738%3FSubscriptionId%3D13CT5CVB80YFWJEPWS02%26tag%3Dws%26linkCode%3Dxm2%26camp%3D2025%26creative%3D165953%26creativeASIN%3D0387310738.

[85] François Chollet et al. Keras. https://keras.io, 2015.

[86] P Speckmayer, A Höcker, J Stelzer, and H Voss. The toolkit for multivariate data analysis, TMVA 4. *Journal of Physics: Conference Series*, 219(3):032057, apr 2010. doi: 10.1088/1742-6596/219/3/032057. URL https://doi.org/10.1088/1742-6596/219/3/032057.

[87] Michele Pinamonti. Statistical methods at atlas and cms. accessed: 05.10.2021, 2018. URL https://indico.cern.ch/event/727396/contributions/3021899/.

[88] Glen Cowan, Kyle Cranmer, Eilam Gross, and Ofer Vitells. Asymptotic formulae for likelihood-based tests of new physics. *The European Physical Journal C*, 71(2), Feb 2011. ISSN 1434-6052. doi: 10.1140/epjc/s10052-011-1554-0. URL http://dx.doi.org/10.1140/epjc/s10052-011-1554-0.

[89] G. Aad, B. Abbott, D. C. Abbott, A. Abed Abud, K. Abeling, D. K. Abhayasinghe, S. H. Abidi, O. S. AbouZeid, N. L. Abraham, and et al. Observation of the associated production of a top quark and a z boson in pp collisions at $\sqrt{s}$= 13 tev with the atlas detector. *Journal of High Energy Physics*, 2020(7), Jul 2020. ISSN 1029-8479. doi: 10.1007/jhep07(2020)124. URL http://dx.doi.org/10.1007/JHEP07(2020)124.

[90] A. M. Sirunyan, A. Tumasyan, W. Adam, F. Ambrogi, E. Asilar, T. Bergauer, J. Brandstetter, M. Dragicevic, J. Erö, A. Escalante Del Valle, and et al. Observation of $t\bar{t}H$ production. *Physical Review Letters*, 120(23), Jun 2018. ISSN 1079-7114. doi: 10.1103/physrevlett.120.231801. URL http://dx.doi.org/10.1103/PhysRevLett.120.231801.

[91] Michele Pinamonti and Loic Valery. Trexfitter documentation. URL https://trexfitter-docs.web.cern.ch/trexfitter-docs/.

[92] M. et al Aaboud. Search for the standard model higgs boson produced in association with top quarks and decaying into a $b\bar{b}$ pair in pp collisions at $\sqrt{s}$ =13 TeV with the atlas detector. *Phys. Rev. D*, 97:072016, Apr 2018. doi: 10.1103/PhysRevD.97.072016. URL https://link.aps.org/doi/10.1103/PhysRevD.97.072016.